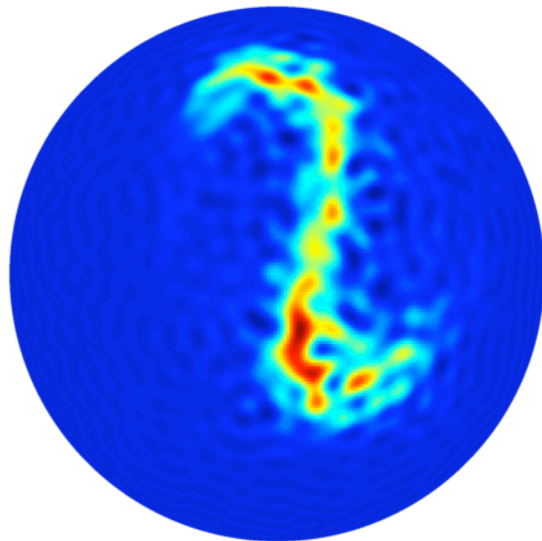


Classical Bifurcation  
and Entanglement Generation  
in an Internal Bosonic Josephson Junction



Tilman Zibold  
2012



Dissertation  
submitted to the  
Combined Faculties of the Natural Sciences and  
Mathematics  
of the Ruperto-Carola-University of Heidelberg, Germany  
for the degree of  
Doctor of Natural Sciences

Put forward by  
Dipl. Phys. Tilman Zibold  
born in: Ravensburg  
Oral examination: 4.7.2012



**Classical Bifurcation  
and Entanglement Generation  
in an Internal Bosonic Josephson Junction**

Referees: Prof. Dr. Markus K. Oberthaler  
Prof. Dr. Thomas Gasenzer



## Abstract

In this work the dynamical behavior of an internal bosonic Josephson junction is investigated. The junction is realized using two Zeeman sub states of the ground state hyperfine manifold in a Bose-Einstein condensate of  $^{87}\text{Rb}$ . With several hundreds of atoms, the size of the system is at the crossover where its classical description breaks down and quantum mechanical effects become important. The system allows for a high level of control in terms of state preparation, readout and its important parameters. Thus its classical dynamics, which show a striking bifurcating behavior, can be studied by mapping out the full phase space and revealing its topological change. Furthermore the dynamics at the unstable classical fixed point arising in the course of the bifurcation are investigated. The dynamics at this point clearly show the breakdown of the classical description. The dynamical evolution leads to spin squeezing and entanglement and subsequently to macroscopic superposition states. The generation of squeezing is quantitatively analyzed and the generated states are reconstructed in terms of their Wigner functions by tomography. This work is an important step for the understanding of highly entangled macroscopic quantum states.

## Zusammenfassung

In dieser Arbeit wird die Dynamik eines internen bosonischen Josephson Kontakts untersucht. Der Kontakt wird durch zwei Zeeman-Unterszustände der Hyperfein Grundzustände in einem Bose-Einstein Kondensat aus  $^{87}\text{Rb}$  realisiert. Mit mehreren hundert Atomen ist die Größe des Systems am Übergang, an dem seine klassische Beschreibung versagt und quantenmechanische Effekte bedeutsam werden. Das System erlaubt ein hohes Maß an Kontrolle in Bezug auf Zustandspräparation, Zustandsmessung und seiner wichtigen Parameter und ermöglicht so die Untersuchung der klassischen Dynamik. Durch das Vermessen des gesamten Phasenraumes und das Aufzeigen der damit verbundenen topologischen Veränderungen zeigt sich ein bemerkenswertes bifurkierendes Verhalten. Der durch die Bifurkation entstehende instabile klassische Fixpunkt wird auf seine Quantendynamik hin untersucht. Sie zeigt deutlich das Versagen der klassischen Beschreibung. In diesem System erzeugt der dynamische Verlauf spin squeezing und Verschränkung und führt im folgenden zu makroskopischen Superpositionszuständen. Der Entstehungsprozess des spin squeezing wird quantitativ analysiert und die erzeugten Zustände werden in Form ihrer Wigner Funktionen tomographisch rekonstruiert. Diese Arbeit stellt einen wichtigen Schritt für das Verständnis von hochgradig verschränkten makroskopischen Quantenzuständen dar.



# Contents

|          |  |           |
|----------|--|-----------|
| <b>1</b> | <b>Introduction</b>  | <b>1</b>  |
| <b>2</b> | <b>A Pair of Linearly Coupled Bose-Einstein Condensates</b>                    | <b>3</b>  |
| 2.1      | Two Linearly Coupled Interacting BECs . . . . .                                | 3         |
| 2.2      | Angular Momentum Operators . . . . .   | 4         |
| 2.3      | Hilbert Space and Number State Basis . . . . .                                 | 5         |
| 2.4      | Coherent Spin States . . . . .   | 6         |
| 2.5      | Bloch Sphere and Husimi Representation . . . . .                               | 7         |
| 2.6      | Pictorial Interpretation of the Hamiltonian . . . . .                          | 9         |
| <b>3</b> | <b>Experimental Realization of the Internal Bosonic Josephson Junction</b>     | <b>13</b> |
| 3.1      | The Atomic Two-state System . . . . .  | 13        |
| 3.2      | Creating a Bose-Einstein Condensate . . . . .                                  | 14        |
| 3.3      | Creating many Copies of the same State . . . . .                               | 15        |
| 3.4      | Coupling of the Two Spin States . . . . .                                      | 17        |
| 3.5      | Nonlinearity and Feshbach Resonance . . . . .                                  | 18        |
| 3.6      | Time Dependence of the Spatial Wave Functions . . . . .                        | 19        |
| 3.7      | Imaging . . . . .  | 20        |
| 3.7.1    | Imaging Noise . . . . .  | 22        |
| 3.8      | Experimental Imperfections . . . . .   | 22        |
| 3.8.1    | Atom Loss . . . . .  | 22        |
| 3.8.2    | Magnetic Field Noise . . . . .   | 23        |
| 3.8.3    | Magnetic Field Stabilisation . . . . .   | 23        |
| 3.8.4    | Magnetic Field Gradients . . . . .   | 24        |
| 3.8.5    | Rabi Frequency Gradients . . . . .   | 25        |
| <b>4</b> | <b>Classical Bifurcation at the Transition from Rabi to Josephson Dynamics</b> | <b>27</b> |
| 4.1      | The Classical Mean Field Hamiltonian . . . . .                                 | 27        |
| 4.2      | Topologies of the Mean Field Hamiltonian . . . . .                             | 28        |
| 4.3      | A Classical Analog . . . . .   | 30        |
| 4.4      | Influence of the Detuning on the Classical Dynamics . . . . .                  | 33        |
| 4.5      | External vs. Internal Bosonic Josephson Junctions . . . . .                    | 34        |
| 4.6      | Experimental Sequence and State Readout . . . . .                              | 35        |
| 4.7      | Observation of the Topological Change . . . . .                                | 36        |
| 4.8      | Measurement of the Phase Portrait . . . . .                                    | 37        |

|          |  |           |
|----------|--|-----------|
| 4.9      | The Temporal Behavior of the Dynamics . . . . .  | 39        |
| <b>5</b> | <b>Quantum Behavior at the Unstable Classical Fixed Point</b>                              | <b>41</b> |
| 5.1      | Spin Squeezing . . . . .   | 43        |
| 5.1.1    | Number Squeezing and the Standard Quantum Limit . . . . .                                  | 44        |
| 5.1.2    | Improvement of Interferometry using Spin Squeezed States . . . . .                         | 44        |
| 5.1.3    | Entanglement and Squeezing . . . . .   | 45        |
| 5.2      | Systematic Measurements of the Dynamical Spin Squeezing . . . . .                          | 45        |
| 5.3      | Quantum Fisher Information . . . . .   | 49        |
| 5.4      | State Tomography . . . . .   | 51        |
| 5.4.1    | Wigner Distribution on the Bloch Sphere . . . . .  | 52        |
| 5.4.2    | Reconstruction of the Wigner Function by a Filtered Back<br>Projection Algorithm . . . . . | 53        |
| 5.4.3    | Maximum Likelihood Estimation of the Density Matrix . . . . .                              | 54        |
| 5.5      | Relevance of the Experimental Imperfections . . . . .                                      | 56        |
| 5.5.1    | Detuning Noise and Spin Echo . . . . .   | 57        |
| 5.5.2    | The Influence of Atom Loss . . . . .   | 58        |
| 5.6      | Numerical Simulation . . . . .   | 60        |
| <b>6</b> | <b>Summary of the Results and Outlook</b>  | <b>63</b> |
| <b>A</b> | <b>Histograms of the Squeezing Measurements</b>  | <b>65</b> |
| <b>B</b> | <b>Full Data Entering the Measured Wigner Functions</b>                                    | <b>67</b> |

# List of Figures

|      |  |    |
|------|--|----|
| 2.1  | Husimi distribution of a coherent spin state and a Dicke state . . . . .                               | 8  |
| 2.2  | Velocity field associated with the linear coupling . . . . .   | 9  |
| 2.3  | Velocity field associated with the nonlinearity . . . . .  | 10 |
| 2.4  | Canceling of the linear coupling and the nonlinearity on the backside of the sphere . . . . .          | 11 |
| 2.5  | Add up of the linear and nonlinear terms on the frontside of the sphere                                | 12 |
| 3.1  | The electronic groundstate of $^{87}\text{Rb}$ . . . . .   | 14 |
| 3.2  | Schematic illustration of the experimental setup . . . . .   | 15 |
| 3.3  | Absorption images in the different trapping configurations . . . . .                                   | 16 |
| 3.4  | The nonlinearity depending on the magnetic field close to the Feshbach resonance . . . . .             | 18 |
| 3.5  | Comparison of the ground state probability densities for different partition of the atoms . . . . .    | 20 |
| 3.6  | The gradient in the linear coupling Rabi frequency . . . . .   | 26 |
| 4.1  | Husimi representation of coherent spin states with different atom numbers . . . . .                    | 28 |
| 4.2  | The phase plane portrait of the classical Hamiltonian . . . . .  | 29 |
| 4.3  | Pendulum performing plasma oscillations . . . . .  | 30 |
| 4.4  | Macroscopic quantum self trapped pendulum . . . . .  | 31 |
| 4.5  | $\pi$ -self-trapped pendulum . . . . .   | 31 |
| 4.6  | $\pi$ -oscillations in the classic pendulum . . . . .  | 32 |
| 4.7  | Topological difference between bosonic Josephsen junctions and their superconducting analogs . . . . . | 33 |
| 4.8  | Influence of a detuning on the classical dynamics . . . . .  | 34 |
| 4.9  | Experimental evidence of the topological change . . . . .  | 36 |
| 4.10 | Measured phase portraits of the classical mean field dynamics . . . . .                                | 38 |
| 4.11 | Time dependence of the classical observables . . . . .   | 39 |
| 5.1  | <i>Quantum mechanical</i> inverted pendulum . . . . .  | 41 |
| 5.2  | Quantum evolution of a coherent spin state at the unstable fixed point                                 | 42 |
| 5.3  | Number squeezing versus measurement direction . . . . .  | 46 |
| 5.4  | Squeezing vs. time . . . . .   | 47 |
| 5.5  | Uncertainty product and angle of minimal uncertainty vs. time . . . . .                                | 48 |
| 5.6  | Possible precision gain in terms of coherent spin squeezing and Fisher information . . . . .           | 49 |
| 5.7  | State tomography via different measurement directions . . . . .  | 51 |

|      |   |    |
|------|---|----|
| 5.8  | Wigner distributions of a coherent spin state and exemplary macroscopic superposition state . . . . . | 52 |
| 5.9  | Measured Wigner distribution via filtered back projection . . . . .                                   | 54 |
| 5.10 | Measured Wigner distribution via maximum likelihood estimated density matrix . . . . .                | 55 |
| 5.11 | Comparison of the effect of detuning noise with and without spin echo                                 | 57 |
| 5.12 | Fluctuations in the effective nonlinearity due to atom loss . . . . .                                 | 59 |
| A.1  | Measured histograms of the squeezing data . . . . .   | 66 |
| B.1  | Full set of tomographic data higher Rabi frequency . . . . .  | 68 |
| B.2  | Full set of tomographic data lower Rabi frequency . . . . .   | 69 |

# Chapter 1

## Introduction

Since the advent of quantum mechanics physicists have been puzzled by its interpretation. The most fundamental difference between the classical and the quantum world is the existence of superposition states in the latter. A physical system which resides in such a quantum superposition state shows at least in one of its properties a literally surprising behavior. If one performs a repeated measurement of this property one gets differing and completely unpredictable results, even if the system is in the exact same physical state before the individual measurements are carried out. Perfect knowledge about the quantum state of a system does not necessarily imply the predictability of measurement results.

While one might find this fact acceptable for very small systems, like qubits, where the different measurement results differ only slightly in their physical consequence, on a macroscopic scale this effect is completely counterintuitive. This is most famously illustrated by Schrödinger's gedankenexperiment on a cat in a box, where the superposition state of a microscopic system is transferred to the health status of the cat [1, 2, 3]. Since this experiment is completely valid in the framework of quantum mechanics the question arises why we do not encounter similar situations in every day life? The answer to this question is surprisingly not found in the complex mechanism, that kills the cat, but in the box containing the whole apparatus. The fact that the superposition state of the cat survives until one opens the box depends crucially on the isolation from the outside world, i.e. the quality of the box.

The experimental investigation of macroscopic superpositions therefore relies on systems which are highly isolated against decoherence with their environment. These properties are found in neutral Bose-Einstein condensed atomic systems. A promising scheme to generate and investigate macroscopic superposition states in Bose-Einstein condensates is found in the bosonic Josephson junction.

### Bosonic Josephson Junctions

Since the first realization of Bose-Einstein condensation in alkali gases [4] the experimental techniques have grown substantially [5]. Two of these advances are especially important for this work. The use of purely optical traps for the atoms allows to use the spin of the atoms as a very well controllable degree of freedom [6]. Further Feshbach resonances allow to tune the nonlinear interaction among the atoms in the

---

condensate [7].

These two techniques are the main ingredients for the realization of an internal bosonic Josephson junction. The idea to implement Josephson like physics in a system of two weakly coupled Bose-Einstein condensates dates long before the experimental realization of Bose-Einstein condensed alkali gases [8]. In an internal bosonic Josephson junction the distinguishing parameter between the two condensates is found in their internal spin degree of freedom, in contrast to the spatial difference found for instance in the superconducting analog [9].

The possibility of tight optical confinement of the condensates in the same trap allows to simplify the description of the system's dynamics considerably. The external degrees of freedom of the two condensate are not involved in the dynamics, and the system can be described by the formalism of a large spin. This simple description makes the system an ideal toy model for the investigation of the dynamics of many-particle systems, which is underlined by the fact that the Hamiltonian describing the system's dynamics is equivalent to a special case of the Lipkin-Meshkov-Glick Hamiltonian. This Hamiltonian was theoretically constructed by Lipkin, Meshkov and Glick with the purpose of having an in some cases exactly solvable model system which allows for the test of the validity of many-particle methods [10, 11, 12].

In this work we focus on two main aspects of the dynamics of the internal bosonic Josephson junction. The first is its classical behavior. Since the number of particles in our system is on the order of several hundred the dynamics are typically well described by a mean field approach leading to classical equations of motion [13, 14]. It turns out that depending on the relative interplay of the different dynamical contributions the system undergoes a bifurcation. We investigate the topological change associated with this bifurcation experimentally, which is special for the bosonic Josephson junction and not found in its superconducting analog. The high level of experimental control of the system allows us to investigate all aspects of the dynamics across the bifurcation.

In the process of this bifurcation an unstable fixed point arises in the classical dynamics. This raises the question of the quantum mechanical behavior at this classical fixed point which is the second aspect of this work. It turns out that the classical mean field description breaks down even on short timescales, when the system is prepared at the unstable fixed point. We will show that the quantum dynamics at this classical fixed-point lead to a squeezing of the spin state. This property is directly related to many-particle entanglement and a possible precision improvement of an atomic interferometer. The dynamics at the unstable fixed point further lead to the generation of a macroscopic superposition state of the system on an experimentally feasible time scale [15]. We investigate this scenario by tomographic measurements on the state which allow us to reconstruct the Wigner function of the many particle state.

# Chapter 2

## A Pair of Linearly Coupled Bose-Einstein Condensates

In this chapter the theoretical description of two weakly linked Bose-Einstein condensed atomic systems (BEC) will be given. This description can be in our case greatly simplified by assuming constant spatial wave functions of the two BECs. It will be discussed how this assumption breaks down the dynamical description of the many body system to that of a macroscopic spin built up of many small spin-1/2 systems. The properties of this spin can be visualized via its Husimi distribution on a sphere in close analogy to the Bloch sphere, which allows for an intuitive interpretation of the system's dynamics.

### 2.1 Two Linearly Coupled Interacting BECs

We will start our description by its Hamiltonian given in second quantized form. Following [16, 17], the Hamiltonian for two linearly coupled interacting BECs takes the form,

$$\hat{H} = \hat{H}_1 + \hat{H}_2 + \hat{H}_{\text{int}} + \hat{H}_{\text{cpl}}, \quad (2.1)$$

with

$$\begin{aligned} \hat{H}_k &= \int d^3\mathbf{x} \hat{\psi}_k^\dagger(\mathbf{x}) \left[ -\frac{\hbar^2}{2m} \nabla^2 + V_k(\mathbf{x}) + \frac{4\pi\hbar^2 a_{kk}}{2m} \hat{\psi}_k^\dagger(\mathbf{x}) \hat{\psi}_k(\mathbf{x}) \right] \hat{\psi}_k(\mathbf{x}), \\ \hat{H}_{\text{int}} &= \frac{4\pi\hbar^2 a_{12}}{m} \int d^3\mathbf{x} \hat{\psi}_1^\dagger(\mathbf{x}) \hat{\psi}_2^\dagger(\mathbf{x}) \hat{\psi}_1(\mathbf{x}) \hat{\psi}_2(\mathbf{x}), \\ \hat{H}_{\text{cpl}} &= -\frac{\hbar\eta}{2} \int d^3\mathbf{x} \left[ \hat{\psi}_1(\mathbf{x}) \hat{\psi}_2^\dagger(\mathbf{x}) e^{-i\delta t} + \hat{\psi}_1^\dagger(\mathbf{x}) \hat{\psi}_2(\mathbf{x}) e^{i\delta t} \right], \end{aligned}$$

where  $k = 1, 2$  denotes the condensate in the potential  $V_k$ ,  $m$  is the mass of the particles and the field operators  $\hat{\psi}_k(\mathbf{x})$  annihilate an atom in the respective condensate at position  $\mathbf{x}$ . The field operators fulfill the standard bosonic commutation relations  $[\hat{\psi}_k(\mathbf{x}), \hat{\psi}_l(\mathbf{x}')] = \delta_{lk} \delta(\mathbf{x} - \mathbf{x}')$ . The parts  $\hat{H}_1$  and  $\hat{H}_2$  of the Hamiltonian describe the two condensates in the absence of the other condensate where the three terms in the integral correspond to the kinetic energy, potential energy and the interaction energy arising from elastic collisions within the condensate. The third part  $\hat{H}_{\text{int}}$  of the Hamiltonian describes the interaction among the two condensates

due to elastic collisions between the two species. The three interaction terms in the Hamiltonian are parametrized by the elastic s-wave scattering lengths  $a_{11}$ ,  $a_{22}$  and  $a_{12}$ . The linear coupling between the two condensates is described by the last part of the Hamiltonian  $\hat{H}_{\text{cpl}}$ . This part leads to an interconversion of atoms between the two condensates with a Rabi frequency of  $\eta$  and a detuning parameter  $\delta$ .

This Hamiltonian can be significantly simplified by the assumption that internal dynamics have no influence on the external degrees of freedom. In the relevant case where the two condensates are situated in the same trap and have the same wave function the assumption is often referred to as single mode approximation. The motivation for its validity will be given later in section 3.6. The assumption implies that the field operators can be written as

$$\hat{\psi}_1(\mathbf{x}) = \hat{a}_1\phi_1(\mathbf{x}) \quad \hat{\psi}_2(\mathbf{x}) = \hat{a}_2\phi_2(\mathbf{x}) \quad (2.2)$$

with real normalized wave functions  $\phi_k$  and annihilation operators  $\hat{a}_k$  which fulfill the commutation relations  $[\hat{a}_k, \hat{a}_l] = 0$ ,  $[\hat{a}_k, \hat{a}_l^\dagger] = \delta_{kl}$ . This assumption leads to

$$\begin{aligned} \hat{H} = & \hbar\omega_1\hat{a}_1^\dagger\hat{a}_1 + \hbar\omega_2\hat{a}_2^\dagger\hat{a}_2 + \hbar\chi_{11}\hat{a}_1^\dagger\hat{a}_1^\dagger\hat{a}_1\hat{a}_1 + \hbar\chi_{22}\hat{a}_2^\dagger\hat{a}_2^\dagger\hat{a}_2\hat{a}_2 \\ & + 2\hbar\chi_{12}\hat{a}_1^\dagger\hat{a}_1\hat{a}_2^\dagger\hat{a}_2 + \hbar\frac{\eta}{2}(\hat{a}_1\hat{a}_2^\dagger + \hat{a}_1^\dagger\hat{a}_2) \end{aligned} \quad (2.3)$$

,

with

$$\omega_k = \int d^3\mathbf{x}\phi_k(\mathbf{x})\left[-\frac{\hbar}{2m}\nabla^2 + \frac{1}{\hbar}V_k\right]\phi_k(\mathbf{x}), \quad (2.4)$$

$$\chi_{kk} = \frac{4\pi\hbar a_{kk}}{2m} \int d^3\mathbf{x}|\phi_k(\mathbf{x})|^4, \quad (2.5)$$

$$\chi_{12} = \frac{4\pi\hbar a_{12}}{2m} \int d^3\mathbf{x}|\phi_1(\mathbf{x})|^2|\phi_2(\mathbf{x})|^2, \quad (2.6)$$

$$\Omega = \eta \int d^3\mathbf{x}\phi_1(\mathbf{x})\phi_2(\mathbf{x}). \quad (2.7)$$

The  $\omega_k$  denote the sum of kinetic and potential energy of the individual BECs. The nonlinearities  $\chi_{kl}$  correspond to the additional energy from the self and cross interaction of the two BECs. The effective Rabi frequency  $\Omega$  is proportional to the mode overlap of the two condensates. The total atom number  $\hat{N} = \hat{a}_1^\dagger\hat{a}_1 + \hat{a}_2^\dagger\hat{a}_2$  commutes with the Hamiltonian and is therefore a conserved quantity of the system.

Regarding a single atom in such a system, the assumption of constant external modes restricts the dynamics to a two-mode system which can be translated into a spin-1/2 system. It is therefore natural to describe the system in terms of angular momentum operators, as will be detailed in the following.

## 2.2 Angular Momentum Operators

With the assumption of constant external modes the description of a single atom can be reduced to the two dimensional Hilbert space of a spin-1/2 particle.

Schwinger developed a description of a system of two harmonic oscillators in terms of angular momentum operators[18, 19]. The excitation of the individual

oscillators can be associated with the number of particles in the two modes. The operator  $\hat{N} = \hat{a}_1^\dagger \hat{a}_1 + \hat{a}_2^\dagger \hat{a}_2$  corresponds to the total number of excitations respectively particles in the two modes and  $\hat{J}_z = \frac{1}{2}(\hat{a}_2^\dagger \hat{a}_2 - \hat{a}_1^\dagger \hat{a}_1)$  is proportional to the particle number difference. The latter can be understood as the  $z$ -component of a collective angular momentum of the  $N$  particle system. The corresponding set of angular momentum operators is given by

$$\hat{J}_x = \frac{1}{2} \sum_{j=1}^N \sigma_x^{(j)} = \frac{1}{2}(\hat{a}_1 \hat{a}_2^\dagger + \hat{a}_1^\dagger \hat{a}_2), \quad (2.8)$$

$$\hat{J}_y = \frac{1}{2} \sum_{j=1}^N \sigma_y^{(j)} = \frac{1}{2i}(\hat{a}_1 \hat{a}_2^\dagger - \hat{a}_1^\dagger \hat{a}_2), \quad (2.9)$$

$$\hat{J}_z = \frac{1}{2} \sum_{j=1}^N \sigma_z^{(j)} = \frac{1}{2}(\hat{a}_2^\dagger \hat{a}_2 - \hat{a}_1^\dagger \hat{a}_1), \quad (2.10)$$

$$\hat{J}^2 = \hat{J}_x^2 + \hat{J}_y^2 + \hat{J}_z^2. \quad (2.11)$$

Here the  $\sigma_{x,y,z}^{(j)}$  denote the Pauli operators associated with the spin of particle  $j$ . The first part of each equation shows the composite character of the system from the single particle spins, where the latter equation shows the relation to creating and annihilating particles in the two modes.

With this relation it is possible to express the Hamiltonian for a given total atom number  $N$  in terms of the corresponding angular momentum operators. By rearranging the terms and neglecting all constant terms one obtains

$$\hat{H} = \hbar\chi\hat{J}_z^2 + \hbar\Omega\hat{J}_x + \hbar\Delta\hat{J}_z, \quad (2.12)$$

with the effective nonlinearity

$$\chi = \chi_{11} + \chi_{22} - 2\chi_{12}, \quad (2.13)$$

and the effective detuning

$$\Delta = \omega_1 - \omega_2 + \delta + (2J - 1)(\chi_{22} - \chi_{11}). \quad (2.14)$$

This shows that the external degrees of freedom of the system are completely absorbed into the parameters of the Hamiltonian and that the dynamics of the  $N$ -particle system can be understood as those of a large spin.

## 2.3 Hilbert Space and Number State Basis

The system is formally equivalent to a combination of  $N$  spin-1/2 systems so the most general Hilbert space is given by the  $2^N$  dimensional product space. However the bosonic character of the  $N$  identical particles restricts the dynamics to the Hilbert subspace which is totally symmetric. In this subspace the spins of the individual particles couple to the maximum possible spin  $J = \frac{1}{2}N$  [20, 19]. A natural basis is therefore given by the eigenstates  $|N, n\rangle$  of both  $\hat{\mathbf{J}}^2$  and  $\hat{J}_z$  where

the quantum numbers denote the total atom number and half the atom number difference  $n = \frac{1}{2}(N_2 - N_1)$  respectively. These states are called symmetric Dicke or number states and are the direct analog to Fock states in quantum optics [20]. They can be defined as

$$|N, n\rangle = \frac{1}{\sqrt{(N/2 + n)!(N/2 - n)!}} (\hat{a}_1^\dagger)^{N/2-n} (\hat{a}_2^\dagger)^{N/2+n} |0, 0\rangle,$$

where  $|0, 0\rangle$  is the vacuum of the two modes.

This basis is also a natural choice since it forms the basis of the measurements performed on the system. The total atom number and the individual atom numbers in the two modes are the main observables of the system.

## 2.4 Coherent Spin States

Although the number states as defined above give a basis of the Hilbert space of the system, their properties make them a choice that is often far away from the states found in the experiment. This is in direct analogy to the Fock states in quantum optics where the set of coherent states is often more appropriate to describe the state of the light. In this section we will therefore introduce the coherent spin states (CSS) as their analog in the spin system. The CSS are states that are built up as the direct product of single spin-1/2 states. The bosonic symmetry only allows that these single spin-1/2 states are all the same. This leads to the following definition of the CSS

$$|N, \vartheta, \varphi\rangle = \left( \cos \frac{\vartheta}{2} |\uparrow\rangle + \sin \frac{\vartheta}{2} e^{i\varphi} |\downarrow\rangle \right)^{\otimes N}, \quad (2.15)$$

where the states  $|\uparrow\rangle$  and  $|\downarrow\rangle$  correspond to the respective spin-1/2 states. It can be easily verified that all fully symmetric states which are separable can be parametrized in this way and are therefore CSS.

The CSS can also be written in the number state basis defined before, taking the form

$$|N, \vartheta, \varphi\rangle = \sum_{n=-N/2}^{N/2} \sqrt{\binom{N}{N/2+n}} \cos^{N/2-n} \left(\frac{\vartheta}{2}\right) \sin^{N/2+n} \left(\frac{\vartheta}{2}\right) e^{-in\varphi} |N, n\rangle,$$

where the binomial coefficients  $\binom{N}{N/2+n}$  appear in the respective absolute amplitudes of the number states. This can be understood from another point of view: the spin-1/2 systems are separable, thus uncorrelated. The projection onto a number state  $|N, n\rangle$  gives the probability to find exactly  $2n$  of the spins in the excited  $|\uparrow\rangle$  state. For an uncorrelated ensemble of spin-1/2 this can be seen as a repeated coin toss [21]. The binomial coefficients give the multiplicity while the trigonometric terms are the probabilities to be excited or not, i.e. heads or tails.

It is important to note that the number states  $|N, N/2\rangle$  and  $|N, -N/2\rangle$  are exactly the coherent spin states  $|N, 0, 0\rangle$  and  $|N, \pi, 0\rangle$  respectively. These extremal states which correspond to the situations where all atoms are found in the same mode of the system are the only states that are both CSS and number states in a

given number state basis. However for a general number state basis defined as the eigenstates of  $\hat{\mathbf{J}}^2$  and the general angular momentum operator

$$\hat{J}_{\vartheta,\varphi} = \sin \vartheta \cos \varphi \hat{J}_x + \sin \vartheta \sin \varphi \hat{J}_y + \cos \vartheta \hat{J}_z, \quad (2.16)$$

the extremal states with eigenvalue  $N/2$  and  $-N/2$  are the CSS  $|N, \vartheta, \varphi\rangle$  and  $|N, \vartheta + \pi, \varphi\rangle$  respectively. For all angular momentum operators  $\hat{J}_{1\perp}, \hat{J}_{2\perp}$  satisfying  $[\hat{J}_{1\perp}, \hat{J}_{2\perp}] = \pm i \hat{J}_{\vartheta,\varphi}$  these coherent spin states are Heisenberg limited. Meaning that they minimize the uncertainty product in the corresponding Heisenberg uncertainty relation

$$\Delta \hat{J}_{1\perp} \cdot \Delta \hat{J}_{2\perp} \geq \frac{1}{2} \left| \langle \hat{J}_{\vartheta,\varphi} \rangle \right| = \frac{N}{4} \quad (2.17)$$

This property shows that the CSS are the states which are most localized and isotropic around their mean. Due to these properties and their separability, the CSS are regarded as the classical states of the system. From the equation one can further see that the relative uncertainty of the angular momentum operators shrinks with growing atom number as  $1/\sqrt{N}$ . Therefore one expects that for very high atom numbers the quantum uncertainties become irrelevant and the many-particle system can be described in its classical limit which will be discussed in detail in section 4.1.

The CSS are also special in terms of their transformation under unitary rotations. Two different CSS can be always transformed into each other by a unitary rotation and CSS stay CSS under every unitary rotation. This property shows that the separability and the minimality of a state is conserved by rotations. It can be also used for a definition of the general CSS by

$$|N, \vartheta, \varphi\rangle = e^{-i\varphi \hat{J}_z} e^{-i\vartheta \hat{J}_y} |N, N/2\rangle \quad (2.18)$$

which is the rotation of the coherent spin state corresponding to all particles in the second mode by  $\vartheta$  around the  $y$ -axis and subsequently by  $\varphi$  around the  $z$ -axis. These transformation properties are important in the experiment to prepare and readout the state of the system as described in section 4.6. The following discussion of the Husimi distribution will show a nice visual interpretation of many of the features of the CSS which have been described here.

## 2.5 Bloch Sphere and Husimi Representation

As discussed in section 2.2, the assumption of constant spatial wave functions leads to a description where the Hamiltonian of the system is given by a combination of collective angular momentum operators. These operators can be understood as sums of the individual spin-1/2 operators.

The general state vector of a single spin-1/2 particle can be written as

$$|\vartheta, \varphi\rangle = \cos \frac{\vartheta}{2} |\uparrow\rangle + \sin \frac{\vartheta}{2} e^{i\varphi} |\downarrow\rangle \quad (2.19)$$

where  $|\uparrow\rangle$  and  $|\downarrow\rangle$  are the corresponding eigenstates along the quantization axis. This parametrization by two angles suggests the representation of the spin state as a point on the surface of a unity sphere, the so called Bloch sphere [22].

The Bloch sphere picture also allows for a very nice interpretation of the dynamics of the system. Since the spin operators in form of the Pauli matrices together with the identity operator span the full vector space of  $2 \times 2$  Hermitian matrices every Hamiltonian describing the dynamics of the system can be expressed in terms of those. These operators are the generators of rotations. Therefore all possible dynamics of the system correspond to a rotation of the surface of the sphere. This picture allows for a simple understanding of the dynamical behavior of arbitrary initial state vectors.

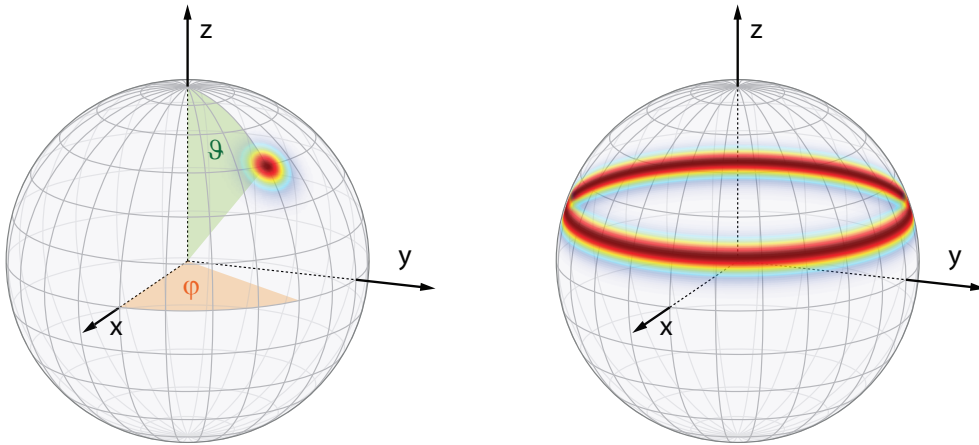


**Figure 2.1:** Husimi distribution of a coherent spin state  $|300, \vartheta, \varphi\rangle$  (left) and a number or Dicke state (right). In both cases the total atom number is 300. The Husimi distribution allows to illustrate many of the physical properties of the many-particle state.

For the  $N$  particle system with its  $N + 1$  dimensional Hilbert space a state vector can no longer be visualized as a point on the sphere. However, the definition of the coherent spin states, which are the most localized states in a given direction, allows one to calculate a probability distribution on the sphere that measures the overlap of the state with a coherent spin state in a given direction. It can be defined in a more general way for a density operator  $\hat{\rho}$  as

$$Q(\vartheta, \varphi) = \langle N, \vartheta, \varphi | \hat{\rho} | N, \vartheta, \varphi \rangle. \quad (2.20)$$

This probability distribution<sup>1</sup> is known as Husimi or Q-representation. Two examples of the Husimi distributions for a CSS and a number state can be seen in figure 2.1. The Husimi distribution in these two examples visualizes many of the properties of the two states. The example of the CSS shows the narrow symmetric distribution which is peaked at  $(\vartheta, \varphi)$  on the sphere. The number state shows its undefined phase in the sense that there is no maximum of the distribution along its latitude. The projection of the maximum onto the quantization axis indicates the distribution of the atoms into the two modes of the system.

<sup>1</sup>To be a probability distribution the Husimi distribution has to be normalized  $\int_0^{2\pi} \int_0^\pi Q(\vartheta, \varphi) \sin \vartheta d\vartheta d\varphi = 1$ .

While a lot of physical properties of the state can be directly seen from its graphical Husimi representation, many properties are hidden. For example, the distribution of the number state suggests a finite width in the  $\hat{J}_z$  direction while the true variance is zero. Nevertheless the Husimi distribution  $Q(\vartheta, \varphi)$  is a complete representation of the state's density matrix, one only has to keep in mind that its graphical illustration should not be taken in all its aspects as a representation of the physical properties of the state.

However the Husimi representation allows one to develop a picture of the many body dynamics in the system which will be explained in the following section.

## 2.6 Pictorial Interpretation of the Hamiltonian

This section will provide a basic understanding of the dynamics induced by the Hamiltonian 2.12. We will focus on the simplified situation where the detuning  $\Delta$  in the Hamiltonian is negligible. This describes the ideal physical evolution, which is typically achieved to a good approximation in our experiments. This simplifies the Hamiltonian leaving only the interaction term, which is quadratic in the angular momentum operator, and the linear coupling term. As discussed in the section before the states of the system can be associated to a probability distribution on the sphere. The dynamics of the system correspond to a redistribution of this probability distribution on the surface of the sphere.

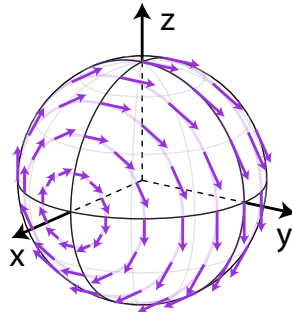


**Figure 2.2:** Velocity field associated with the linear coupling. The arrows indicate the velocity at their origin.

The angular momentum operators are generators of unitary rotations. As discussed in section 2.4 a rotation transforms a CSS into another CSS. The CSS form the basis of the Husimi distribution, it is therefore natural that the linear coupling term leads to a rotation of the distribution on the sphere around the  $x$ -axis with constant angular velocity  $\Omega$ . The radial velocity field associated with this rotation is shown in figure 2.2.

While it is easy to prove that linear angular momentum terms in the Hamiltonian correspond exactly to a rotation of the Husimi representation around the respective axis, a correspondence for higher order terms is neither obvious nor exact. However, one can ask what is the differential rotation induced by to the higher order terms to get a feeling how these redistribute the probability distribution on the sphere.

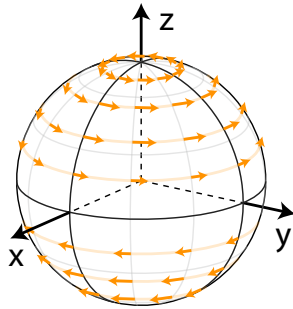


**Figure 2.3:** Radial velocity field associated with the nonlinear interaction

This can be done by looking at the dynamics of the CSS instead of looking at the dynamics of the density matrix of the system. It turns out that the nonlinear interaction which is quadratic in  $\hat{J}_z$  leads to

$$e^{-i\chi\hat{J}_z^2 dt}|N, \vartheta, \varphi\rangle \sim e^{-i\frac{N}{2}\cos(\vartheta)\chi\hat{J}_z dt}|N, \vartheta, \varphi\rangle = |N, \vartheta, \varphi + \frac{N}{2}\cos(\vartheta)\chi dt\rangle \quad (2.21)$$

This corresponds to a rotation around the  $z$ -axis with an angular velocity proportional to the expectation value in  $z$ -direction of the corresponding CSS. This velocity field is illustrated in figure 2.3. The latitude dependence leads to a shearing of the state distribution. By this the circular uncertainty distribution of a CSS is transformed into an elliptical one. This effect is called one-axis twisting and leads to spin squeezed states. These states offer a reduced quantum uncertainty in a certain direction and can be used to improve the sensitivity of linear interferometers [23, 24, 25]. This will be discussed in more detail in section 5.1.2.

The corresponding velocity fields of the two terms in the Hamiltonian can be understood as the extreme case of the Hamiltonian where one of the terms dominates over the other. This work however focuses on the dynamics initiated by the interplay between both terms, the linear coupling and the nonlinear interaction. Although the dynamics under the simultaneous influence of both terms are much more complicated, the velocity fields allow one to deduce the most important features.

Both velocity fields have several fixed points, i.e. points on the sphere where the velocity is zero. For the linear interaction these are the two points on the  $x$ -axis while for the nonlinear interaction we find the two points on the  $z$ -axis corresponding to the north and south pole of the sphere. In addition, all the points on the equator of the sphere are fixed for the nonlinear interaction due to the dependence of the velocity on the latitude. This makes the two polar points on the  $x$ -axis common fixed points of the dynamics.

However, these are not necessarily the only fixed points. A closer look on the back side of the sphere shows that the velocities of the two terms counteract each other at some points (see figure 2.4). The velocities of both fields at points with  $y = 0$  are parallel to the  $y$ -axis but anti parallel to each other which leads to a cancellation of the two fields, which depends on the strength of the two terms relative to each other. The two fields completely cancel each other if the absolute velocities of both

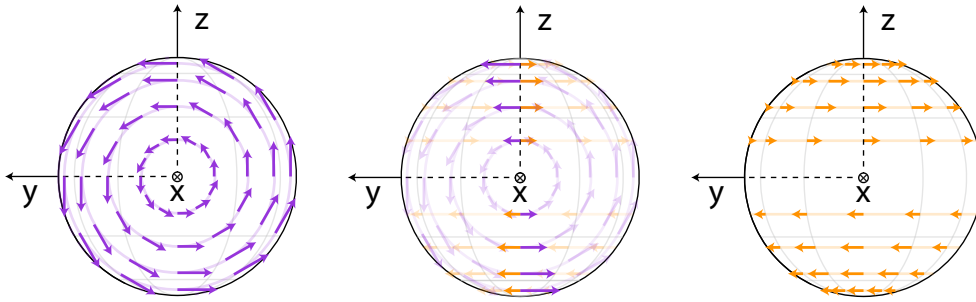


**Figure 2.4:** Radial velocity fields corresponding to the coupling (left) and nonlinearity (right) and their combination (middle) as seen from the back side of the sphere. In the middle panel the velocities at points with phase  $\pi$  are emphasized. Here the velocities are anti parallel and can cancel each other. Depending on their relative strength one finds a pair of points symmetrically above and below the equator where they perfectly cancel, i.e. a fixed point in the combined dynamics. Independent of the relative strength of the two parts the point on the  $x$ -axis is a point with zero velocity and therefore a fixed point in the dynamics.

fields are the same at a particular point on the sphere. From the considerations before this is the case if

$$\sin \vartheta = \frac{\Omega}{\chi N}, \quad (2.22)$$

which can only be fulfilled for  $\Omega < N\chi$ . This shows that the ratio of  $\chi N$  and  $\Omega$  determines whether there are two or four fixed points in the dynamics of the system. Due to its important role, this ratio will be defined as

$$\Lambda = \frac{\chi N}{\Omega}. \quad (2.23)$$

In a classical system the change of the number of fixed points is described by a bifurcation. This change happens in our system at the critical parameter  $\Lambda = 1$ .

The view of the velocity fields from the other side (see figure 2.5) shows that, here the two fields do not counteract each other but add up. This can be directly understood from the symmetry of the two terms. The velocity field of the nonlinear interaction is intrinsically symmetric around the  $z$ -axis while that of the linear coupling is not, which leads to a counteraction only on one side of the sphere depending on the signs of  $\Omega$  and  $\chi$ . In our experiments  $\Omega$  and  $\chi$  are positive, which makes the hemisphere with  $x < 0$  the part of the phase space where the bifurcation occurs due to the counteraction of the two terms. We will also refer to this side as the  $\pi$  side of the sphere.

The interpretation of the Hamiltonian dynamics in terms of the corresponding velocity fields allows one to make further conclusions about the temporal behavior of the dynamics. While the dynamics associated with the coupling and the nonlinearity constructively or destructively add up on the two sides of the sphere we expect generally a slower dynamical behavior on the  $\pi$  side. This will be further discussed in section 4.9 and also used to experimentally determine the size of the nonlinearity by a frequency measurement as discussed in section 3.5.

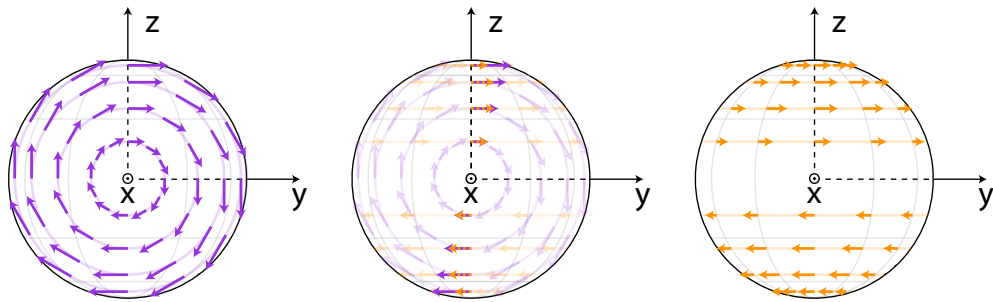


**Figure 2.5:** Radial velocity fields corresponding to the coupling (left) and non-linearity (right) and their combination (middle) as seen from the front side of the sphere. Here the velocities at points with  $y = 0$  do not cancel but add up in contrary to the other side of the sphere (see figure 2.4). This different behavior on the two sides of the sphere stems from the different symmetry of the linear coupling term and the quadratic nonlinear term in the Hamiltonian. Again the point on the  $x$ -axis is a fixed point with zero velocity independent on the strength of the two terms.

# Chapter 3

## Experimental Realization of the Internal Bosonic Josephson Junction

In this chapter we present an overview how the system is experimentally realized. We further discuss general experimental limitations affecting both the experiments on the classical mean field dynamics as well as the experiments dealing with the quantum mechanical behavior of the system. Since the experiments have been performed on an apparatus that has been setup over the last ten years, we will focus our discussion on the experimental details which are most relevant for this work. A more detailed discussion about the technical aspects of the apparatus can be found in the references [26, 27, 28].

### 3.1 The Atomic Two-state System

We begin our discussion on the experimental realization by introducing our physical system. A two-mode BEC system forming a bosonic Josephson junction can be either implemented using external degrees of freedom, which allows one to distinguish the atoms by their location or spatial mode, or one can use internal degrees of freedom such as the spin of the atoms as a distinguishing attribute. Of course a combination of both can also be used as has been demonstrated in [24].

In this work, the two modes of the system are realized by the spin of the atoms, forming an internal Josephson junction. Figure 3.1 shows the Zeeman levels of the two hyperfine manifolds of the ground state of  $^{87}\text{Rb}$ . The energy difference between these two manifolds is approximately 6.8 GHz while the energy scale of the linear Zeeman effect is typically much smaller with a sensitivity of  $\sim 700\text{kHz/G}$ . The two spin states used here are the  $|F, m_f\rangle = |1, 1\rangle$  and  $|2, -1\rangle$  as shown in figure 3.1. These states are chosen for several reasons. The main reason is that a Feshbach resonance at relatively small magnetic fields allows one to tune the interspecies scattering length of the atoms. This is a prerequisite for getting significant nonlinearities  $\chi$  in the system as discussed in section 3.5. A second reason is that the linear Zeeman effect shifts both energy levels equally. The resulting low sensitivity to magnetic fields is important for having a long coherence time as discussed in section 3.8.2. A nice property of using ground state Zeeman states is that commercial microwave and radio frequency sources can be used to realize the coupling between the two

states as is explained in more detail in section 3.4.

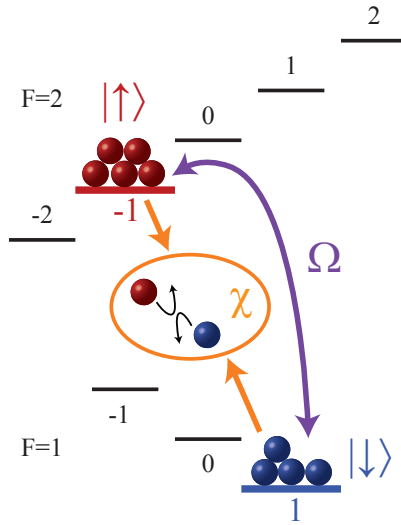


**Figure 3.1:** Schematic illustration of the electronic ground state of  $^{87}\text{Rb}$ . The two hyperfine manifolds  $F = 1$  and  $F = 2$  are shown with their Zeeman sublevels. The two Zeeman states  $|F, m_F\rangle = |1, 1\rangle$  and  $|2, -1\rangle$  forming our two-level system are blue and red respectively. The main parameters determining the system's dynamics are the linear coupling  $\Omega$  by a two photon transition via the  $|2, 0\rangle$  state and the nonlinear interaction  $\chi$  originating from inter atomic collisions.

## 3.2 Creating a Bose-Einstein Condensate

The creation of the  $^{87}\text{Rb}$ -BEC we employ standard techniques of cold atom physics [29]. A three-dimensional magneto-optical trap (3D-MOT) in ultrahigh vacuum is loaded by a cold beam of atoms. This beam originates from a two-dimensional magneto-optical trap in a part of the vacuum system with room temperature rubidium vapour pressure. The atoms in the 3D-MOT are then further cooled in an optical molasses and subsequently trapped in a magnetic trap. This trap uses the same pair of coils used for the 3D-MOT but with an additional time orbiting field preventing Majorana spin flips [30]. In this trap the atomic ensemble is evaporatively cooled close to the BEC phase transition. For the creation of a spin polarized BEC in the  $F = 1$  hyperfine manifold, the atoms are optically pumped into the lower hyperfine state during the molasses and residual atoms in the  $F = 2$  manifold are heated out of the trap in the beginning of the evaporative cooling by a short pulse of resonant light. With the  $|F, m_F\rangle = |1, -1\rangle$  state being the only remaining trapable low-field seeking state, one ends up with a spin-polarized ensemble of atoms. These atoms are then transferred into an optical dipole trap where they are further cooled below the critical temperature forming a BEC. The optical confining potential traps atoms in all spin states of the ground state manifold. This allows to use a chirped magnetic radio frequency pulse for a rapid adiabatic passage to the  $|1, +1\rangle$  state. The residual fraction of atoms in the  $|1, -1\rangle$  and  $|1, 0\rangle$  states is close

to zero and below our detection limit. Regarding the two mode system formed by the two states  $|\downarrow\rangle = |1, 1\rangle$  and  $|\uparrow\rangle = |2, -1\rangle$ , the atoms are now in a coherent spin state as discussed in 2.4.

For the experiments in this work, two different optical dipole traps have been used. The one used for the experiments on the classical behavior of the system used a high numerical aperture of the focusing lens creating a tight focus with a waist of  $\sim 5 \mu\text{m}$  [31]. This trap provides high transversal trap frequencies up to the kHz regime combined with a longitudinal trap frequency of typically  $\sim 60 \text{ Hz}$ . In this work it will be referred to as the *charger* trap. The dipole trap used for the investigation of the quantum mechanical behavior of the system used a much lower aperture of the focusing lens providing low longitudinal trap frequencies as low as  $\sim 1 \text{ Hz}$  and transversal trap frequencies of only about 130 Hz. The high aspect ratio of this dipole trap motivates its name, *waveguide* trap. Absorption images of the cigar shaped clouds in the two traps are shown in figure 3.3.

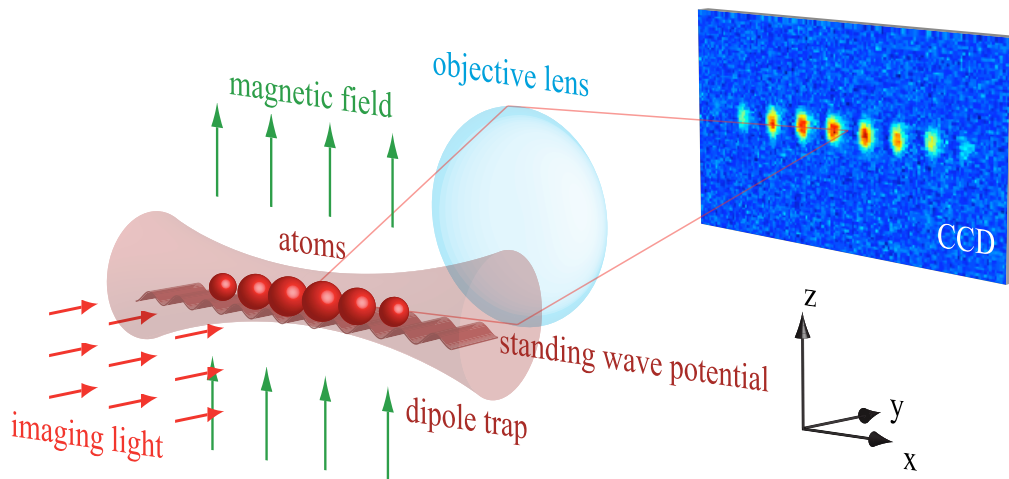


**Figure 3.2:** Schematic illustration of the experimental setup. The atoms are trapped in the focus of a red detuned laser beam traveling in  $x$  direction, i.e. the optical dipole trap. This trap is overlapped with a one dimensional lattice potential forming several potential wells where individual condensates are trapped along the axis of the optical dipole trap with a typical distance of  $\sim 5 \mu\text{m}$ . A magnetic field in the vertical  $z$ -direction (green) allows for the use of a Feshbach resonance. For imaging the clouds, the atoms are addressed by a resonant laser beam (light red) perpendicular to their extension along the dipole trap. The transmitted light is imaged onto a CCD (charge-coupled device) by a large numerical aperture imaging system, here shown schematically by a single lens.

### 3.3 Creating many Copies of the same State

To investigate the properties of the system it is necessary to create many copies of the same state. This can be done by repeating the experimental sequence many times with the same parameters. Another way is to create several independent

realizations in the same experimental sequence simultaneously. In our experiments this is done due to a necessity concerning the trap geometry and the advantage of gaining more information about the state in a single run.

The relation between waist and Rayleigh length of the Gaussian beam of the dipole trap leads to a cigar shaped condensate cloud. While the transversal trapping frequencies in our case are as high as several hundred Hz the longitudinal trapping frequencies in the dipole trap can be as low as only a few Hz. This causes the problem that the ground state wave functions of the two spin states can be very different due to the different scattering lengths of the species [32]. The assumption of constant external modes which is essential for our description does not hold in this situation. It is therefore important to increase the longitudinal trapping frequency so that the confinement in this direction is high enough that the dynamics in the external wave function can be neglected. This is done by a one-dimensional optical lattice potential along the longitudinal axis of the trap (schematically shown in figure 3.2). This potential is set up by two beams oriented with a relative angle of approximately eight degrees overlapping at the position of the dipole trap. The interference pattern created by these beams leads to a sinusoidal potential along the longitudinal direction of the dipole trap which creates several local potential minima in this direction. For high lattice intensities the cigar shaped condensate is divided up into several condensates which sit in the different potential wells. This is shown in the absorption images in figure 3.3.

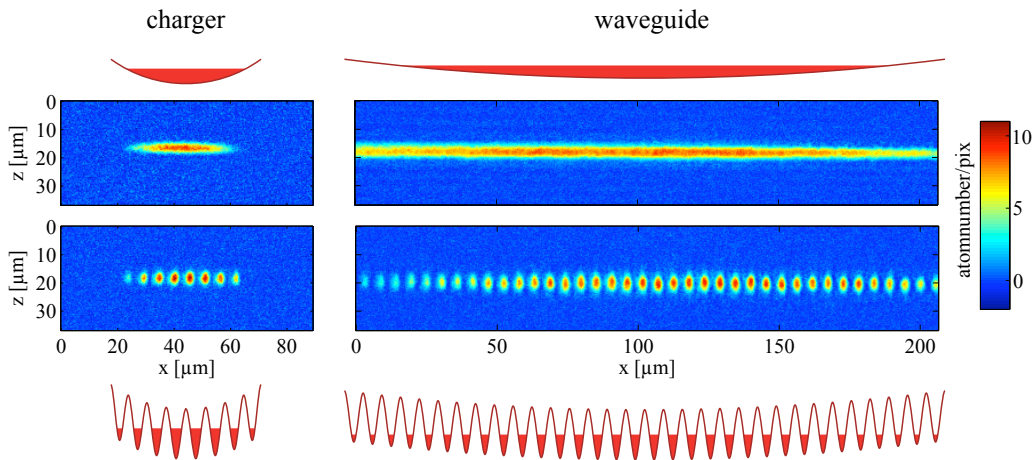


**Figure 3.3:** Typical absorption images of atom clouds in the charger and waveguide dipole traps (upper row left and right) and respective split clouds with the one dimensional lattice turned on (lower images). The red curves illustrate the optical potential filled by the chemical potential of the atoms along the  $x$ - direction. The total atom numbers on the images of the charger and the waveguide dipole trap are about 5000 and 40000 respectively, while the total atom number in the maximally filled wells in the second row of images is about 800.

These condensates can be treated individually when the time scale for tunneling between neighboring wells is much longer than the duration of an experiment, which is well fulfilled in our experiments. The two beams originate from the same

Titanium-sapphire laser. The tunable wavelength of this laser was tuned to 840 nm for the experiments in the smaller dipole trap and to 810 nm for the experiments which were performed in the long trap leading to a well spacing of 5.6  $\mu\text{m}$  and 5.1  $\mu\text{m}$  respectively. This setup allows for longitudinal trapping frequencies as high or higher than the transversal ones, which justifies the assumption of constant external modes as discussed in the next section.

The splitting of the initial condensate into several condensates has another nice side effect. The results obtained in the different condensates give a huge statistical boost since the number of results gained during one experimental run is, in principle, directly given by the number of condensates. In the tightly- focused charger dipole trap one gets six to eight condensates, however their atom number distribution is still strongly determined by the underlying dipole trap. This limits one to using only the two or four inner wells for the analysis, where the atom number is approximately the same. This is one reason why we set up the long waveguide dipole trap for the quantum state characterization where high statistics are needed. This trap allows to have up to  $\sim 40$  condensates on the absorption image. The use of all the realizations in parallel is of course only possible as long as variations in the experimental conditions for the different condensates are small or can be well controlled.

### 3.4 Coupling of the Two Spin States

The linear coupling between the two states of the Bose Einstein condensate is provided by a two photon magnetic dipole transition. The energy difference between the states of approximately 6.8 GHz is overcome by a microwave photon of roughly 6.8 GHz and a photon in the radio frequency range of approximately 6 MHz. The frequency of the microwave and RF photon are chosen such that the two states are resonantly coupled and the state  $|F, m_f\rangle = |2, 0\rangle$  acts as the intermediate state. The detuning from this state is chosen for all the experiments in this work as 200 kHz below the intermediate state. This detuning was optimized such that it gives a good compromise between two-photon Rabi frequency and single-photon transition probability to other spin states. The achieved Rabi frequencies on the two photon transition are limited technically by the microwave power which provides a maximum single photon Rabi frequency on the order of 20 kHz. To minimize the single photon transition probability during the two photon coupling the power of the radio frequency is chosen such that it has approximately the same resonant single photon Rabi frequency as the microwave. This leads to two photon Rabi frequencies up to 1 kHz.

In our situation, where the detuning of the two radiation fields from the intermediate state is high, the transition probability to the intermediate state can be neglected and the whole transition can be treated like a single photon transition.

Selection rules require a two photon transition for the coupling of the two spin states, which has the disadvantage of a reduced Rabi frequency, however, the use of the radio frequency photon has several technical advantages. The radio frequency field can be easily controlled in phase and amplitude by the use of an arbitrary waveform generator. It is therefore possible to make fast changes of the coupling

phase and amplitude. The coupling term in the Hamiltonian (equation 2.12) can therefore be written more generally as,

$$\Omega(t) \cdot \left[ (\cos \varphi_c(t) \hat{J}_x + \sin \varphi_c(t) \hat{J}_y) \right]$$

where the  $\varphi_c(t)$  is the time dependent phase of the coupling field. This high flexibility allows us to employ the pulse techniques developed in the field of nuclear magnetic resonance [33] to prepare and readout the state of the system which will be discussed in more detail in section 4.6 and 5.4.

### 3.5 Nonlinearity and Feshbach Resonance

The timescale of the dynamics in the resonant Hamiltonian is given by the strength of the parameters  $\chi$  and  $\Omega$  in the Hamiltonian of the system (see equation (2.12)). As discussed in 3.4 the Rabi frequency  $\Omega$  is mainly technically limited while the nonlinearity is limited by the scattering length and the wave function integral (see equations (2.5)(2.6)(2.13)). The problem with  $^{87}\text{Rb}$  is that the three important elastic scattering lengths are almost exactly the same at zero magnetic field [34] giving only a very small effective nonlinearity. However, the use of a Feshbach resonance allows us to change the scattering properties of ultra cold atomic systems. This method has proven to be an extremely valuable tool for many experiments with ultra cold atoms [7, 35].

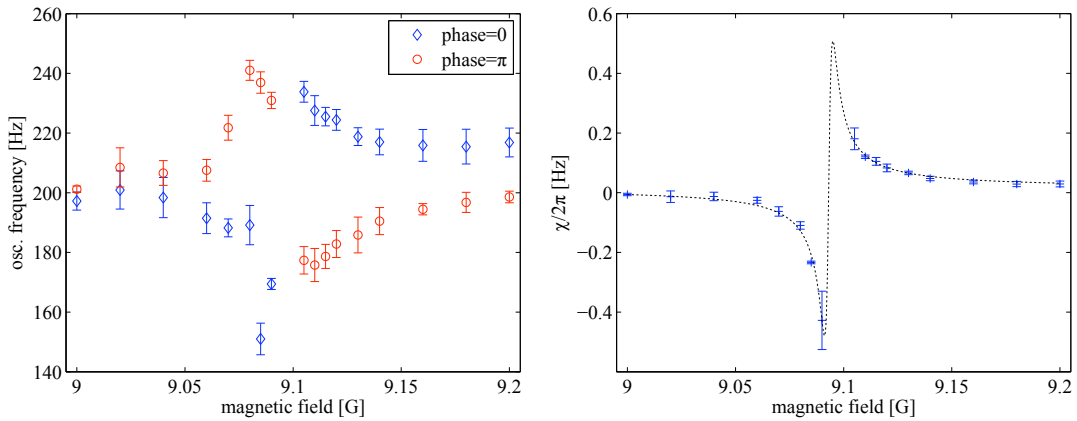


**Figure 3.4:** Measurement of the nonlinearity depending on the magnetic field close to the Feshbach resonance. (left) The magnetic field determines the scattering properties close to the Feshbach resonance. The resulting change of the nonlinearity  $\chi$  in the Hamiltonian leads to a change of the oscillation frequency of the dynamics on the two sides of the sphere (blue diamonds and red circles). (right) The nonlinear interaction  $\chi$  can be directly deduced from the measured oscillation frequencies. The typical dispersive shape associated with the lossy Feshbach resonance is here fitted (dotted line) under the assumption of constant wave functions over the whole range of magnetic fields). The measurement was performed with roughly 600 atoms in the charger trap configuration, with trap frequencies of  $\sim 420$  Hz in all directions.

In our case, we use a Feshbach resonance that modifies the inter-species scattering length of the atoms in the two spin states while the intra-species scattering is insignificantly changed [36, 37]. The resulting nonlinearity can be directly measured by using the theoretical predictions made within the classical mean field theory of the problem. The oscillation frequency on the two sides of the sphere are changed under the influence of the nonlinearity (see section 2.6). This change can be used to experimentally determine the resulting nonlinearity without further knowledge of the systems external mode. A more detailed discussion of these relations will be given in chapter 4.1. The results of such a measurement are shown in figure 3.4, where the left panel shows the change of the oscillation frequency on the two sides of the sphere and the right panel shows the resulting nonlinearity. From this measurement one might deduce that a magnetic field close to the Feshbach resonance would be favorable for a high nonlinearity but the proximity to the resonance also leads to dramatic loss of the atoms as discussed in section 3.8.1. In the experiment we have therefore chosen a magnetic field where a good trade off between loss and nonlinearity was found. The experiments in the charger were performed at 9.13 G with a typical nonlinearity of  $\chi \sim 2\pi \times 0.065$  Hz while the experiments on the quantum behavior of the system were done at 9.12 G resulting in an effective nonlinearity of  $\chi \sim 2\pi \times 0.09$  Hz.

As discussed in section 2.6 the ratio  $\Lambda = \frac{\chi N}{\Omega}$  plays an important role in the dynamical behavior of the system. As was already motivated at  $\Lambda = 1$  the dynamics are expected to be significantly changed. For typical atom numbers in the experiment and our given nonlinearity this corresponds to a linear coupling frequency on the order of tens of Hz. The overall time scale of the experiments is therefore given mainly by the size of the nonlinearity.

### 3.6 Time Dependence of the Spatial Wave Functions

The important simplification in the derivation of the theoretical description is based on the assumption of constant external modes. It has been shown that this assumption is typically fulfilled for small atom numbers and tight confinement in the trap. However as long as the interaction between the atoms is spin dependent, the constant spatial wave function is an approximation. While it is in general possible to treat the problem in terms of a time-dependent Gross-Pitaevskiĭ equation the numerical simulation gets very complex without further assumptions [38, 39].

To give a theoretical insight into the applicability of the constant mode approximation it is instructive to look at the ground state probability densities without coupling for different atom number partitions in the two modes. The ground state modes can be computed relatively simply by numerical methods treating the time-independent Gross-Pitaevskiĭ equation. The left panel in figure 3.5 shows the ground state distributions in the trapping scenario, which corresponds to the case of the elongated waveguide trap.

The narrow set of curves shows the distribution in the longitudinal direction where the high trapping frequency of the lattice potential of  $\sim 860$  Hz provides a strong confinement. The wide set of curves shows the distribution in the shallow

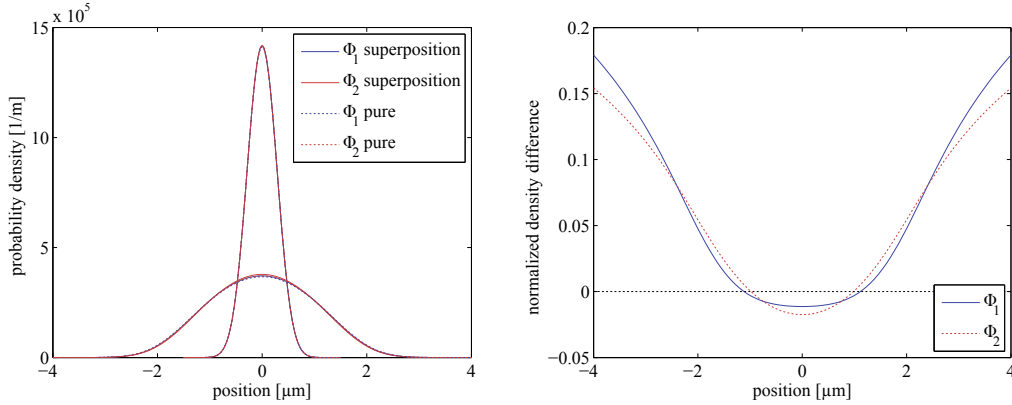


**Figure 3.5:** (left) Ground state probability densities without linear coupling for 400 atoms distributed equally over the two states (solid lines) and pure densities in either state of the states (dotted lines). The narrow set of curves are in the tight direction of the strongly confining lattice potential (860 Hz) while the wide set of curves shows the probability densities in the direction of the weak transversal confinement (130 Hz). The difference between the different partition of atoms is hardly visible here. (right) Relative probability density difference between the mixed and the pure ground state functions in the weak transversal direction for spin down (blue) and spin up (red dotted). In the relevant center the probability densities differ by less than 5% which confirms the usability of the constant spatial mode approximation.

transversal direction (trapping frequency  $\sim 130$  Hz). Shown are the ground state distributions for an equal partition of 400 atoms and the ground state distributions for a pure condensate of the same atom number in either of the two spin states. The intra species scattering length has been chosen to be 75 Bohr radii which is a lower estimate on the real value in our experiment. As is clearly visible, the external modes are indistinguishable for the longitudinal direction and similar in the transversal direction for all four cases. To give a more quantitative view on the actual difference the normalized wave function difference between the respective pure and 50/50 case is shown in the right panel of figure 3.5 for the transversal direction. In the region with a significant probability density the respective wave functions only differ by a few percent. The relatively high difference at the outer regions is not as important due to the low probability density.

The analysis of the ground state modes shows that even in the case of the unfavorable waveguide trap configuration, the modes do not change appreciably for different atom number partitions over the two spin states. This justifies the approximation of constant external modes in our experimental configuration.

### 3.7 Imaging

The observable in the system is the atom number in the individual spin states. The Bose-Einstein condensed atoms are a system that is only very weakly coupled to its environment. This is necessary to have the high level of coherence needed for the experiments but poses difficulties for the detection of the system's state. Several

detection methods have been implemented in ultra-cold atom physics experiments so far [40, 41, 42]. In our experiment, we use high-intensity absorption imaging to detect the atom number. The atoms are illuminated by a pulse of a resonant laser light, which is imaged onto a CCD camera by an objective with high numerical aperture lens, allowing us to spatially resolve adjacent atomic clouds [43]. The resonant light is scattered by the atoms and casts a shadow on the CCD depending on the column density of atoms in the cloud as is illustrated in figure 3.2. This negative image of the atom density can be calculated into an absolute atom number by taking a reference image of the light field under the same condition but without the atoms and appropriate calibration of atom number in relation to the measured absorption. The light absorption follows the Beer-Lambert law and several methods for the calibration of the parameters of the non linear dependence have been developed [40].

In our case a precise imaging calibration can also be performed by using the fact that the variance of a coherent spin state is well known from its binomial character (see section 2.4). In the following we will try to outline the very basic concept of this approach.

We assume that one has already linearized the dependence of the presumably incorrectly inferred atom number  $\tilde{N}_k$  of the two spin states to the real atom number  $N_k$  by other methods and that the linear dependence is the same for the two spins. This can be expressed by

$$\tilde{N}_i = \alpha N_1 \quad \text{and} \quad \tilde{N}_2 = \alpha N_2.$$

For the variance of the inferred atom number difference one finds therefore

$$\text{Var}(\tilde{N}_2 - \tilde{N}_1) = \alpha^2 \text{Var}(N_2 - N_1) \propto \alpha^2 \langle (N_1 + N_2) \rangle = \alpha \langle (\tilde{N}_1 + \tilde{N}_2) \rangle.$$

Here the proportionality relation stems from the distribution of the CSS and is known, while the last equation originates from the assumption. Since the same proportionality relation between atom number fluctuations and total atom number applies for the inferred atom numbers the parameter  $\alpha$  can be fixed by measuring both atom number fluctuations and total atom number for a CSS.

One may argue that the method has difficulties when fluctuations in the inferred atom numbers stem from other sources than the atoms. However this problem can be overcome as long as the additional variances do not grow linearly with the total atom number which is typically the case. A more detailed discussion of our imaging calibration can also be found in [28].

To selectively count the atoms in the different spin states we either use state selective light or spatial separation of the spin states. For the first method the atoms in the two spin states are counted by taking two images where the first one only images the atoms in the  $F = 2$  hyperfine manifold and successive imaging of the atoms in the  $F = 1$  states by additional light on the repumping transition. The second method transfers the atoms in the  $|F, m_F\rangle = |2, -1\rangle$  by a microwave pulse to the  $|1, -1\rangle$  state. This state has the opposite magnetic moment as the  $|1, +1\rangle$  state which enables Stern-Gerlach separation of the two spin states in the vertical direction so that they can be imaged individually on the same absorption image.

### 3.7.1 Imaging Noise

The absorption imaging technique used in the experiments suffers from several drawbacks which are due to the additional fluctuations briefly mentioned above. There are two main sources for this noise in the imaging process. The first one originates from the granularity of the light pulses. The finite number of photons in the pulses leads to shot noise which translates into intensity fluctuations on the images becoming noticeable as an effective noise on the determined atom number. This noise contribution is typically on the order of 8 atoms in our system. Although the reason for the second contribution of noise is not completely resolved it can be mainly backtracked to differences of the image with atoms and the reference image without atoms. Between the two images lies a time of approximately 1 ms. In this time slight changes in the light path change the intensity pattern so that the absorbed intensity can not be measured perfectly which shows up in a slight fringe pattern on the calculated images. The noise level of this fringe noise corresponds to an effective atom noise comparable to the noise stemming from photon shotnoise. The overall atom number detection noise is therefore approximately 11 atoms.

## 3.8 Experimental Imperfections

Although ultra-cold neutral atomic systems have proven to be very close to ideal quantum mechanical testbeds they are still subject to decoherence with their environment. Furthermore, technical imperfectly controlled system parameters lead to difficulties in implementing the desired Hamiltonian, and thus give rise to additional noise in the experimental results.

In this section an overview of the main technical and physical limitations in implementing the quantum mechanical system is given.

### 3.8.1 Atom Loss

The Bose-Einstein condensed clouds in the traps are subject to atom loss. The two main contributions to atom loss in our system are spin relaxation and three body collisions close to the Feshbach resonance.

Spin relaxation may occur when two atoms collide. While the total spin magnetization of the atoms is conserved the hyperfine spin is not necessarily a conserved quantity in the process. The typical energy scale of the atoms in the cloud is much lower than the hyperfine splitting of  $^{87}\text{Rb}$  which energetically forbids the excitation of  $F = 1$  atoms into the  $F = 2$  manifold, but the relaxation in the other direction is possible. The energy released in this process leads to  $F = 2$  atom loss. The timescale of this loss is on the order of 200 ms in our experiment.

The second loss mechanism is due to the Feshbach resonance. The Feshbach resonance is the resonant coupling of two free atoms to a molecular state. The binding energy of this molecular state can be transferred to kinetic energy of a third atom. In this case all three atoms gain enough energy to be lost from the trap. The time scale of this loss process depends strongly on the distance to the Feshbach resonance. In the experiments discussed here it was typically on the order of 100 ms.

For the sake of completeness, as in all cold atom experiments atoms can be also lost due to collisions with the background gas in the vacuum chamber or released from the trap due to heating. The loss time scale of this process is typically much longer than 10 s making it insignificant in relation to the other loss processes.

With the overall time scale of the loss of about 100 ms the absolute loss of atoms during the typical experimental evolution time of 40 ms is significant. This loss has mainly two effects: decoherence of the system's state and the change of the system parameters.

The effect of decoherence is especially important for quantum states that are entangled since the entanglement is typically lost under the influence of decohering processes. The squeezed spin states and macroscopic superposition states investigated in chapter 5 are examples of entangled states in the system. In general theoretical predictions for the influence of decoherence such as atom loss on such states are complicated and usually demand assumptions that are experimentally hard to ensure.

Although the influence of loss on squeezing has been theoretically investigated [44] and the macroscopic superpositions states have been found to be relatively robust under the influence of loss [45, 15] the theoretical predictions do not necessarily cover the experimental situation completely. It is therefore an open question how the produced entangled states decohere due to atom loss.

The influence on the system parameters will be discussed in more detail in section 5.5.2

### 3.8.2 Magnetic Field Noise

The energies of the two modes of our system which correspond to  $\omega_1$  and  $\omega_2$  in equation 2.14 are magnetic field dependent due to the Zeeman effect. However the linear Zeeman effect shifts both levels the same way so that the important energy difference is not affected by the linear Zeeman effect (see figure 3.1). However, the quadratic Zeeman effect shifts the two levels relative to each other. At magnetic field strengths of approximately 9G where the experiments are performed this shift is approximately 10.6Hz/mG and directly enters in the detuning term of the Hamiltonian (see equation 2.14). The magnetic field fluctuations in the lab are typically on the order of several mG at a frequency of 50 Hz due to the power lines and slow drifts from day to day. The resulting fluctuations of the detuning have to be compared to the Rabi frequencies of the linear coupling to give an impression on its influence on the dynamics. The linear coupling during the time evolution is typically on the order of less than 30 Hz which makes the detuning term at least comparable to the others or even the dominant term in the Hamiltonian. A major technical issue is therefore the reduction of the magnetic field fluctuations such that the detuning term in the Hamiltonian becomes well-controlled. This has been accomplished by an active magnetic field stabilization system discussed in the next section.

### 3.8.3 Magnetic Field Stabilisation

Magnetic field stabilization in the experiment can be either implemented by using passive methods such as  $\mu$ -metal shielding or by active stabilization through closed

loop field control [46]. Although the first generally promises better results, it is difficult to implement in our experimental setup because of two reasons. The passive shield shields not only the magnetic fields from the atoms but also significantly reduces the optical access to them which is a significant disadvantage in an ultra cold atom experiment. The second reason is the high magnetic fields generated during the magnetic trapping of the atoms. These fields would magnetize the passive shield leading to a strong reduction of performance. For these reasons an active magnetic field stabilization has been set up.

The active stabilization of the magnetic field in the experiment is done by using a pair of large square coils for producing the relatively high magnetic field of  $\sim 9$  G needed for the Feshbach resonance. These coils have a size of  $\sim 1\text{m}^2$  and are set up in approximate Helmholtz configuration with the atomic cloud roughly in their center. The use of this large coils ensures a uniform field in a region around the atoms, which enables us to get an accurate field measurement using a fluxgate magnetometer (Bartington Mag03MS) at a distance of about 8 cm from the atoms. The magnetometer signal is used in a closed feedback control driving a second set of coils to actively stabilize the magnetic field at the position of the sensor and therefore also at the position of the atoms.

With this setup we are able to reduce the magnetic field fluctuations at 50Hz down to a level of  $200\mu\text{G}$  in amplitude. These field fluctuations due to the power lines are very stable in phase and amplitude. We therefore synchronize our experiment to the 50 Hz line frequency to further lower their effect. The residual fluctuations from realization to realization are below  $40\mu\text{G}$  corresponding to fluctuations of the effective detuning of about 0.4 Hz.

On a long time scale the effective magnetic field at the position of the atoms still drifts over some mG from day to day. These drifts are not completely understood but can be partly explained by the temperature dependence of the magnetic field sensor. We overcome these drifts by performing magnetic field reference measurements with the atoms on a regular basis.

#### 3.8.4 Magnetic Field Gradients

As discussed in 3.8.2 magnetic field changes result in a change of the detuning of the atomic transition relative to the linear coupling. A gradient of the magnetic field within the spatial extent of the individual condensates, which is typically on the order of some micrometers, is usually too small to introduce problems. On the length scale of the whole system with its extension in  $x$  direction over several hundred micrometers, even a rather small gradient may lead to a different detuning for the individual condensates. The influence of such a gradient on the system can be easily tested by performing a Ramsey sequence [47]. Such a sequence translates the accumulated phase resulting from the detuning into a population imbalance of the condensate which can be directly detected. This population imbalance is given by the sine of the accumulated phase. A constant gradient of the magnetic field along the line of condensates therefore shows up as a sinusoidal imbalance distribution from left to right. In the experiment the magnetic field of approximately 9 G is oriented along the vertical  $z$ -direction. The field components perpendicular to this field are much smaller, which makes the influence of their gradients negligible. The

only gradient important for our experiments is therefore that of the field components in  $z$ -direction increasing or decreasing in  $x$ -direction. To use all the condensates as individual realizations of the same system one has to reduce the gradient. This has been done by installing small permanent magnets with their dipole oriented along the  $z$ -direction on both sides of the condensed atoms anti parallel to each other. We choose permanent magnets to compensate the gradient instead of coils since they offer a high stability without active stabilization on long time scales. By adjusting the distance the gradient could be minimized to less than 2 mG/cm which corresponds to a maximal magnetic field difference of less than 40  $\mu$ G on the extension of the images. This is less than the overall shot-to-shot fluctuations in the experiment.

### 3.8.5 Rabi Frequency Gradients

The microwave and radio frequency antennas generating the oscillating linear coupling fields are positioned approximately 4 cm away from the condensed  $^{87}\text{Rb}$  atoms. The complex setup of coils and other metallic material in close proximity to the atoms leads to very complex field distribution. Although the length scale for the spread of the condensates in the  $x$ -direction is only on the order of several hundred  $\mu\text{m}$  while the wavelength of both the microwave and the radio frequency field is orders of magnitude larger we find an inhomogeneous power distribution over the condensates. This leads to different Rabi frequencies along the line of condensates which can be directly measured.

Individual measurement of the radio frequency and microwave Rabi frequencies allows us to find the source of this gradient. Surprisingly it is mainly due to a gradient in the radio frequency field. This gradient can not easily be altered since it is mainly given by the geometry of the antennas and the metallic parts close to the vacuum chamber, which leaves little room for alterations. With a maximal difference between left and right side of our images of approximately 3% it is not too critical but one has to consider potential effects in the data analysis. The influence of this gradient on the experiments in the tightly confining charger dipole trap can be completely neglected due to its small spatial extent.

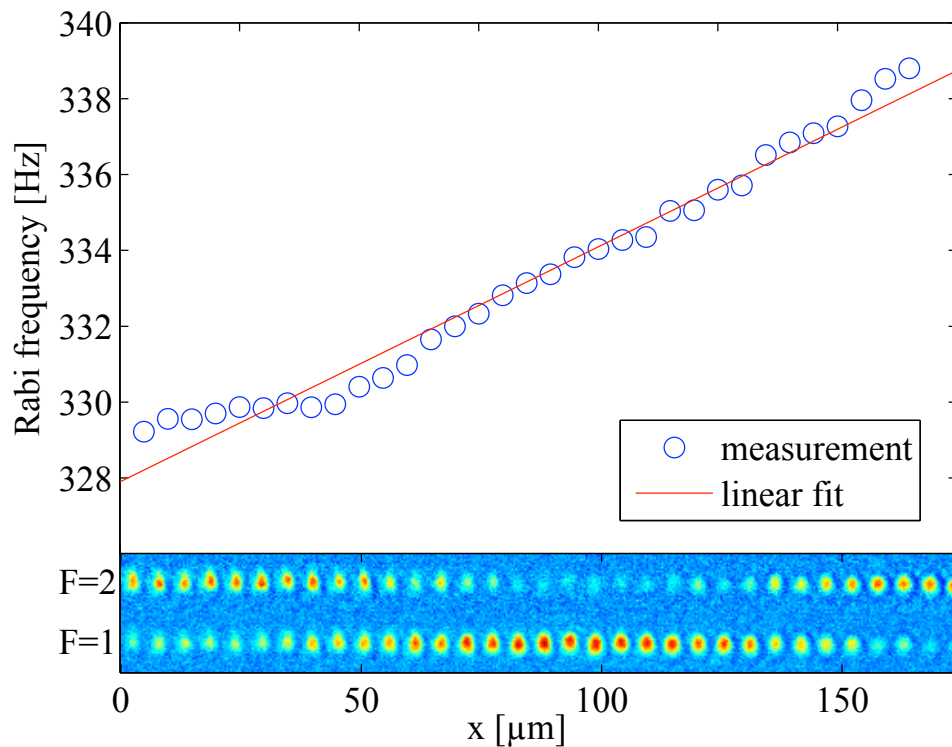


**Figure 3.6:** Measurement of the linear coupling Rabi frequency in the different wells over the extension of the image. As can be clearly seen the effective two photon Rabi frequency shows an approximately linear increase in  $x$ -direction of about 3% over the extension of the image of the clouds of about  $180\mu\text{m}$ . The resulting sinusoidal atom number distribution in the upper and lower spin states after a long Rabi pulse of  $\sim 130$  ms can be seen in the lower part. The antennas for the microwave and radio frequency radiation are situated right of the image in positive  $x$ -direction.

# Chapter 4

## Classical Bifurcation at the Transition from Rabi to Josephson Dynamics

In this section we discuss the investigation of the classical mean field dynamics of the Hamiltonian. The classical description is motivated by the fact that the quantum mechanical state of the system is macroscopic enough that it can be well described by the mean values of its observables. The resulting description is very similar to the Josephson effect found in superconductors [48, 49, 50] and the weakly linked reservoirs of super fluid Helium [51, 52]. A unique feature of the bosonic Josephson junction is the topological change of the classical phase space under a smooth parameter change. Such a scenario is described by a bifurcation in the dynamics which becomes accessible in the internal Josephson junction realized in this work [53]. The system allows to map out the full phase space of the dynamics and investigate the topological change.

### 4.1 The Classical Mean Field Hamiltonian

The system which is initially prepared in a coherent spin state behaves more and more classical with growing total number of particles. This becomes obvious in the Husimi distribution of the CSS, which becomes more and more localized with growing number of atoms (see figure 4.1). This supports the idea that for a large atom number the system can be characterized as a single point on the sphere and the dynamics can be described by classical equations of motion.

The expectation values in the three orthogonal directions for a CSS  $|N, \vartheta, \varphi\rangle$  are given by

$$\langle \hat{J}_x \rangle = \frac{N}{2} \sin \vartheta \cos \varphi, \quad \langle \hat{J}_y \rangle = \frac{N}{2} \sin \vartheta \sin \varphi, \quad \langle \hat{J}_z \rangle = \frac{N}{2} \cos \vartheta.$$

This shows that the CSS is completely defined by these expectation values and motivates the idea that the classical limit of these observables can be used as the phase space variables of the classical problem. However, the three variables are over defining the state of the system. The state is fully characterized by taking the following variables

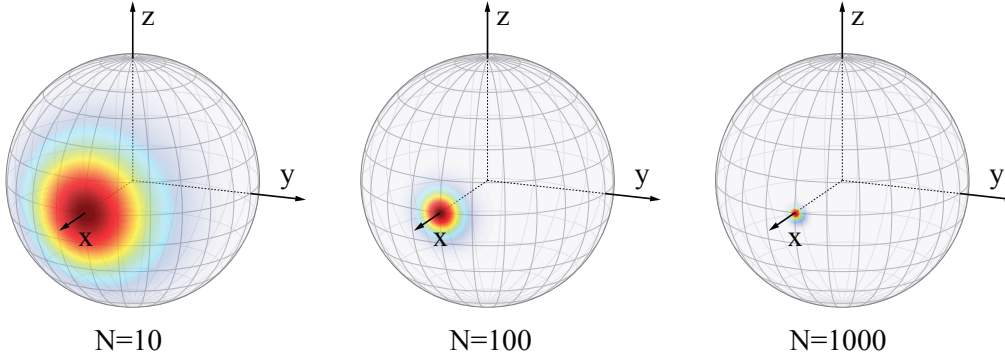


**Figure 4.1:** Husimi representation of coherent spin states with total atom numbers of 10, 100 and 1000 atoms from left to right. It is clearly visible how the quantum fluctuations shrink with the growing number of atoms. For high atom numbers it is therefore self evident that a classical description as a single point in the phase space is a very good approximation to the full quantum mechanical picture.

$$z = \frac{2}{N} \langle \hat{J}_z \rangle = \frac{N_2 - N_1}{N_2 + N_1} \quad (4.1)$$

$$\varphi = \arctan \left( \frac{\langle \hat{J}_y \rangle}{\langle \hat{J}_x \rangle} \right) \quad (4.2)$$

These variables correspond to the normalized atom number imbalance and the relative phase of the two modes.

Replacing the operators in the quantum Hamiltonian (see equation 2.12) by their mean values directly leads to the classical mean field Hamiltonian. Without the detuning term one gets

$$H_{MF} = \frac{\Lambda}{2} z^2 - \sqrt{1 - z^2} \cos \varphi, \quad (4.3)$$

with the corresponding equations of motion

$$\dot{z}(t) = -\sqrt{1 - z(t)^2} \sin \varphi(t), \quad (4.4)$$

$$\dot{\varphi}(t) = \Lambda z(t) + \frac{z(t)}{\sqrt{1 - z(t)^2}} \cos \varphi(t). \quad (4.5)$$

The influence of the detuning on the classical dynamics will be considered in section 4.4. This Hamiltonian can be solved analytically in terms of Jacobian elliptic functions [13] or integrated numerically.

## 4.2 Topologies of the Mean Field Hamiltonian

As already seen in section 2.6 the analysis of the fixed points of the system can be very instructive for the understanding of the resulting dynamics. The fixed points found in the approximate considerations in section 2.6 are exact for the classical

case. There are two fixed points on the equator  $F_0 = (z, \varphi) = (0, 0)$  and  $F_\pi = (0, \pi)$ , while for  $\Lambda > 1$  two additional fixed points  $F_\pm = (\pm\sqrt{1 - (1/\Lambda^2)}, \pi)$  appear. The appearance or disappearance of fixed points is associated with a bifurcation in the classical dynamics. Such a bifurcation is accompanied by a topological change of the phase space.

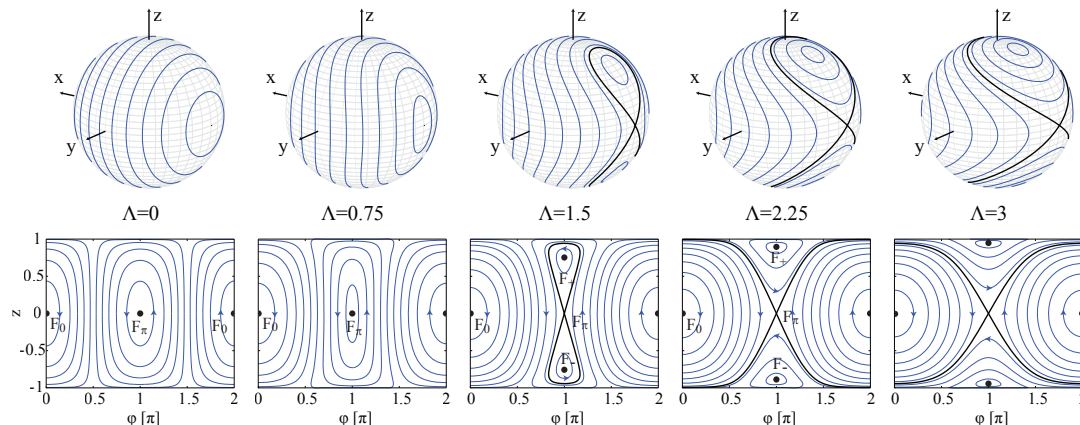


**Figure 4.2:** Illustrations of the phase plane portrait of the classical Hamiltonian for growing parameter  $\Lambda$  from left to right. The upper part shows the phase space on the sphere from a viewpoint behind the sphere. Here the topological change of the phase space and the emergence of the separatrix (black line) is clearly seen. The lower part shows the same phase portrait projected onto the plane. In this illustration the stable fixed points are marked by black dots and the direction of the dynamics is indicated by arrows.

This can be clearly seen in figure 4.2. Typical phase space trajectories are shown both on the sphere in the upper row of pictures and in a flat projection of the phase space in the bottom row for different values of  $\Lambda$ . The flat projection has the advantage that the phase space can be shown as a whole but one has to keep in mind that in this visualization the top and bottom line correspond to a single point in the phase space (north and south pole).

For small  $\Lambda$  the dynamics are dominated by the linear Rabi coupling, i.e. a rotation around the  $x$ -axis of the sphere. This regime is therefore referred to as the Rabi regime of the dynamics [9]. In the phase space the trajectories go around the two fixed points  $F_0$  and  $F_\pi$ . The circular shape of the trajectories corresponds to an oscillating behavior in both the relative imbalance  $z$  and the phase  $\varphi$ . The oscillations around  $F_0$  are called plasma oscillations in reference to their superconducting analog, while the oscillations around  $F_\pi$  which have mean phase  $\pi$  are called  $\pi$ -oscillations lacking a counterpart in the superconducting Josephson junctions. With increasing  $\Lambda$ , which corresponds to a relative increase of the nonlinearity, the dynamics on the two sides of the sphere become considerably different which can be seen in their deformation from pure circles.

For  $\Lambda > 1$  the effective strength of the nonlinearity is comparable to the linear coupling and the two fixed points  $F_+$  and  $F_-$  appear. Now the dynamics in their proximity enclose these fixed points. Although the fixed point  $F_\pi$  is unstable there

are still trajectories which revolve around it. While the dynamics around  $F_0$  are topologically unaffected by the increase of  $\Lambda$  the  $\pi$ -oscillations on the other side of the sphere can now be classified in those with zero mean imbalance and those with a mean imbalance either positive or negative. This finite mean imbalance originates from the interaction of the atoms among themselves. The dynamical behavior is therefore referred to as macroscopic quantum self trapping [13, 9]. An eight shaped separatrix (black line) divides the phase space into the topologically different regions.

By increasing  $\Lambda$  further the two fixed points  $F_{\pm}$  move further apart in the direction of the poles while the separatrix encloses more and more of the phase space. At  $\Lambda = 2$  the separatrix reaches the north and south pole. For even larger  $\Lambda$  the poles are enclosed by the separatrix and some self trapped trajectories revolve around the pole axis. Their dynamics are therefore characterized by a running behavior of the phase without bound. The regime of  $\Lambda > 1$  is called Josephson regime, since the phenomena of plasma oscillations and the macroscopic self trapping behavior can be found similarly in the Josephson effect known from weakly linked superconductors [9].

For the sake of completeness we mention that for very large  $\Lambda > N$  where  $N$  is the total atom number a third regime can be defined which is often referred to as Fock regime [9]. In this regime the coupling is so small that the ground state of the Hamiltonian becomes a highly entangled number state. Although this regime can be easily entered in our experiment by switching of the coupling radiation the interesting ground state properties can not be accessed on a time scale feasible in our experiment.

### 4.3 A Classical Analog

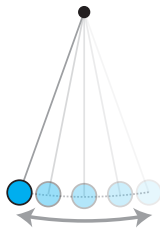


**Figure 4.3:** Pendulum performing plasma oscillations

The use of a classical Hamiltonian to describe the system has not only the advantage of simplification but also allows to compare the dynamics with other well known classical systems. As has been pointed out the classical Hamiltonian is very similar to that of a mathematical pendulum [13]. The Hamiltonian of a mathematical pendulum can be written as

$$H_{\text{Pendulum}} = \frac{\Lambda}{2} z^2 - \cos \varphi \quad (4.6)$$

Here  $z$  is the angular momentum variable of the pendulum and  $\varphi$  is the angular displacement. The first part of the Hamiltonian is the kinetic energy while the second

one corresponds to its potential energy. The mass, length and the gravitational constant of the pendulum are absorbed into  $\Lambda$  by an appropriately chosen time scale.

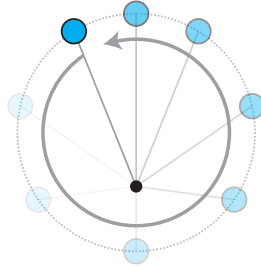


**Figure 4.4:** Macroscopic quantum self trapped pendulum

The comparison between the Hamiltonian of the pendulum and the classical Hamiltonian of our system (see equation 4.3) shows that the only difference is the additional factor  $\sqrt{1 - z^2}$  in the latter one. If one interprets this Hamiltonian also as a pendulum this factor leads to a momentum dependent shortening of the pendulum. However for small  $|z|$  this term is close to one and we expect a very similar behavior of the two systems. For large  $\Lambda$  this condition is satisfied for a large region of the phase space.

Considering a classical pendulum one finds two different types of motion: oscillations around the minimum and rotations around the pivot of the pendulum. These two types of motion have a direct analog in our system. The oscillations around the minimum correspond to the plasma oscillations. Both the angular momentum and the phase of the pendulum oscillate around the fixed point which corresponds to  $F_0$ . This is illustrated in figure 4.3. The full rotations around the pivot correspond to the macroscopic self trapped trajectories with running phase. The latter ones have a finite positive or negative mean angular momentum corresponding to a rotation either clockwise or counter clockwise (see figure 4.4). The shortening of the pendulum can be small as long as  $\Lambda$  is very large. The unstable fixed point  $F_\pi$  corresponds to a situation where the pendulum is perfectly pointing upward.

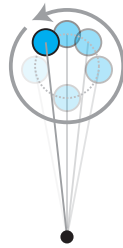


**Figure 4.5:** Self-trapped  $\pi$ -oscillations

Since the mathematical pendulum has only two fixed points the two stable fixed points  $F_\pm$  of the system have to have their origin in the shortening of the pendulum.

If the angular momentum of the pendulum is high enough the shortening can lead to a motion where the pendulum bob does not revolve around the pivot any more but orbits around a point above the pivot. The mean angular displacement is therefore found to be  $\pi$  while there is still some finite positive or negative mean angular momentum. This behavior is shown in figure 4.5 and corresponds to the macroscopic self trapping with mean phase  $\pi$ .

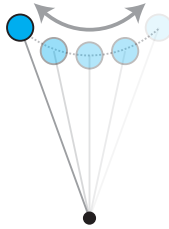


**Figure 4.6:**  $\pi$ -oscillations around the stable upper fixed point.

For small  $\Lambda$   $F_\pi$  is a stable fixed point which also originates from the shortening of the pendulum. This shortening is found in the potential energy part of the Hamiltonian and has a local minimum even for a phase  $\varphi \approx \pi$ . It therefore stabilizes the pendulum in its upward position. This behavior is illustrated in figure 4.6. The oscillation back and forth leads to a zero mean of the momentum.

### Topological Considerations

As was shown above the two systems behave very similar in the case of large  $\Lambda$  and small values of the momentum  $z$  but there is also a major difference where these conditions are not fulfilled. This is especially apparent by comparing the topologies of the two phase spaces. While the momentum of the normal pendulum is not bounded at all the momentum shortened pendulum only allows a maximum momentum of  $\pm 1$ . In this situation the length of the pendulum shrinks to zero and the angular displacement  $\varphi$  gets undefined. This is just another way of understanding the spherical nature of its phase space. For the normal pendulum this can never happen, the topology of the phase space is cylindrical as is illustrated in figure 4.7.

From this illustration it becomes also obvious why the behavior is so similar for small  $|z|$  in the region around the equator, the sphere can be well approximated by a cylinder.

The comparison of the momentum shortened pendulum with the rigid mathematical pendulum corresponds directly to the comparison of Josephson physics found in superconductors and the bosonic Josephson junction. This illustrates that the analogy of the two phenomena breaks down when one leaves the cylindrical part of the phase space in the direction of the poles of the sphere.

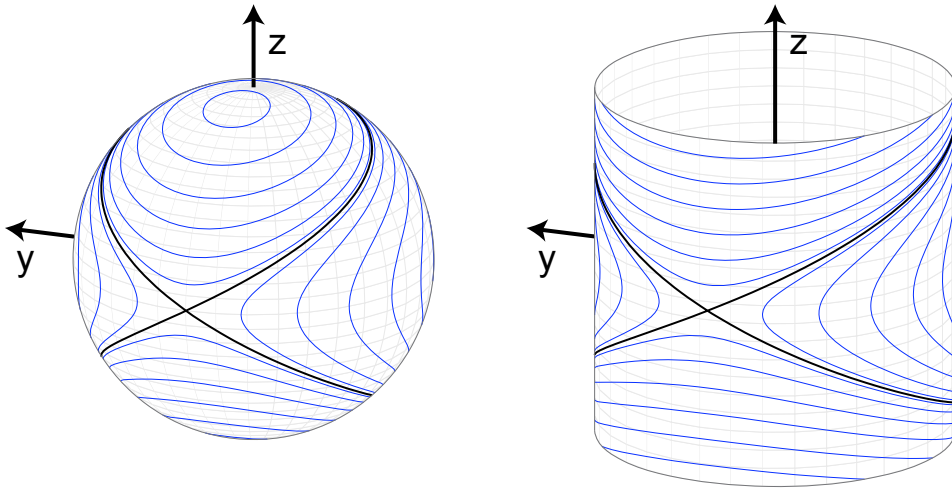


**Figure 4.7:** Topological difference between bosonic Josephsen junctions and their superconducting analogs. Phase spaces of the momentum shortened pendulum left and of the mathematical pendulum on the right for the same parameter  $\Lambda > 2$ . The topological difference of the spherical phase space of the momentum shortened pendulum and the cylindrical phase space of the mathematical rigid pendulum illustrates the absence of the dynamics with mean phase  $\pi$  in the case of the mathematical pendulum.

## 4.4 Influence of the Detuning on the Classical Dynamics

Up to now the detuning term in the quantum Hamiltonian has been left out in the discussion of the classical mean field dynamics of the system. Although the experiments discussed in this work aspire zero detuning one is limited by experimental imperfections as discussed in section 3.8. In this section we will therefore treat the influence of a finite detuning on the classical behavior. The detuning term in the quantum Hamiltonian  $\Delta \hat{J}_z$  translates into  $\frac{\Delta}{\Omega} z$  in the classical mean field Hamiltonian. In the spirit of the discussion in section 2.6 this term corresponds to a rotation on the sphere around the  $z$ -direction. This leads to a break of the symmetry of the northern and southern hemisphere of the phase space. While the phase of the fixed points turns out to be unaffected at either zero or  $\pi$  their longitude or imbalance  $z$  is changed. For large detuning this can even lead to a complete topological change of the phase space meaning that even for  $\Lambda > 1$  the fixed point  $F_\pi$  is not unstable and the two fixed points  $F_\pm$  do not exist. This is illustrated in figure 4.8 in the left panel where the number of fixed points is given depending on the parameters  $\Lambda$  and  $\Delta/\Omega$ . It can be clearly seen that the detuning leads to an increase of the critical  $\Lambda$  where the bifurcation happens. The typical imperfection in  $\Delta/\Omega$  in the experiment

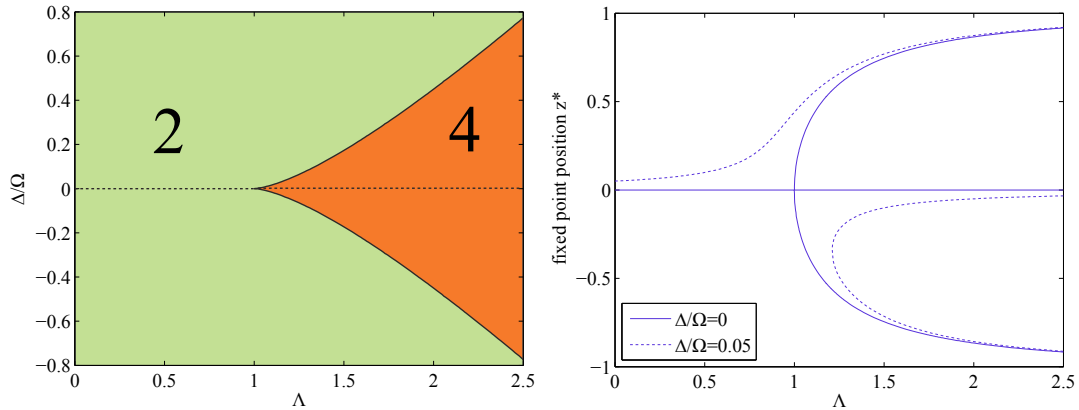


**Figure 4.8:** (left) Dependence of the number of fixed points on  $\Lambda$  and the effective detuning  $\Delta/\Omega$ . The onset of the orange region with 4 fixed points marks the bifurcation point. (right) Position of the fixed points for zero detuning (solid lines) and a finite effective detuning of  $\Delta/\Omega=0.05$  (dotted line). In the second case the bifurcation happens *out of blue sky* and for a larger critical  $\Lambda$ .

is less than 0.03 so that the change of the critical  $\Lambda$  can be considered negligible.

In the right panel of figure 4.8 the position of the fixed points on the  $\pi$ -side of the sphere is shown depending on the parameter  $\Lambda$  for zero detuning (solid line) and a finite detuning (dashed line). As can be seen in the case of finite detuning the assignment of the fixed points is not any more clear. Here the stable fixed point does not undergo a transition into an unstable fixed point any more. Instead the unstable fixed point appears together with a stable fixed point *out of blue sky*.

## 4.5 External vs. Internal Bosonic Josephson Junctions

The first realizations of bosonic Josephson junctions with ultra cold atoms have been implemented by using external degrees of freedom to realize the two mode system [54, 55, 56]. In this work we have implemented the system by taking solely the spin of the atoms as discriminating property of the two modes. These two ways offer different advantages and disadvantages which will be discussed in the following.

External degrees of freedom allow one to optically distinguish between the two states. By designing optical potentials which separate the two BEC by a large amount one can further easily reach quite large nonlinearities even if the scattering lengths are not favorable. However the coupling frequency is typically reduced because the mode overlap decreases (see (2.7)). This allows one to access regimes where the nonlinearity dominates the dynamics, i.e. large  $\Lambda$ . On the other hand the regime of small  $\Lambda$  is hard to reach. The aspired high linear coupling corresponds to a high mode overlap which typically leads to a breakdown of the two mode theory. The smallest  $\Lambda$  which was reachable in the work of Albiez et al. was on the order of 70 [55] and therefore far above the bifurcation point.

The biggest drawback of external systems is that it is usually hard to prepare

an arbitrary initial coherent spin state. To get a well defined phase between the two condensates they have to either originate from the same condensate or they have to be at least strongly coupled for some time [57]. After the following separation one has to employ energy shifts to the condensates so that a specific desired phase difference between them builds up which is technically challenging. Another disadvantage of such systems is that the readout of the phase is typically done via spatial interference of the two condensates which raises the technical difficulty of detecting the interference pattern with high resolution.

The use of the internal spin degree of freedom allows one to circumvent most of these issues. By optically trapping the two condensates in the same trap one gets close to perfect mode overlap leaving the spin as the only distinguishing parameter of the two subsystems. The coupling of the internal degrees of freedom can be achieved by using electromagnetic fields either by using optical two photon stimulated Raman transitions or by employing microwave and radio-frequency magnetic fields directly coupling to the magnetic moment of the atoms. For both methods commercial radio frequency or microwave sources allow one to couple the two states with a very high level of control. The possibility to switch the phase and amplitude of the coupling field on a nanosecond time scale allows to implement almost arbitrary unitary transformations on the Bloch sphere, which help to readout and characterize the state. The drawback of the internal Josephson junction, at least in the case of  $^{87}\text{Rb}$ , is that the nonlinearities are small compared to the external case and accompanied by significant atom loss. Nevertheless internal degrees of freedom allow for the investigation of the regime of  $\Lambda$  at the transition from Rabi to Josephson dynamics where the bifurcation occurs.

## 4.6 Experimental Sequence and State Readout

In this section we want to briefly discuss how the measurements on the classical mean field dynamics are performed.

In general the variation of  $\Lambda$  is experimentally performed by varying the coupling strength  $\Omega$ . This means that the nonlinearity is kept constant over the actual measurement by ramping the magnetic field to the constant value of 9.13 G close above the Feshbach resonance where a good trade-off between atom loss and nonlinearity is found (see section 3.5).

The preparation and the phase readout of the state of the system is done with a maximum coupling strength of about  $2\pi \times 600$  Hz which corresponds to a minimal  $\Lambda < 0.05$ . This means that the influence of the nonlinearity during these pulses can be neglected in good approximation. The experimental sequence starts by such a pulse where the pulse length determines the initial imbalance. The following evolution happens with the appropriate attenuation of  $\Omega$  leading to the aspired  $\Lambda$ . The coupling during the evolution can have a relative phase difference to the preparation pulse which determines the initial phase of the dynamics. Since the state readout is performed via destructive absorption imaging the process has to be repeated frequently with varying length of the evolution time to obtain the dynamical behavior of the system in a stroboscopic way.

The readout of the population imbalance  $z$  can be performed by simply counting

the atom numbers in the different internal spin on the absorption images as discussed in section 3.7. To read out the phase  $\varphi$  we apply another strong coupling pulse to the atoms which performs a rotation of  $90^\circ$ . This pulse can be chosen in its relative phase to the evolution pulse so that it rotates either the  $x$  or the  $y$  coordinate into the  $z$  direction which can be measured as a relative atom number difference. In this way one obtains a full set of coordinates which can be used to get the variables  $z$  and  $\varphi$  in an unambiguous way.

## 4.7 Observation of the Topological Change

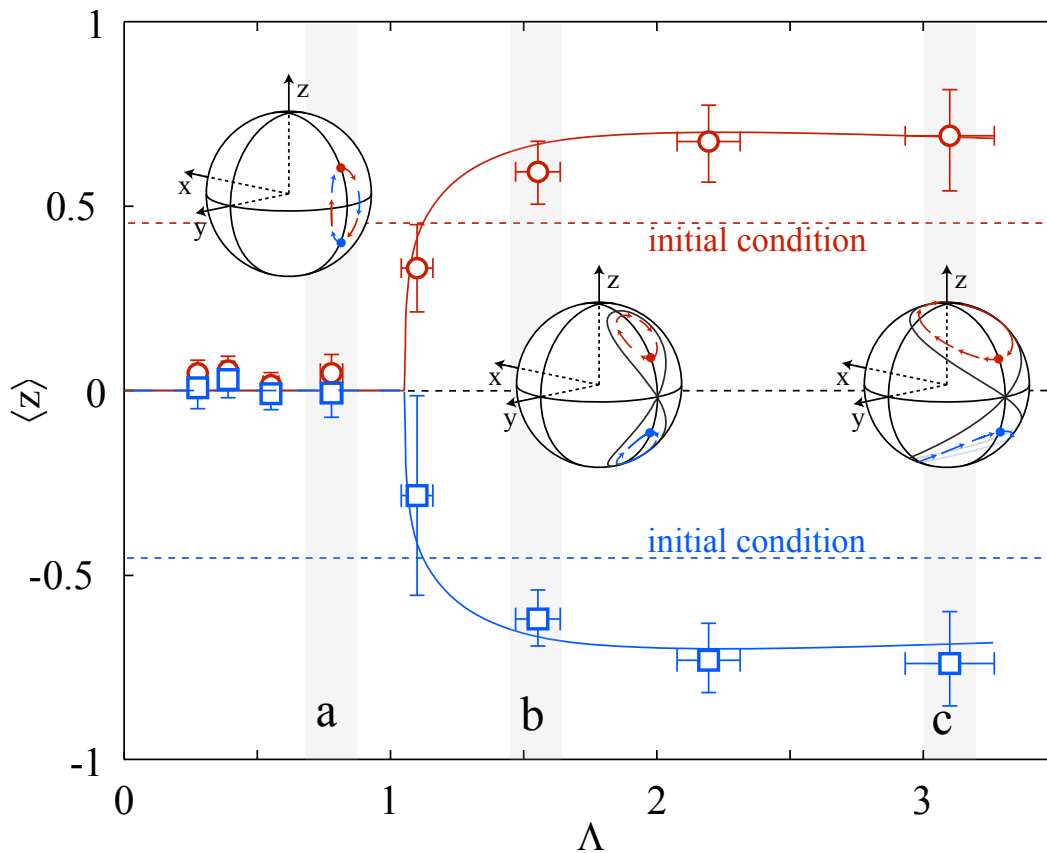


**Figure 4.9:** Direct observation of the topological change in the dynamics due to the bifurcation. Two initial states symmetric in the upper and lower hemisphere (see the inset) lead to qualitatively different dynamics in the Rabi and Josephson regime, respectively. In the Rabi regime both initial states share the same trajectory around the stable fixed point  $F_\pi$ , and the temporal mean imbalance vanishes in both cases. By increasing  $\Lambda$  over the critical value a separatrix is formed. If the initial preparation lies within this separatrix the trajectories are distinct showing a nonvanishing mean. The solid lines are the theoretical prediction.

For a quantitative experimental study of the bifurcation phenomenon and the associated topological change in the phase space, we study the temporal mean imbalance of two fixed initial preparations for different  $\Lambda$ . These initial preparation

points are chosen symmetrically on the northern and southern hemisphere and both with an initial phase of  $\pi$ . By analyzing the temporal mean of the subsequent evolution over a full oscillation one expects to observe a different behavior in the Rabi regime in contrast to the Josephson regime. This can be seen in figure 4.9. For  $\Lambda < 1$ , i. e. the Rabi regime one finds the temporal mean imbalance for the two preparations to be equal and zero within the measured precision. This can be easily understood from a symmetry argument. In the case of zero detuning the Hamiltonian is symmetric with respect to the equator of the phase space implying also symmetric trajectories. In the Rabi regime the two initial preparations lie on the same trajectory which is a  $\pi$  oscillation around the stable fixed point  $F_\pi$  (see Bloch spheres in figure 4.9). Their temporal mean imbalance  $\langle z \rangle$  is therefore expected to be zero. In the Josephson regime however the two different preparations do not share the same trajectory any more, but the system is macroscopically self trapped above or below the equator, which is in good agreement with the experimental findings.

Although this method allows to demonstrate the topological change occurring in the phase space at the critical  $\Lambda$  it must not be confused with a direct measurement of the fixed points in the system. The theoretical dependence plotted in figure 4.9 is the theoretically expected behavior of the temporal mean which is different to the position of the fixed points. This behavior depends also on the exact initial preparation condition which was in our case  $(z, \varphi) = (\pm 0.45, \pi)$  indicated as dashed lines in the figure. For  $\Lambda = 1$  the bifurcation happens and the separatrix starts to grow by increasing  $\Lambda$ , while the fixed points  $F_\pm$  move in the direction of the poles. However the actual change in the temporal mean can only be detected if the initial preparation falls onto a trajectory enclosed by the separatrix. This means that the initial imbalance determines at which  $\Lambda$  the change happens in the measurement. However the difference from the critical  $\Lambda = 1$  is very small even for relatively large initial imbalances.

## 4.8 Measurement of the Phase Portrait

As described in section 4.6 the experiment allows us to prepare the system in an arbitrary coherent spin state and to read out both the imbalance  $z$  and the phase  $\varphi$  of the system's final state it has evolved to. This enables us to map out the phase portrait of the different types of trajectories. The results are shown in figure 4.10 for different  $\Lambda$ .

In panel (a) we are in the Rabi regime ( $\Lambda = 0.78$ ). Both plasma oscillations (blue symbols) and  $\pi$ -oscillations (red symbols) are experimentally observed. The solid lines correspond to the theoretical prediction which has no adjusted parameters. The  $\Lambda$  is fixed by an individual measurement of the Rabi frequency  $\Omega$  and the nonlinearity  $\chi$ . The only remaining parameter is the initial preparation of the trajectory. This is determined by calculating the corresponding energy of the measured points in the phase portrait. One therefore gets to the trajectory which is energetically closest to the measured points. The trajectories nicely show how the interaction of the atoms deforms the dynamics on the two sides of the sphere which is most clearly seen in the three dimensional picture of the Bloch sphere in the second row of the figure.

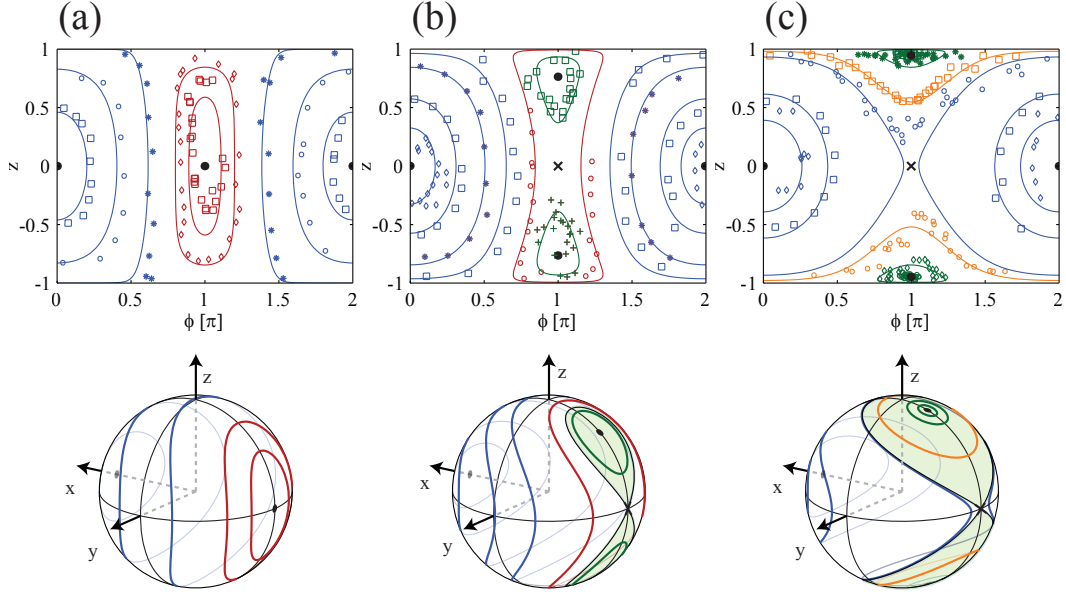


**Figure 4.10:** Experimentally observed phase portraits of the classical dynamics showing all possible kinds of trajectories. The experimental data for three different  $\Lambda$  are compared to the theoretical prediction without free parameter (solid lines). (a) Phase portrait in the Rabi regime for at  $\Lambda = 0.78$ . Plasma (blue) and  $\pi$ -oscillations (red) can be clearly identified. The corresponding Bloch sphere in the lower part shows the theoretical lines which clearly illustrates how the trajectories are deformed from pure circles due to the interaction. (b) The Josephson regime is entered by reducing the linear coupling  $\Omega$  ( $\Lambda = 1.55$ ). Here the bifurcation leads to topologically new trajectories around the emerged stable fixed points above and below the equator. This macroscopic quantum self trapping with mean phase  $\pi$  is demonstrated by the green crosses and squares. (c) The phase portrait at  $\Lambda = 3.1$  shows trajectories with running phase (orange squares and circles). These trajectories appear in the phase space for  $\Lambda > 2$  and are the analog to the ac-Josephson effect found in superconducting Josephson junctions.

Panel (b) shows a typical phase portrait observed in the Josephson regime of the dynamics slightly above the bifurcation ( $\Lambda = 1.55$ ). Here additionally macroscopically self trapped trajectories appear (green symbols). These trajectories illustrate how the interaction now dominates the dynamical behavior. The coupling is not strong enough to allow a transition of the majority of the atoms from one spin state to the other. The macroscopic self trapped trajectories show a mean phase of  $\langle \varphi \rangle = \pi$ .

For  $\Lambda > 2$  we expect self trapped trajectories showing a running behavior of their phase. This is experimentally demonstrated in the panel (c) of figure 4.10. Here the orange symbols are spread over all phases. However this characteristic is better visible in their temporal behavior discussed in the next section. Although the trajectory of the blue symbols also shows self trapped running phase behavior the theoretical description is that of a plasma oscillation with large amplitude. This discrepancy can be explained by a small error in the actual  $\Lambda$  or a small detuning.

## 4.9 The Temporal Behavior of the Dynamics

While the mapping out of the phase portrait shows in a clear way the topological change in the phase space the actual temporal behavior is hidden. Here we discuss this important aspect of the dynamics.

Figure 4.11 shows the dynamical behavior of the imbalance  $z$  and the phase  $\varphi$ . The data shown are a selection from the data presented in figure 4.10, with a one to one correspondence of the three panels. Colors and symbols are chosen accordingly.

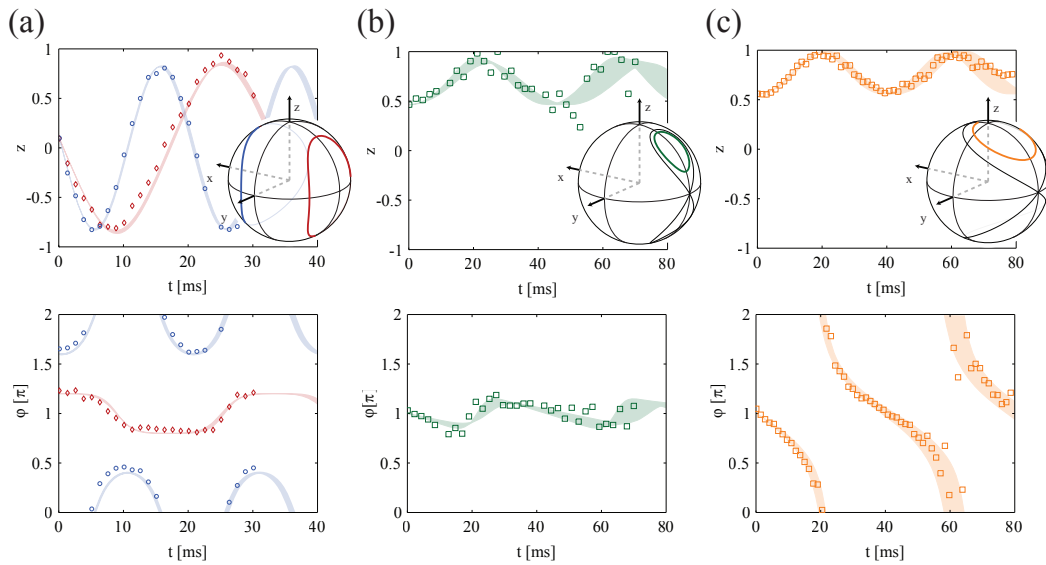


**Figure 4.11:** Exemplary time dynamics for of the population imbalance  $z$  and the phase  $\varphi$ . The shaded areas correspond to the theoretical predictions including a relative error of 5% in  $\Lambda$ . (a) Plasma (blue) and  $\pi$ -oscillations (red) in the Rabi regime ( $\Lambda = 0.78$ ). Although the dynamics are qualitatively similar the two oscillations differ in their frequency. This can be understood by the amplification or cancellation of the linear coupling and the nonlinearity on the two sides of the sphere. (b) Time trace of the macroscopic self trapping in the Josephson regime ( $\Lambda = 1.55$ ). The phase varies about its mean value of  $\pi$ . (c) Example of macroscopic self trapping at  $\Lambda = 3.1$ . The time trace has a very similar behavior in its imbalance  $z$ , however the phase shows running behavior. This is similar to the ac-Josephson effect found in superconductors.

The panel (a) shows plasma (blue) and  $\pi$ -oscillations (red). Although the amplitude of the two oscillation types is almost the same their temporal behavior reveals the slow-down of the  $\pi$ -oscillations compared to their counterpart. As briefly discussed already in section 2.6 and 3.5 this can be understood from the adding or canceling of the two terms in the Hamiltonian corresponding to the linear coupling and the nonlinearity.

For small amplitude oscillations the oscillation frequency of the plasma and  $\pi$ -oscillations is given by

$$\omega_{\text{Plasma},\pi} = \Omega\sqrt{1 \pm \Lambda},$$

where the plus sign corresponds to the higher frequency plasma oscillations.

The panel (b) shows the temporal behavior of self trapped  $\pi$ -oscillations. Here the phase behavior (lower part of panel (b)) oscillates in proximity to the temporal mean phase of  $\pi$ . This is different for the running phase behavior shown in the right panel of the figure. Here the phase runs without bound over the full span. The time scale in the middle and the right panel is the same. It is interesting to note that the temporal behavior of both dynamical processes is very similar in the imbalance  $z$ , although the linear coupling is only the half for the right panel. This demonstrates the strong effect of the nonlinearity on the temporal behavior of the dynamics.

# Chapter 5

## Quantum Behavior at the Unstable Classical Fixed Point

In the previous chapter the experimental investigation of the classical behavior of the two-mode system has been discussed. The classicality of the spin system is determined by its size, i.e. the total number of particles. In our experiments this particle number ranges typically between 100 and 1000 atoms. Although the preceding findings were in good agreement with the classical description this regime is at the boundary where quantum mechanical effects become important. Here *quantum mechanical effects* refers to all properties which are not covered by the classical description of the system's state in terms of a single point in the phase space.

As already discussed in section 2.4 the initial state of the system, a coherent spin state, has a finite isotropic uncertainty around its mean value. The nonlinear term in the dynamics redistributes this uncertainty in the phase space relative to its mean. The *quantumness* of the system can therefore be understood as the difference of the uncertainty region to that of a coherent spin state.

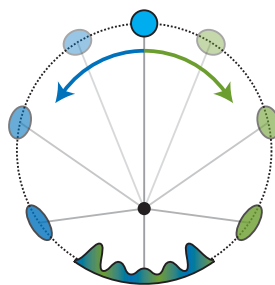


**Figure 5.1:** The *quantum mechanical* inverted pendulum

In this terminology we expect quantum mechanical behavior in every dynamical evolution of the system since it is given by the interplay of the nonlinearity and the linear coupling. However the effects of this quantum mechanical behavior are typically small and hard to verify in the experiment. To observe considerable quantum mechanical effects one has to choose an appropriate initial preparation which reveals the effects during its time evolution on an experimentally feasible timescale [58].

To study the quantum mechanical behavior the most interesting point in the phase space is the unstable classical fixed point  $F_\pi$  in the Josephson regime, which is clearly illustrated by the pendulum analogy. The point corresponds to a preparation of an inverted pendulum resting in its unstable upward position. The quantum case implies an uncertainty of position and momentum of the pendulum around the stable fixed point, given by the quantum mechanical wave function. We therefore expect that the left and right part of the wave function will start to move in their respective directions. The pendulum will not stay in the upwards position but a superposition of left and right will swing down on either side. When the two coherent pendulums reach the lower turning point we expect interference between the two parts of the wave function similar to Young's double slit experiment. This analogy is illustrated in figure 5.1.

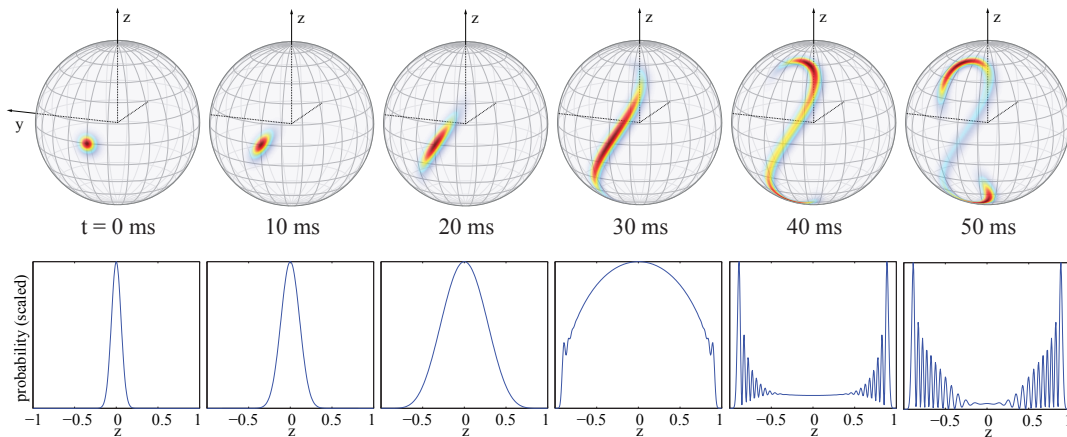


**Figure 5.2:** Quantum mechanical evolution of a coherent spin state prepared on the unstable fixed point in the Josephson regime in snapshots. The upper part shows the calculated Husimi distributions of several time steps. The state gets stretched along the separatrix. In the beginning of the time evolution the uncertainty region has an elliptical shape, for longer times a mirrored S-shape builds up. After a certain time the state distribution shows two maxima on the northern and southern hemisphere corresponding to a macroscopic quantum superposition state. For even longer times these maxima return to the initial preparation point. The lower part shows the corresponding distributions for the relative imbalance, i.e. the projection onto the  $z$ -axis. When the macroscopic superposition is reached the two maxima show up as narrow peaks in the probability distribution which are accompanied by several interference fringes.

The preparation at the unstable fixed point has been extensively studied theoretically [15, 45, 59, 60, 61, 62]. The upper part in figure 5.2 shows the quantum mechanical dynamics in form of snapshots of the Husimi distribution for typical experimental parameters. The initial coherent spin state is prepared on the unstable fixed point, i.e. the crossing of the separatrix. The dynamics stretch its uncertainty distribution along the separatrix. For short times this leads to an elliptical Husimi distribution, for longer times the uncertainty evolves into a mirrored S-shape. After a certain time the maximum of the probability distribution is not any more located

at the unstable fixed point, but simultaneously at two symmetric points on the northern and southern hemisphere, i.e. a macroscopic superposition is reached. In contrast to the scheme of Yurke and Stoler [63] this macroscopic superposition is reached in an experimentally feasible time. For even longer times not shown in the figure the two maxima move back in the direction of the unstable fixed point. For all times, the expectation values  $\langle \hat{J}_z \rangle$  and  $\langle \hat{J}_y \rangle$  remain zero due to the symmetric evolution, corresponding to the rest of the classical pendulum at its unstable fixed point as expected.

Although the Husimi distribution gives a nice impression of the dynamics in the quantum mechanical Hilbert space, its connection to actual measurements is typically less obvious. More insight is given by the probability distribution of the imbalance<sup>1</sup> which is shown in the second row of plots in figure 5.2. For short times this function spreads but keeps its approximately Gaussian shape. When the macroscopic superposition has built up the probability distribution not only shows two pronounced peaks at the maxima but also shows interference fringes in between the maxima, a signature of the coherent character of the superposition.

In a repeated measurement of the imbalance of the macroscopic superposition state this distribution means that it is very likely that one randomly finds almost all atoms in one of the spin states. The macroscopic number of atoms *decides* in the instant of the measurement in which of the two states they mainly show up, i.e. the atoms are entangled. This entanglement is produced by the inter atom interaction.

In this work we focus on the dynamical time evolution until a macroscopic superposition is reached. The longer time scales are experimentally less feasible since the effect of many experimental imperfections (see sec 3.8) grows with the evolution time.

## 5.1 Spin Squeezing

As shown in figure 5.2 the time evolution to a macroscopic superposition state begins with a redistribution of the circular uncertainty of the initial coherent spin state into an elliptically shaped uncertainty region. A closer look at the associated variances of the state reveals that while the variance along the separatrix of the state is increased, the perpendicular variance is decreased relative to the variance of a coherent spin state. Such a scenario is called spin squeezing in reference to the squeezing of light in quantum optics [64]. In both cases the variance is redistributed between two non commuting observables. This redistribution can be used to improve interferometric measurements as will be discussed in the following.

---

<sup>1</sup>The probability distribution for a state  $|\psi\rangle$  is given by  $p(z = \frac{2n}{N}) = |\langle N, n | \psi \rangle|^2$ . Although the distribution is discrete the atom number of several hundred atoms motivates the treatment as a continuous function here and in the following

### 5.1.1 Number Squeezing and the Standard Quantum Limit

The reduction of the variance, i.e. squeezing of a spin state is usually measured by the so called number squeezing factor

$$\xi_N^2 = \frac{(\Delta\hat{J})^2}{\Delta_{\text{CSS}}^2} = \frac{2(\Delta\hat{J})^2}{J(1 - \langle\hat{J}\rangle^2/J^2)}, \quad (5.1)$$

which relates the variance of a general angular momentum operator  $\hat{J}$  to the variance of the coherent spin state with the same mean value  $\langle\hat{J}\rangle$  [23, 65]. The variance of the CSS is often referred to as the standard quantum limit. This limit originates from the separability of the CSS as explained in section 2.4. The term  $\langle\hat{J}\rangle^2/J^2$  in equation 5.1 accounts for the reduced fluctuations expected for a coherent spin state with finite mean. Typically the direction of  $\hat{J}$  is chosen such that this mean vanishes, which means  $\hat{J}$  is lying in a plane perpendicular to the mean spin direction of the state. For non-isotropic states such as squeezed spin states  $\xi_N^2$  shows a sinusoidal behavior depending on the particular direction of  $\hat{J}$  in that plane, which can be parametrized by an angle  $\alpha$ . This sinusoidal behavior stems from the elliptical nature of the variance.

### 5.1.2 Improvement of Interferometry using Spin Squeezed States

The idea of using squeezed states for interferometry is motivated by the hope that the reduced uncertainty of these states in a certain direction can be used to improve the signal to noise ratio and therefore the sensitivity of such devices. In atomic systems such an interferometer is typically of the Ramsey type [47, 66]. The basic idea of the Ramsey interferometer can be reduced to the following sequence. A two mode system is brought into a superposition state by coupling of the two modes. The coherent superposition accumulates a differential phase shift during a free evolution time. This phase shift is translated into a population difference between the two modes by a final coupling. The population difference which is measured in the end of the sequence is directly dependent on the accumulated phase shift.

When the system is composed of many independent two mode systems the final state is given by a coherent spin state. The fluctuation of the relative populations given by the coherent spin state are therefore a fundamental lower limit on the measurement noise in such a system. This noise is referred to as projection noise or shot noise and is limiting many state of the art atom interferometers [67, 68]. However, if the interferometer is performed using a squeezed spin state as the input state, which has reduced fluctuations this fundamental limit can be overcome.

The precision of the phase measurement  $\Delta\phi$  of an interferometer is not only given by the noise of its output  $\Delta\hat{J}$ , but depends also on its sensitivity  $\frac{\partial\langle\hat{J}\rangle}{\partial\phi}$ :

$$\Delta\phi = \left(\frac{\partial\langle\hat{J}\rangle}{\partial\phi}\right)^{-1} \Delta\hat{J}. \quad (5.2)$$

Wineland et al. pointed out that the spin squeezed states employed in a Ramsey interferometer have a reduced sensitivity compared to coherent spin states [65]. This can be understood by the fact that the uncertainty of the spin squeezed states is

more spread along the long axis of the states compared to a coherent spin state. This leads to an effective reduction of the mean spin length  $\langle \hat{\mathbf{J}} \rangle^2 = \langle \hat{J}_x \rangle^2 + \langle \hat{J}_y \rangle^2 + \langle \hat{J}_z \rangle^2$ , which appears as reduced visibility of the Ramsey fringe.

However, the gain through reduction of the noise can exceed the loss of sensitivity, implying the usefulness of spin squeezed states for Ramsey interferometry. The improvement in precision of such an interferometer over a standard one using a coherent spin state of the same number of particles is given by the so called coherent spin squeezing parameter

$$\xi_R^2 = \frac{J^2}{\langle \hat{\mathbf{J}} \rangle^2} \xi_N^2, \quad (5.3)$$

as

$$\Delta\phi = \xi_R \Delta\phi_{\text{CSS}}, \quad (5.4)$$

where  $\xi_R < 1$  is directly connected to an improvement of precision.

### 5.1.3 Entanglement and Squeezing

A multi particle state described by the density operator  $\hat{\rho}$  is entangled if it can not be written in the following form,

$$\hat{\rho} = \sum_k p_k \hat{\rho}_k^{(1)} \otimes \hat{\rho}_k^{(2)} \otimes \dots \otimes \hat{\rho}_k^{(N)}, \quad (5.5)$$

where all  $\hat{\rho}_k^{(j)}$  are single particle density operators, and  $p_k$  are probabilities allowing all mixtures. Sørensen et al. pointed out that the coherent squeezing parameter  $\xi_R < 1$  not only states the improvement of an interferometer but is also directly related to entanglement [69]. The entanglement associated with spin states which differ from coherent spin states is expected from the considerations in section 2.4, however for a general spin state it is not easy to show the underlying entanglement. The entanglement criterion of Sørensen et al. is a so called entanglement witness, meaning that a state is not necessary separable if  $\xi_R \geq 1$ . However, it can be applied for the detection of entanglement in the beginning of the time evolution as will be discussed below. A general overview of entanglement witnesses for squeezed spin systems is found in the references [70, 71].

## 5.2 Systematic Measurements of the Dynamical Spin Squeezing

In this section we discuss the temporal evolution of the squeezing parameters for the initial preparation of the coherent spin state at the unstable fixed point.

Figure 5.3 shows the measured number squeezing parameter  $\xi_N^2$  for different times of the dynamical evolution and different measurement axis in the  $z-y$  plane which is approximately perpendicular to the mean spin direction. The angle  $\alpha$  parametrizes the measurement axis with respect to the  $z$  axis. The number squeezing parameter is shown with (lower points with two standard deviation errorbars) and without (upper points) the subtraction of the photon shot noise originating from the imaging process (see section 3.7). This subtraction is especially important for the small variances.

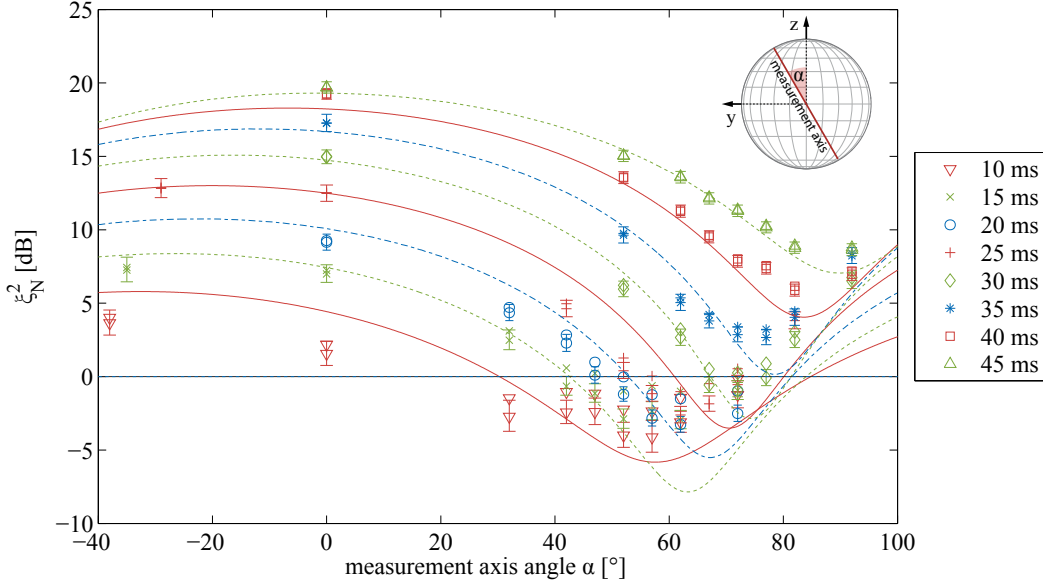


**Figure 5.3:** Number squeezing versus measurement axis angle (defined in the inset) for different times of the evolution. The final total atom number is post selected between 315 and 365 atoms. Solid lines are a numerical simulation without free parameters. Upper and lower points correspond to the data with and without the subtraction of photon shot noise in the imaging process respectively. The errorbars indicate two standard deviations for the respective lower points. Number squeezing below the shot noise limit is found for evolution times shorter than 35 ms.

For short times the measurement demonstrates number squeezing at angles around  $60^\circ$  with and without the subtraction of the photon shot noise. This angle corresponds to the angle of the separatrix with respect to the  $y$  axis. For times longer than 30 ms no variance below the shot noise limit is found any more. The lines correspond to a theoretical simulation of the dynamical evolution which is detailed in section 5.6 with no free parameters. It captures the most important features of the dynamical evolution. The sinusoidal dependence of  $\xi_N^2$  with the angle, that was mentioned in section 5.1.1 is hard to recognize in the logarithmic scale.

As was detailed in section 5.1.2 a possible interferometric improvement of the state is detected by the coherent spin squeezing factor  $\xi_R$ . While for high visibilities its reduction is typically hard to estimate experimentally, knowledge of the long and the short axis of the number squeezing factor is sufficient to deduce the coherent spin squeezing. To accurately measure the two axis one needs to measure exactly along the right angles. To circumvent this one can also fit a sine to the measured number squeezing and deduce the maximum and minimum. The fitted curves are in very good agreement with the measured data in our case. The deduced quantities are shown in figure 5.4. The minimum of the sine fit, and the deduced coherent spin squeezing are shown (red circles and red crosses). We find coherent spin squeezing ( $\xi_R^2 < 1$ ) for evolution times up to 30 ms which can be directly related to entanglement in the system. The coherent spin squeezing and number squeezing differ only very slightly for short evolution times where the state is still relatively well

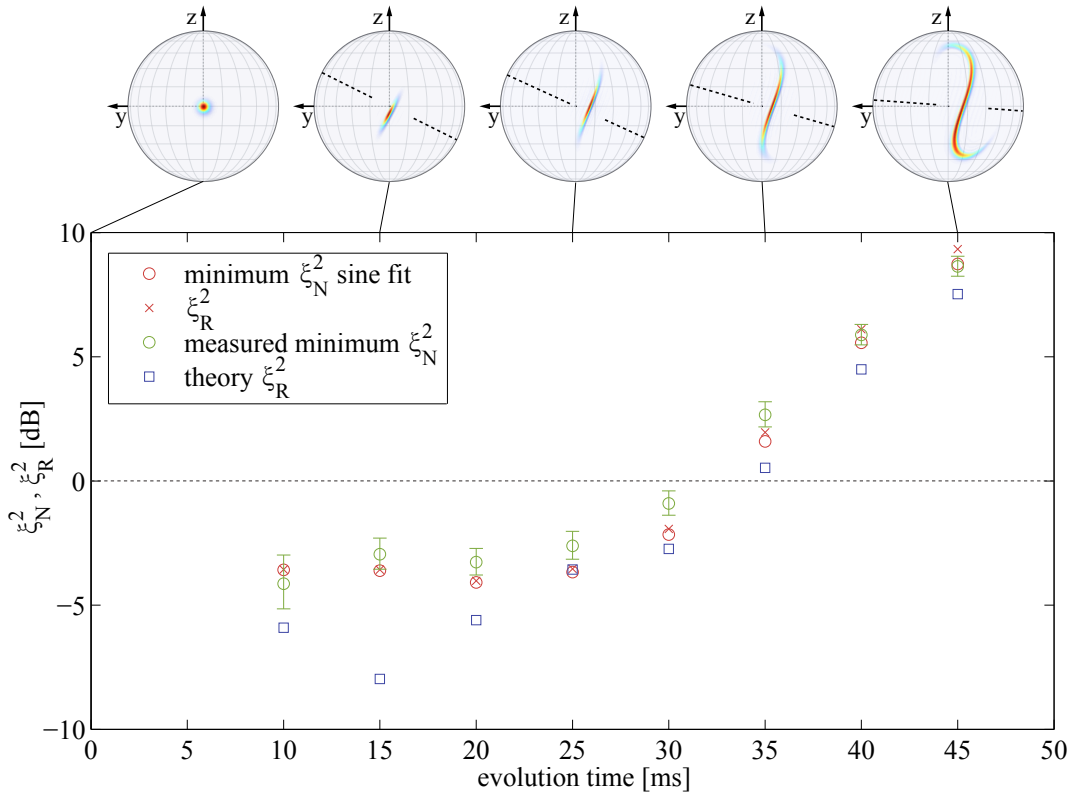


**Figure 5.4:** Time dependence of the minimal number squeezing and coherent spin squeezing. The coherent spin squeezing (red crosses) is deduced from a sine fit to the measured variance data with photon shot noise subtracted. For small evolution times the difference to the fitted number squeezing (red circles) is very small, since the state is still very localized on the sphere. The actual measured number squeezing is shown as green circles where the error bars indicate the two standard deviations. Blue squares indicate the coherent spin squeezing found in the numerical simulation of the time evolution. The deviation to the measured quantity is especially apparent for the small variances where detection noise limits the measured squeezing. The Wigner distributions in the upper part are deduced from theoretical simulations and give an impression of the shape of the state at different stages of the evolution. The dotted lines indicate the measurement direction in which the minimal number squeezing is found experimentally.

localized. The fitted minimum is also in good agreement with the corresponding measured minimum value of the squeezing (green circles with 2 s.d. errorbars). The blue squares show the theoretically expected coherent spin squeezing from the numerical simulation. These values lie systematically below the measured values, which is expected because of the additional excess noise in the experiment. This deviation is especially apparent for short evolution times where the squeezing is maximal.

The upper part of the figure shows the theoretically expected Wigner distributions which give an impression of the shape of the spin state at the different time

steps. The Wigner distribution allows to understand the increase of the fluctuations for long times, the variances along all axes of the distribution are much higher than for a coherent spin state (Wigner distribution at time  $t = 0$ ). The Wigner distribution for the spin system will be explained in more detail in section 5.4.1.

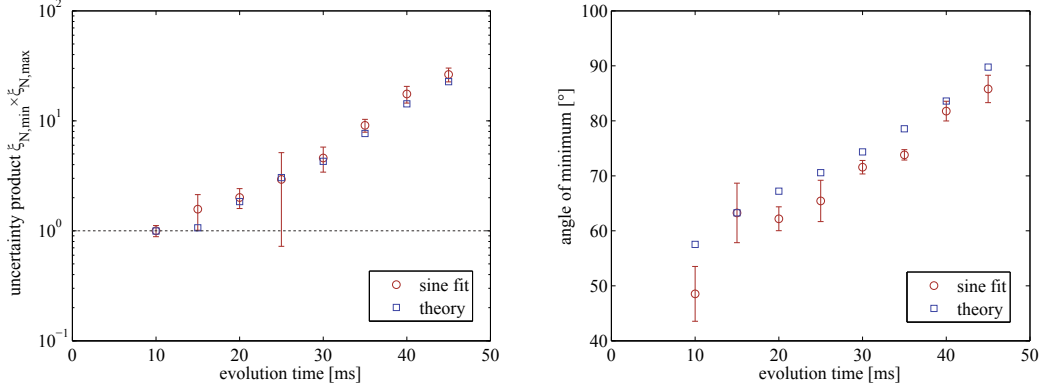


**Figure 5.5:** (left) Uncertainty product of the state deduced from the sinusoidal fit to the data (red circles). After 10 ms of evolution the state is still at the Heisenberg limit (dashed line) but shows a raising behavior for longer times. The error bars correspond to a 5% confidence level of the fitted parameters. The theoretical prediction (squares) shows good agreement with the measurement. (right) Angle of measurement axis where the minimal squeezing parameter is found. The increase of the angle is mainly due to the decay of the system parameter  $\Lambda$  as explained in section 5.5.2. The optimal angles deduced from the numerical simulation are shown as blue squares.

As was described in section 2.4 the coherent spin states are states with minimal uncertainty. This is not the case for the states generated by the dynamics for longer times. The left panel in figure 5.5 shows the product of the minimum and the maximum number squeezing factor  $\xi_N^2$ . After 10 ms of evolution the state is still at the limit allowed by the Heisenberg uncertainty relation (dashed line). For longer evolution times the uncertainty increases up to 25 times the Heisenberg limit. This behavior is in good agreement with the theoretical prediction (blue squares).

The right panel of figure 5.5 shows the time dependence of the angle where the minimal uncertainty is found. This angle increases during the whole time evolution which is not expected in the ideal time evolution for short times. The uncertainty region of the quantum state is stretched along the separatrix which is well described by a line in proximity to the initial preparation point. This suggests that the minimal variance should be found perpendicular to this line at a constant angle. However, the loss of atoms changes the effective nonlinearity during the time evolution causing a change of the separatrix. This is reflected by the increase of the angle which is also found in the theoretical prediction.

### 5.3 Quantum Fisher Information

As was shown in the section before, for long evolution times the variance of the state increases in all directions above that of the corresponding coherent spin state and the usability of the state in an interferometer decreases below the standard quantum limit. This behavior originates not from the experimental noise, but is intrinsic to very dislocated states on the Bloch sphere. The measurement precision of these states in a normal Ramsey type interferometer is therefore reduced.

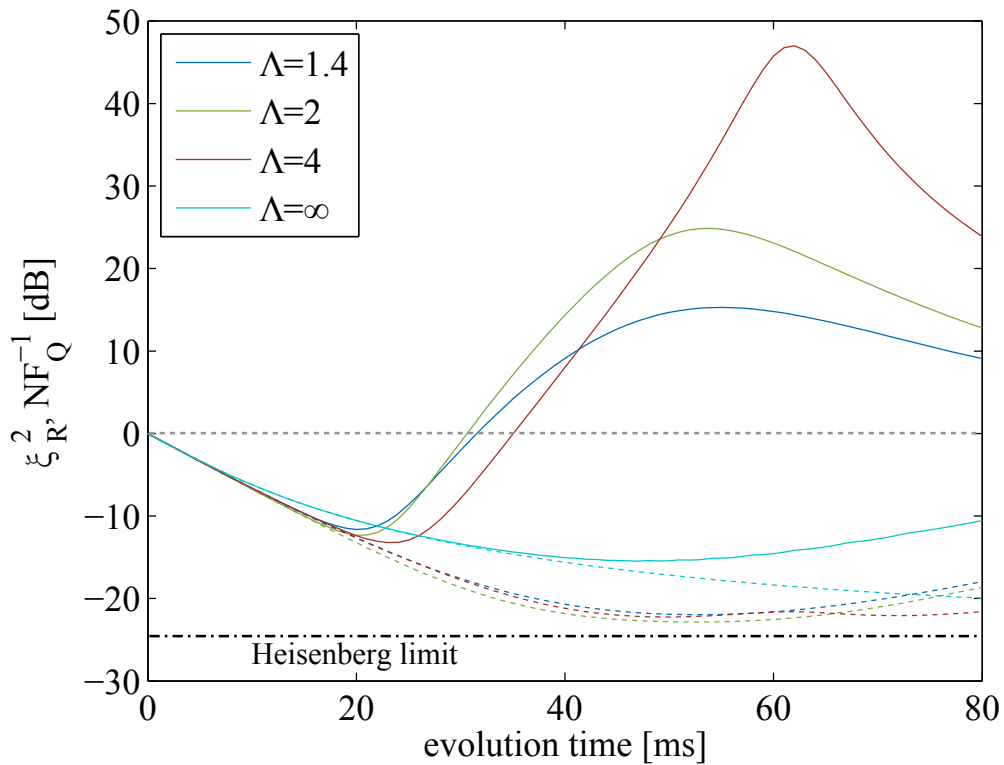


**Figure 5.6:** Comparison between coherent spin squeezing  $\xi_R^2$  (solid lines) and the possible precision gain in terms of the quantum Fisher information  $NF_Q^{-1}$  (dotted lines). The different colors correspond to different  $\Lambda$  originating from a fixed nonlinearity  $\chi$  but different coupling strength  $\Omega$ . This is similar to the situation found in the experiment where one is typically limited by the strength of the nonlinearity. The possible gain in interferometry given by the quantum Fisher information exceeds the gain found by  $\xi_R^2$  by far for evolution times longer than about 20 ms.  $\Lambda = \infty$  corresponds to the single axis twisting scheme as proposed by Kitagawa and Ueda [23] used in the experiments in references [25, 24]. For a given nonlinearity this method is slowest in terms of possible interferometric gain, but allows for a simple readout since the coherent squeezing factor is still good measure for its phase sensitivity at long evolution times. The dash-dotted line corresponds to the Heisenberg limit  $1/N^2$  for the 300 atoms in the simulation. The dynamical generation of entanglement in principle allows to approach this limit on a short time scale.

However, it can be shown that the gain in interferometric precision for a quantum state is not necessarily given by its coherent squeezing parameter  $\xi_R^2$ . The usefulness of many states can be drastically increased by a more general state readout. In a normal Ramsey interferometer the interferometric signal is given as the mean position of the final state. Generalizing the readout to all possible positive-operator valued measures a much higher sensitivity can be reached for some quantum states.

Generally it can be shown that the phase estimation by an interferometer is limited by the so called quantum Cramer-Rao bound [72, 73]. This bound places a lower limit on the achievable precision in an interferometer and is given by

$$\Delta\phi \geq \frac{1}{\sqrt{F_Q(\hat{\rho}, \hat{J})}}, \quad (5.6)$$

Here  $F_Q(\hat{\rho}, \hat{J})$  denotes the quantum Fisher information of the state.

Ronald Fisher introduced a measure in classical statistics for the information carried by a probability distribution about an unknown parameter [74]. This concept was successfully transferred to quantum measurement theory leading to the above analog of the classical Cramer-Rao bound. The quantum Fisher information for a given density operator  $\hat{\rho}$  is given as

$$F_Q(\hat{\rho}, \hat{J}) = 2 \sum_{l,k} \frac{(p_j - p_k)^2}{p_j + p_k} |\langle j | \hat{J} | k \rangle|^2 \quad (5.7)$$

Here  $|j\rangle$  is a set of orthonormal states diagonalizing the density operator, and  $p_j$  the corresponding diagonal entries<sup>2</sup>. The general angular momentum operator  $\hat{J}$  is the generator of the unitary rotation of the interferometer. It is clear from the definition that not all choices of  $\hat{J}$  assure optimal interferometric precision. Further the measurements have to be analyzed in an optimal way. The quantum Fisher information can be obtained from the classical Fisher information maximized over all possible measurement protocols [75], where the classical Fisher information can be retrieved by maximum likelihood estimation [76]. In general it is possible to reach the quantum Cramer-Rao bound in an experiment [73], which has been experimentally demonstrated by means of a maximum likelihood and a Bayesian estimation protocol [77]. However, especially for large quantum systems, the optimal measurement and estimation protocol can be very complicated and difficult to find. Once a Fisher information larger than the number of particles is detected, it allows to make a statement about the entanglement present in the system similar to the case of the coherent spin squeezing factor [78].

Figure 5.6 shows the expected coherent spin squeezing  $\xi_R^2$  and the normalized gain expected from the optimal quantum Fisher information  $NF_{Q,max}^{-1}$ , for different parameters  $\Lambda$ . The coherent spin squeezing is lost after some time similar to the experimental results presented in section 5.2 and [79]. However, the principal gain in an interferometer which is measured by the quantum Fisher information still increases. The dash-dotted line in the figure shows the Heisenberg limit  $1/N^2$ , which corresponds to the highest precision attainable in the framework of quantum mechanics, is theoretically approached.

---

<sup>2</sup> $\hat{\rho} = \sum_j p_j |j\rangle\langle j|$

For comparison also the case of  $\Lambda = \infty$  is shown. Since the nonlinearity is fixed in this simulation, this case corresponds to a evolution with pure nonlinear interactions, i.e. the one axis twisting scheme proposed by Kitagawa and Ueda[23]. This method of spin squeezing has been demonstrated experimentally [25, 24]. The comparison of the dynamical generation of squeezing at the unstable fixed point to this method reveals that the generation of squeezing is faster for the first case, which is an important advantage since the generation time in the experiments is typically limited by other processes such as decoherence. On the other hand the comparison of the coherent spin squeezing factor to the Cramer-Rao bound in the case of the one axis twisting ( $\Lambda = \infty$ ) shows, that it is possible to reach strong squeezing without complicated analysis of the output state even for long evolution times. However, the Fisher information reveals that the dynamical generation of squeezing realized in this work has the ability to produce highly entangled states which approach the Heisenberg limit on an experimentally feasible timescale.

## 5.4 State Tomography

Analog to the classical case where the state of the system was characterized by the imbalance  $z$  and the phase  $\phi$ , the state of the quantum mechanical case can not be characterized by a measurement of the imbalance  $z$  distribution alone, but depends also on its distribution in the other directions of the phase space. To characterize the state of the system one has to measure in different measurement directions as was already shown in the squeezing measurements discussed before (see section 5.1). Here we will explain in more detail how this tomographic method works in the experiment.

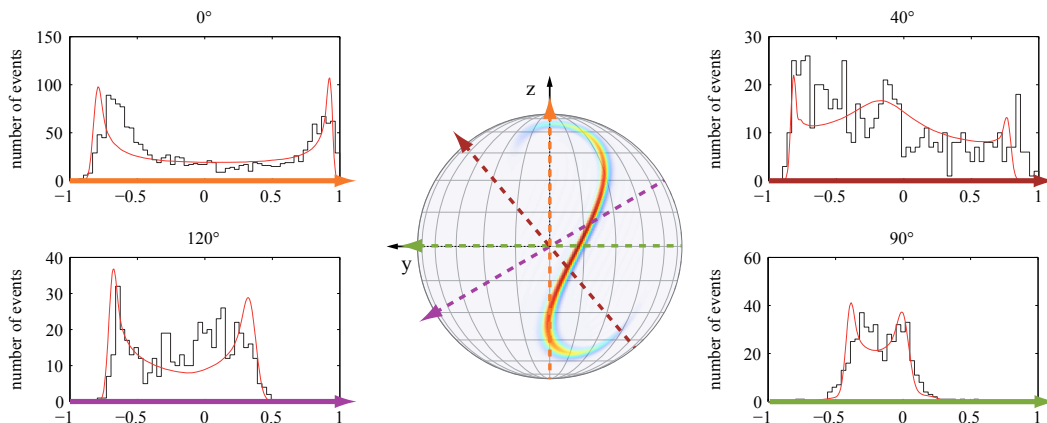


**Figure 5.7:** Histograms of the imbalance measured along different directions in the  $z - y$  plane. The Bloch sphere in the center shows the theoretically expected Wigner function of the state. The different measurement directions are shown as colored arrows in the histograms and on the sphere. The angle between the  $z$ -axis and the measurement axis is indicated above the histograms. The red solid lines in the histograms correspond to the theoretical expectations.

The principle is very similar to the classical case where the phase was obtained

by applying a unitary rotation of  $90^\circ$  before the readout. In the quantum mechanical case we use a unitary rotation to translate an arbitrary axis into the direction of the  $z$  axis. With this method repeated measurements allow us to measure a histogram corresponding to the empirical probability distribution in an arbitrary measurement axis. However the gain in information about a specific state is not equally distributed over all different measurement directions. At least for localized states the gain in information is highest for measurements performed in directions perpendicular to the mean of the state, i.e. the histograms are centered with respect to the imbalance. For our case where the mean of the state is found approximately in the negative  $x$ -direction tomographic measurements are favorably performed by measurements in the  $z - y$  plane. An example of such measurements is shown in figure 5.7. In the following we will describe how these types of measurements allow for the reconstruction of the Wigner function and an estimation of the density operator of the state.

### 5.4.1 Wigner Distribution on the Bloch Sphere

The Wigner distribution was introduced by Eugene Wigner as a quantum mechanical analog to the classical phase space density [80]. In contrast to its classical analog it is not a probability distribution due to its possible negativity. The negativity of the Wigner distribution is considered as a sign of the quantum mechanical character of the system and is typically associated to interference of the quantum mechanical wave function. In textbooks the Wigner distribution is typically defined for conjugate variables like position and momentum or the quadratures of the light field in a planar phase space.

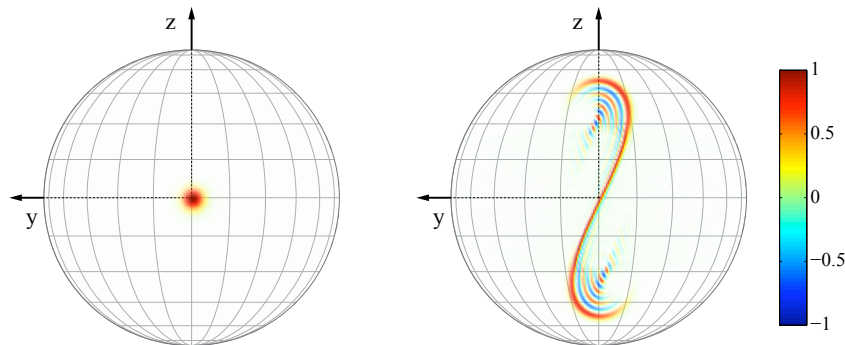


**Figure 5.8:** Wigner distributions for a coherent spin state (left) and exemplary final macroscopic superposition state (right). The Fringes in the probability distribution of the superposition state can be identified with the negative regions present in its Wigner distribution. In contrast the *classical* coherent spin state shows no negativity in its Wigner representation as expected.

Scully and Cohen introduced the Wigner function for spin-1/2 particles [81, 82], while Agarwal found a definition for arbitrary angular momentum in spherical phase space using spherical tensors [83]. This method can be directly applied to get the Wigner function of a collection of two mode systems [84]. The Wigner function  $W(\vartheta, \varphi)$  of a  $j$ -spin system is given by

$$W(\vartheta, \varphi) = \sum_{k=0}^{2j} \sum_{q=-k}^k \rho_{kq} Y_{kq}(\vartheta, \varphi), \quad (5.8)$$

where the coefficients  $\rho_{kq}$ , determining the contribution of the usual spherical harmonics  $Y_{kq}$ , are given by

$$\rho_{kq} = \text{Tr}(\hat{\rho} \hat{T}_{kq}^\dagger). \quad (5.9)$$

Here the state's density operator  $\hat{\rho}$  enters, and  $\hat{T}_{kq}$  are the spherical tensors [85]. The matrix elements of the spherical tensors are given by the Wigner-Eckart theorem in terms of Clebsch-Gordan coefficients<sup>3</sup>[19]. An example of a Wigner function of the initial coherent spin state and a final superposition state after a perfect evolution is shown in figure 5.8.

### 5.4.2 Reconstruction of the Wigner Function by a Filtered Back Projection Algorithm

The data gained by a tomographic measurement of the state can be used to reconstruct the Wigner function of the state by a filtered back projection algorithm [87]. This algorithm works similar to the inverse radon transformation, which is used to reconstruct planar Wigner distributions found in nonlinear optics [88, 89] as well as X-ray computed tomography images in medicine [90].

The used algorithm has the advantage that it is insensitive to experimental fluctuations in the total atom number. This comes from the fact that the Wigner distributions of a similar state for slightly different total atom numbers are very similar. The algorithm provides the  $\rho_{kq}$  coefficients appearing in the definition of the Wigner function. In principle all  $(2j + 1)^2$  coefficients can be extracted that way as long as it is possible to get enough data. However, experimental noise in the final state detection reduces the usefulness of the higher order terms which are responsible for the small scale variations of the Wigner distribution. This problem can be circumvented by introducing a damping of the higher order terms which accounts for the uncertainties in the detected atom number and the angle of the tomography axis in the state detection as suggested in [87]. This leads effectively to a damping of high spatial frequency contributions.

Figure 5.9 compares the Wigner distributions gained by the back projection algorithm (center column) to simulated Wigner distributions with (right column) and without including noise contributions (left column). The upper and lower row correspond to different coupling strengths  $\Omega$ . The negativity of the Wigner distribution present in the perfect evolution without noise is neither found in the reconstructed data nor in the simulation including noise. A possible explanation for this is found in section 5.5.2. The negativity found in the measured Wigner distribution all over the sphere is due to noise and the finite data set used for the reconstruction.

This shows also a major drawback of the filtered back projection algorithm. Valid quantum mechanical density operators are positive semi-definite. This requirement

<sup>3</sup>In practice the analytical Racah formula for calculating the appearing Wigner 3j symbols is hard to evaluate for large angular momentum. A numerical method by Schulten et al. has proven to be extremely useful for us, for a practicable calculation of the Wigner distribution[86].

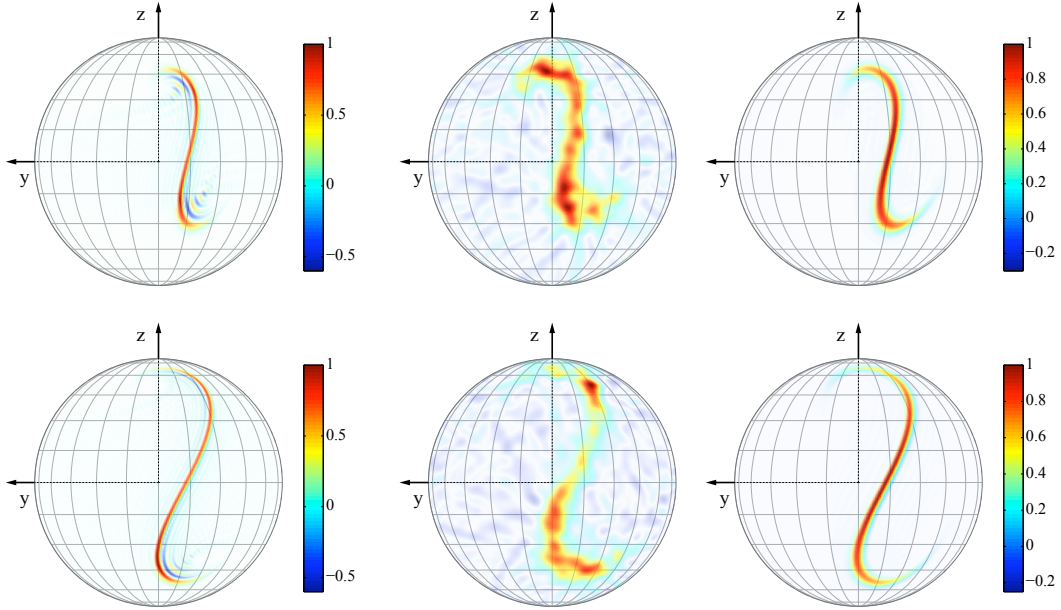


**Figure 5.9:** Wigner distribution obtained from the filtered backprojection algorithm (middle) compared to the numerical simulations for the evolution without noise (left) and with simulated noise in the detuning and the nonlinearity (right). The two rows correspond to two different coupling strength  $\Omega = 2\pi \times 21$  Hz for the upper row and  $\Omega = 2\pi \times 16.7$  Hz for the lower row. The large negative values found in the simulation without noise (see left color scale) which correspond to the interference fringes is neither found in the back projected Wigner distribution nor in the simulation including noise contributions (color scale for both on the right). Although the back projected distribution includes a smooth decay of the higher order terms accounting for the detection noise (see [87]), negative noise appear in the Wigner distribution. The data obtained after an evolution time of 45 ms was post selected with respect to the final total atom number from 310-340. Both data sets include a total of  $\sim 13000$  realizations distributed over 25 different measurement directions in the  $x - y$  plane. The full set of data is shown in the histograms in appendix B.

is not ensured by the filtered back projection algorithm for finite data sets. However, as the comparison with the simulated Wigner function shows the reconstructed Wigner functions allow to illustrate the qualitative shape of the quantum state very well.

### 5.4.3 Maximum Likelihood Estimation of the Density Matrix

The quantum state of the system is fully characterized by its density matrix  $\hat{\rho}$ . It is therefore desirable to retrieve this quantity from repeated measurements on the system. This can be done by a maximum likelihood estimation of the real density matrix [91, 92], which has been shown in experiments on light [88], molecules [93], ions [94] and an atomic beam [95]. The size of these systems was typically on the

order of several quanta. The number of free real parameters in a density matrix is given by  $(n + 1)^2 - 1$  where  $n$  denotes the number of quanta. The small size of the system allowed to give an accurate estimation of the density matrix within a accessible number of measurements.

For a typical atom number of 300 atoms as in our experiment the density matrix has 90600 independent real parameters. It is therefore not possible to gain enough information of such a large quantum system to give a very accurate estimation of the density matrix in the current state of the art experiments. Nevertheless, the method of maximum likelihood estimation does not loose its validity if the number of measurements is lower than the free parameters of the density operator. One only has to expect a higher uncertainty in the physical properties derived from the density operator. As we will see in the following the number of measurements performed on our system is sufficient to use the obtained density operator to get an alternative access to the state's Wigner distribution.

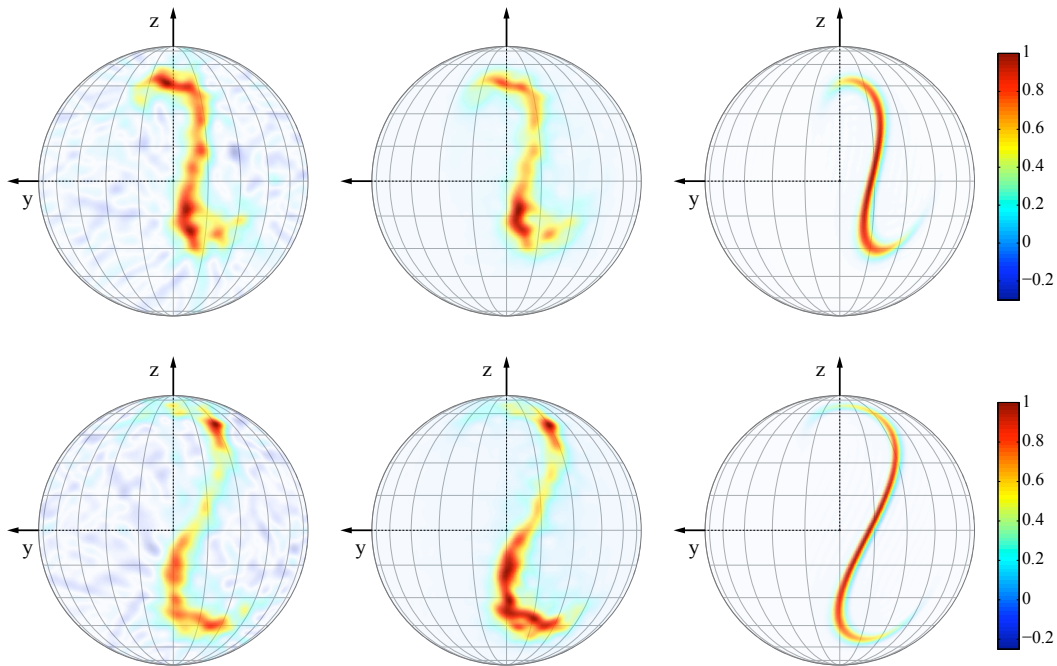


**Figure 5.10:** Comparison of the Wigner distributions obtained via filtered back projection (left column) and maximum likelihood estimation of the density operator (middle column) for the measurement data sets shown in appendix B. The maximum likelihood method produces a physical density operator which is not ensured by the back projection algorithm. This is apparent in the distribution shown by the total lack of negative noise for the case of the likelihood method. For comparison the theoretical expected Wigner distributions are shown in the right column.

There are many different solutions for the numerical problem of maximum likelihood estimation of the density operator of a large size quantum mechanical system. The method applied here is an algorithm which maximizes the likelihood in an iterative way [96]. The basic idea of this algorithm can be understood from the iteration

formula

$$\hat{\rho}^{(k+1)} = \mathcal{N} \left[ \hat{R}(\hat{\rho}^{(k)}) \hat{\rho}^{(k)} \hat{R}(\hat{\rho}^{(k)}) \right], \quad (5.10)$$

with the state dependent operator

$$\hat{R}(\hat{\rho}^{(k)}) = \sum_j \frac{f_j/n}{\text{Tr}(|\phi_j\rangle\langle\phi_j|\hat{\rho}^{(k)})} |\phi_j\rangle\langle\phi_j|. \quad (5.11)$$

Here  $\mathcal{N}$  denotes normalization,  $k$  is the iteration step and  $n$  the total number of measurements performed on the system. The different measurement outcomes are described by the projection operators  $|\phi_j\rangle\langle\phi_j|$  and the frequency of the measurement result  $j$  is given by  $f_j$ .

The basic idea behind this iteration formula is that  $\hat{R}(\rho(k))$  leads to a relative increase of the contribution of  $|\phi_j\rangle\langle\phi_j|$  in the step  $k + 1$  density operator  $\rho(k)$  if the relative empirical probability  $\frac{f_j}{n}$  exceeds the expected probability  $\text{Tr}(|\phi_j\rangle\langle\phi_j|\hat{\rho})$  for the step  $k$  density operator. The convergence of the algorithm is motivated by the identity

$$\hat{R}(\hat{\rho}_0)\hat{\rho}_0\hat{R}(\hat{\rho}_0) = \hat{\rho}_0, \quad (5.12)$$

which holds for large numbers of measurements and the real density operator  $\hat{\rho}_0$ , and the fact that the likelihood is increased in every iteration step [97].

The results of the application of this algorithm after 300 iteration steps starting from a totally mixed density operator  $\hat{\rho}(0) \propto \mathbb{1}$  with our measurement data can be seen in figure 5.10 in form of the Wigner distributions. Although stemming from the same data sets as the Wigner distributions from the filtered back projection algorithm (left column) the Wigner distributions obtained via maximum likelihood estimation (center column) look much closer to the distributions expected from the simulations (right column). They further lack the negative noise found in the back projection algorithm and correspond to a physical density operator.

## 5.5 Relevance of the Experimental Imperfections

The picture of the quantum pendulum given in the beginning of the chapter illustrates many of the important properties of the dynamical creation of a macroscopic superposition state in the system. To create a perfect equal superposition of left and right of the pendulum one has to prepare exactly at the unstable fixed point. However, a slight variation of this preparation still leads to superposition, though unequal. The typical size of the variation allowed to still prepare a sizable superposition is thereby given by the initial uncertainty in the wave function.

In our system this uncertainty is given by the size of the initial coherent spin state which one has to compare to the experimental imperfections discussed in section 3.8. These imperfections will degrade the final superposition state to a mixed state. As has been discussed before some of the effects such as decoherence due to atom loss are theoretically challenging to treat. In the following we will therefore restrict the discussion to the effects which can be estimated more easily.

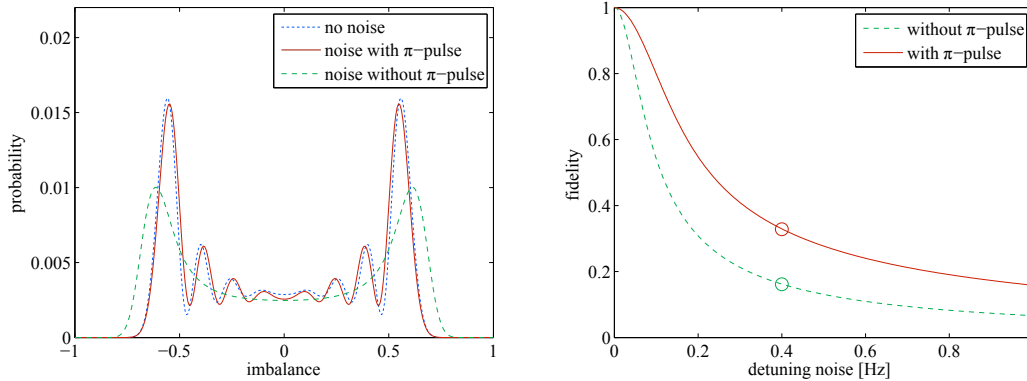


**Figure 5.11:** (left) Numerically simulated probability distribution of the imbalance in  $z$ -direction for 300 atoms. The blue dotted line shows the distribution expected after a perfect evolution. The other two lines correspond to the experimentally relevant case where the detuning is subject to noise on the order of 0.4 Hz from realization to realization. The green dotted line shows the total loss of the interference fringes due to this noise in the case where no echo pulse is applied. The red solid line shows how the application of an echo pulse restores the interference fringes although the evolution is subject to the same noise. (right) This is also shown by the fidelity of the final density operator and pure state after a perfect evolution. With increasing detuning noise the evolution with echo pulse (red) and without echo pulse (green dotted) deviate from a perfect overlap. However the decrease is much slower in the case of the echo pulse. At the typical scale of the detuning noise found in the experiment (circles) the fidelity is about twice as high as without the use of the echo technique. For simplicity this simulation neglects the nonlinearity during the echo pulse. However, the effect of this nonlinearity is very small compared to the effect of the detuning noise.

### 5.5.1 Detuning Noise and Spin Echo

Every offset in the initial preparation or the detuning breaks the symmetry of the dynamics with respect to the equator of the sphere and therefore to the imbalance. The generated superposition state will be more or less imbalanced up or down.

While the preparation is very accurate the effect of the detuning on the time evolution is significant. As discussed in section 3.8.2 the noise in the detuning stems from the fluctuations in the magnetic field and is approximately 0.4 Hz from realization to realization. because of this detuning noise the interference fringes in the probability distribution vanish as can be seen in figure 5.11. However, since the fluctuation affects mainly the low frequency magnetic fields causing fluctuations of the detuning from shot to shot the technique of spin echo can be used to reduce this effect significantly.

The spin echo technique is based on the application of a fast coupling pulse, causing a rotation by  $\pi$ , in the middle of the time evolution [98, 99]. This  $\pi$ -pulse or echo-pulse leads to an inversion of the state at the rotation axis of the pulse. A phase offset caused by a constant detuning during the first half of the evolution is inverted by the pulse and compensated during the second half of the evolution by

the detuning itself. This leads to the state ending up exactly at the phase of the coupling pulse independent of the constant detuning. The technique is used in many nuclear magnetic resonance experiments [33] and finds application in many forms of Ramsey type interferometry [100].

In our case where the dynamics during the evolution is determined by a combination of linear and nonlinear terms the usefulness of the echo sequence is not obvious. Here the phase of the echo pulse is the same as for the coupling during the time evolution. During the pulse the system is switched to the Rabi regime. Although a small nonlinear interaction is still present its influence during the short  $\pi$ -pulse is very small. The result is shown in figure 5.11. The left panel compares the probability distribution of an exemplary superposition state after a perfect evolution without noise to the experimental results, including the noise found in the experiment, with and without the use of the echo technique. Due to this noise the fringes in the atom number distribution disappear completely in the case where no echo pulse is applied. In contrast, the application of the echo pulse almost completely recovers the structure of the probability distribution found in the ideal case.

This recovery of the properties of the ideal evolution can be quantified by the fidelity  $F$  between the state in the ideal case  $|\text{ideal}\rangle$  and the density matrix  $\hat{\rho}_{\text{noise}}$  including the experimental noise, that is defined as

$$F = \langle \text{ideal} | \hat{\rho}_{\text{noise}} | \text{ideal} \rangle. \quad (5.13)$$

The right panel in figure 5.11 shows the fidelity for different detuning noise in the case with and without the application of the echo pulse during the evolution. The echo case shows overall a much higher fidelity to the aspired superposition state as expected from the results shown in the right panel. This result is the reason for using the echo technique throughout the measurements on the quantum mechanical behavior of the system presented in this work.

### 5.5.2 The Influence of Atom Loss

As discussed in section 3.8.1 atoms are lost during the time evolution. Besides the decoherence effects associated with this loss, it has several effects on the dynamics of the system. The system parameter  $\Lambda$  is directly related to the number of atoms in the systems (equation 2.23). The parameter  $\Lambda$  determines the strength of the nonlinear term in the Hamiltonian relative to the linear coupling. The dependence of  $\Lambda$  on the total atom number  $N$  in the system can be understood from the fact that the eigenvalues of the nonlinear term grow quadratically in contrast to the linear grow of the eigenvalues of the coupling term. However the number dependence of  $\Lambda$  is complicated by the atom number dependence of the nonlinear parameter  $\chi$ . As given in equation 2.13  $\chi$  depends on the spatial modes. Although the relative atom number in the two modes has only a small effect on the wave function (see section 3.6) their shape depends on the total atom number. Gross-Pitaevskiĭ simulations show that the dependency of  $\chi$  on the total atom number  $N$  is for our experimental parameters roughly given by  $\chi \propto \frac{1}{\sqrt{N}}$  leading to a dependence of  $\Lambda \propto \sqrt{N}$ .

While the decay of  $\Lambda$  with the total atom number is generally not a problem for the dynamical generation of a macroscopic superposition state, the statistical nature of the loss process and the strong dependence of the dynamics on the atom

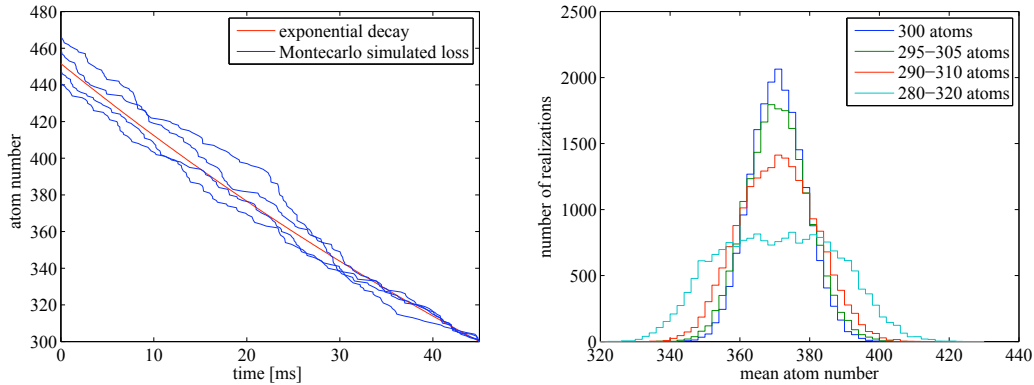


**Figure 5.12:** Examples of Monte Carlo simulations of the atom number decay during the typical time scale of 45 ms leading all to the same final atom number of 300 (blue). The expectation value of the atom number is shown in red revealing the significant deviation of the simulated traces. These fluctuations in the atom number during the time evolution lead to noise in the effective nonlinearity. (right) Fluctuations in the temporal mean of the atom number due to the statistical nature of the atom loss process. The different histograms show the temporal mean atom number of 21000 Monte Carlo simulations for different ranges of post selected atom numbers. Up to range a of  $\pm 10$  atoms the statistical effects dominate over the effect of the choice of the post selection range translating into an effective nonlinearity noise of about 2%.

number pose some difficulties. While the expectation value of the atom number in an ensemble of atoms that is affected by loss typically decreases with a given functional dependence the true atom number at a given time can be significantly different. This is shown in the left panel of figure 5.12. The decay of the expectation value of atoms, that is considered to be exponential, is shown in red. The blue lines are examples of Monte Carlo simulations of a decay processes leading to the same final atom number<sup>4</sup> of 300. The lines show a significant deviation from the expectation value. The restriction to end up at the same atom number is very close to our experimental situation where we post select the data depending on the final atom number. To gain enough statistics the range of selected atom numbers is typically on the order of  $\pm 10$  atoms around the aspired value. The right panel of the figure shows how the temporal mean of the atom number is distributed due to the fluctuation and due to the post selection range. The histograms show the distribution of Monte Carlo simulation results. For small ranges of the post selected atom numbers the fluctuation dominate the spread of the temporal mean. For our post selection the expected relative fluctuations are in the order of 2-3%.

The effect of the fluctuations of the nonlinearity are shown in figure 5.13. The theoretical probability distributions expected after a time evolution of 45 ms are shown with and without including noise. In the case of the experimentally realistic noise of 2%, the interference fringes have completely vanished. This simulation shows that, in order to detect the macroscopic interference which is expected for

<sup>4</sup>The simulation is actually performed in reversed time.

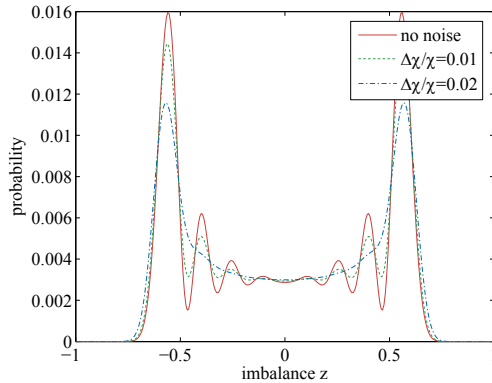


**Figure 5.13:** Smearing of the interference pattern due to fluctuations in the nonlinearity  $\chi$  caused by atom loss. The simulated curves show the expected probability distribution after an evolution time of 45 ms for typical parameters found in the experiment. Plotted are the distributions for the case of a perfect evolution with no noise in the nonlinearity  $\chi$  (red solid line) and with including relative noise in  $\chi$  of 1% (green dotted line) and 2% (blue dash-dotted line). The interference fringes completely disappear in the case of the high relative noise.

the superposition state, one has to reduce the noise in the nonlinearity originating from atom loss. A possible way of reducing this noise is a better initial preparation of the BEC in terms of atom number fluctuation. If one would have a more deterministic atom number in the beginning of the time evolution, the effective noise could be eventually reduced so that the interference becomes visible in the measured histograms.

## 5.6 Numerical Simulation

In this section we will briefly discuss how the numerical simulations found throughout the discussion of the quantum mechanical aspect were performed and how the experimental imperfections are included. In general the Hamiltonian of the system (see equation 2.12), can be solved by numerical diagonalization of the Hamiltonian in the number state basis. This method is very fast even for relatively large atom numbers, since the Hamiltonian is tridiagonal. Once the Hamiltonian is diagonalized the method allows to calculate the state at an arbitrary time, by simple integration of the Schrödinger equation. However, this method does not easily allow to implement the time dependence of the system parameters. This time dependence has turned out to be crucial to get a good agreement between the measured results and the simulations. The time dependence in the parameters has two origins. The loss of atoms leads to a decay of the effective nonlinearity  $N\chi$  and a change in the detuning due to the atom number dependent last term in equation 2.14. Furthermore, the magnetic field at the position of the atoms is time dependent due to the residual 50 Hz signal from the mains supply, causing an additional time dependence of the detuning.

To implement these time dependent terms in the simulations we numerically

integrate the time dependent Schrödinger equation. This is computationally much more time-consuming than the single diagonalization method. However, for our particle numbers the results can still be gained within a feasible time on a normal personal computer. It is important to mention that this method does not allow to include the real effects of the atom loss, which would imply the use of all the different sized Hilbert spaces. Our simulations are performed in a Hilbert space with fixed size<sup>5</sup>, but include only the effective mechanisms of the atom loss on the system parameters.

The time dependence of the parameters in the simulation is chosen according to the results gained in independent measurements. This allows us to simulate our findings without free parameters or any fitting.

To include the noise contributions due to magnetic field fluctuations and fluctuations of the effective atom number (see section 5.5) we perform simulations for a whole set of parameters. The gained results are afterwards incoherently added to a density matrix, according to the size of the respective fluctuations found in the experiment.

---

<sup>5</sup>The size of the Hilbert space is typically chosen according to the final atom number in the experiment



# Chapter 6

## Summary of the Results and Outlook

In the course of this work we have realized an internal bosonic Josephson junction and investigated its dynamical behavior.

We were able to characterize the theoretically predicted classical mean field behavior in all its dynamical aspects. The realization with internal spin degrees of freedom allows a much higher level of control of the initial preparation as compared to previous work [55, 56]. Furthermore the readout of the phase, which is done by adapted coupling pulses, can be performed with higher precision. This allows us to map out the dynamical behavior in the full phase space with high accuracy, revealing previously inaccessible dynamical behavior such as  $\pi$ -oscillations. The internal bosonic Josephson junction further allows to investigate a parameter regime where the classical dynamics undergo a bifurcation. This allows to experimentally reveal the underlying topological change in the dynamics. Furthermore, this investigation shows the fundamentally different topology of the dynamics found in the bosonic Josephson junction compared to the common Josephson effect found in superconductors. The results on the classical behavior of the internal Josephson junction have been published in [53].

The quantum dynamics of the internal Josephson junction were studied at the particularly interesting unstable fixed point in the Josephson regime. We have systematically investigated how the many-body dynamics lead to spin squeezing and entanglement in the system on short time scales. Compared to the one-axis twisting scheme [23], this novel dynamical generation of squeezing has the advantage that very high possible gain in interferometric measurements is reached on shot time scales, indicated by the quantum Fisher information.

Furthermore, we demonstrate that the squeezing disappears on longer timescales. Our theoretical simulations show that this effect can be assigned to the expected quantum mechanical behavior and is not due to decoherence or noise in the preparation or dynamical evolution. The good qualitative agreement of the theoretical simulations with the measured data for longer times further suggests that a macroscopic superposition is generated in the course of the dynamics, although we are not yet able to quantify the degree of coherence present in the system. The possibility to perform tomographic analysis of the many particle state allows us to reconstruct its Wigner function. We have demonstrated this reconstruction via filtered back projection and with the use of a iterative maximum likelihood estimation algorithm of the state's density matrix. The large number of measurements performed on the

---

system indicates that an accurate estimation of the macroscopic many particle state is within reach. Future improvement in terms of the discussed experimental limitations will likely allow to show the macroscopic superposition character of the state either by the expected interference or by its quantum Fisher information. The results gained on the squeezing and the tomographic reconstruction will be published in the near future.

We have demonstrated that the realization of the internal bosonic Josephson junction, provides a testbed for the study of quantum classical correspondence and many-particle quantum dynamics.

The high degree of controllability of the system opens up a route to study the system under the influence of an additional driving. It is expected that the classical phase space in this case exhibits chaotic regions which lack a quantum counterpart. Quantum dynamics in the presence of chaos in the classical system give rise to chaos assisted tunneling [101] and related phenomena [102], which become accessible in the bosonic Josephson junction. The possibility to change the system size and hereby the classicality of the system further enables the investigation of the transition from classical chaos to quantum mechanical entanglement [103].

The quantum mechanical behavior at the classical unstable fixed point allows for the generation of strongly entangled many-particle states. The results gained in this direction in this work suggest that experimental evidence of the superposition character of the generated states is within reach. This may allow to use the high possible gain in interferometric precision of these states in atom interferometers such as atomic clocks which are currently limited to the standard quantum limit [104].

The possibility to analyze the quantum states by means of tomography in arbitrary directions allows to reconstruct the density matrix of the state. This might allow to study microscopic decoherence effects in highly entangled macroscopic quantum states. Furthermore, the scalability of the system might show how far the *size of the quantum world* can be pushed.

## Appendix A

### Histograms of the Squeezing Measurements



## Appendix B

### Full Data Entering the Measured Wigner Functions

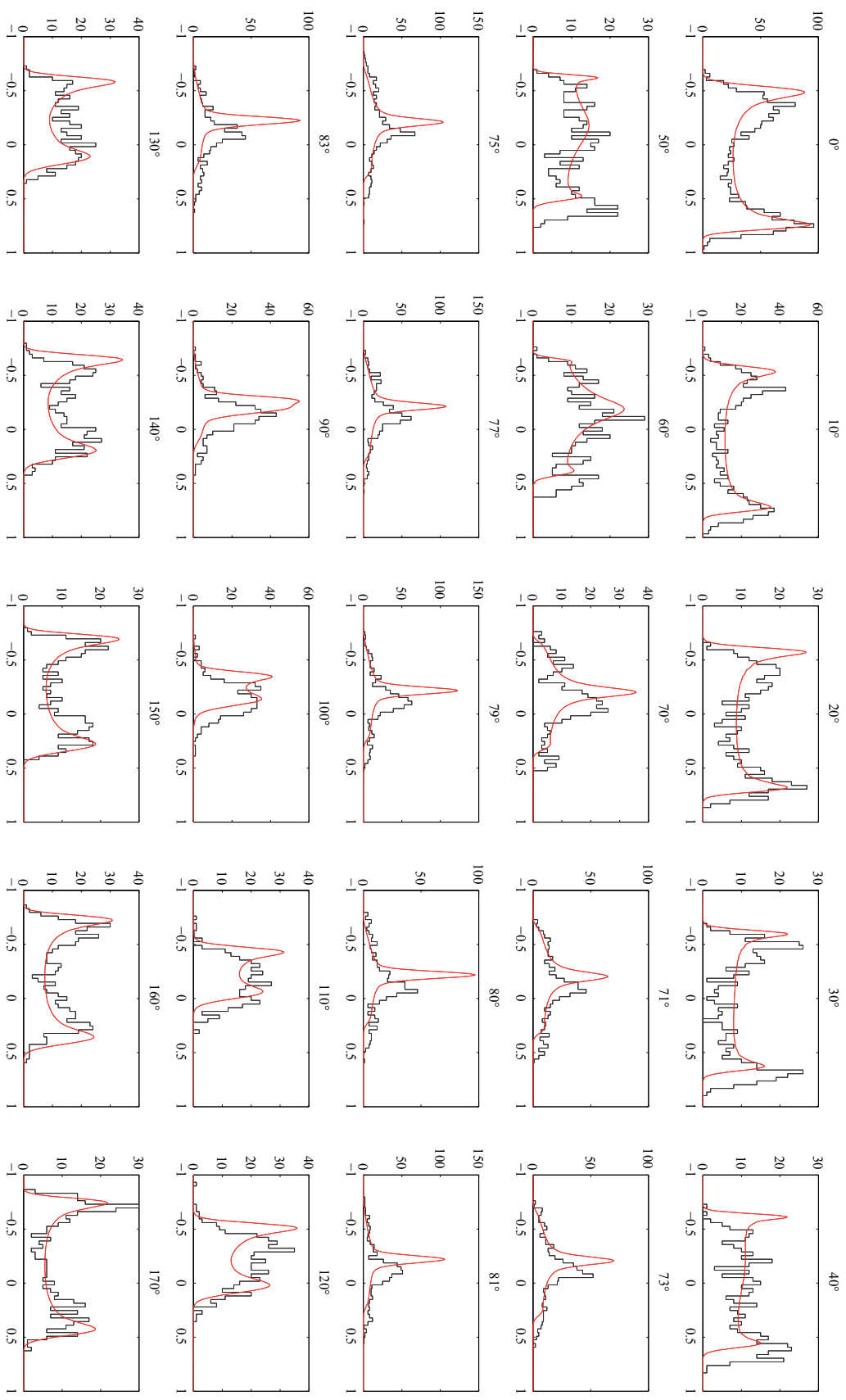


**Figure B.1:** Tomographic data gained for a final atom number ranging from 310-340 atoms after a time evolution of 45 ms. The coupling frequency is  $\Omega = 2\pi \times 21$  Hz. The respective measurement axis is indicated above the histograms. The red solid lines correspond to the numerical simulation without free parameters (see section 5.6). The total number of results is  $\sim 13000$ .

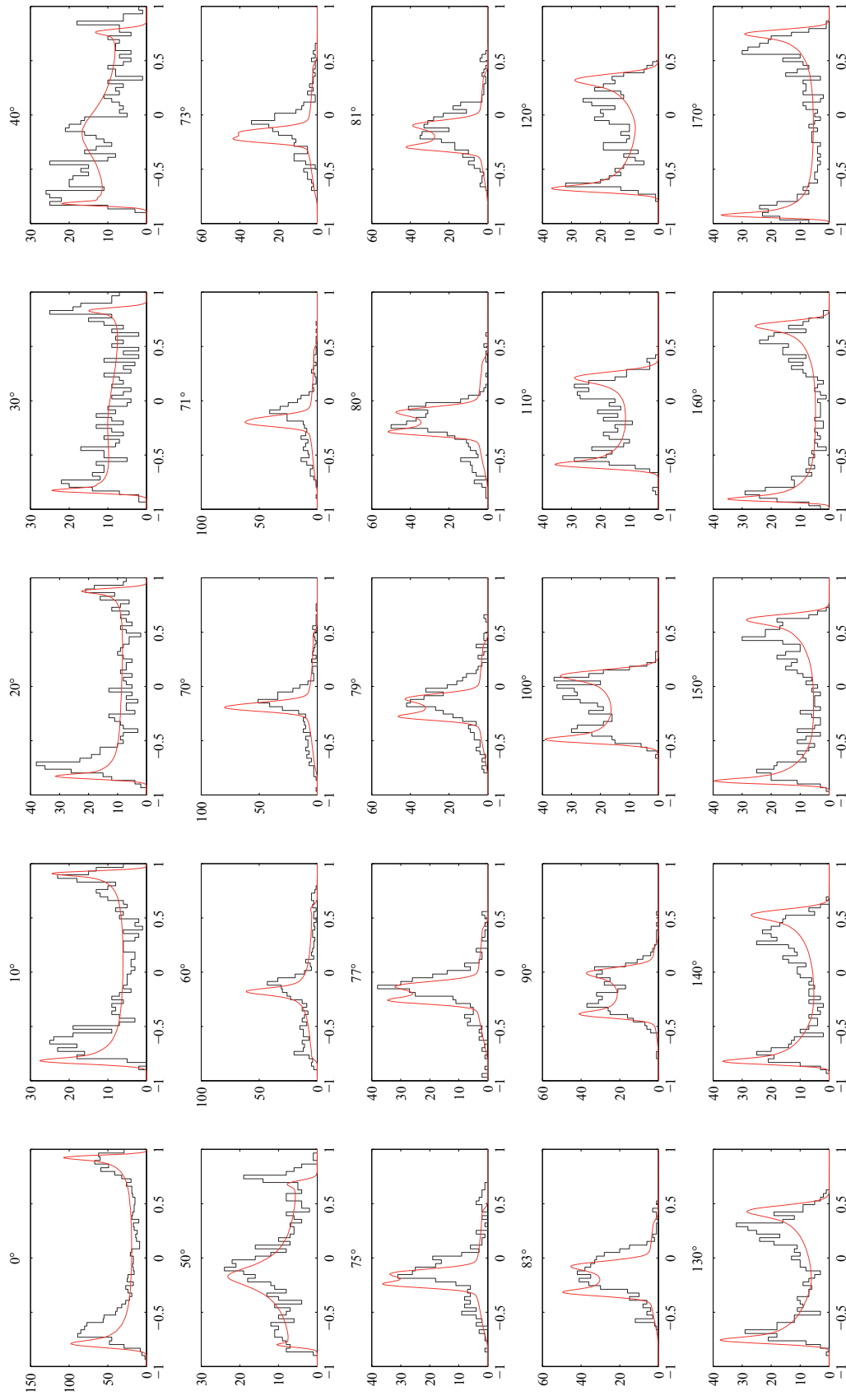


**Figure B.2:** Tomographic data gained for a final atom number ranging from 310-340 atoms after a time evolution of 45 ms. The coupling frequency is  $\Omega = 2\pi \times 16.7$  Hz. The respective measurement axis is indicated above the histograms. The red solid lines correspond to the numerical simulation without free parameters (see section 5.6). The total number of results is  $\sim 13000$ .



# Bibliography

- [1] E. Schrödinger. Die gegenwärtige Situation in der Quantenmechanik. *Naturwissenschaften*, 23:807–812, 1935. 10.1007/BF01491891.
- [2] E. Schrödinger. Die gegenwärtige Situation in der Quantenmechanik. *Naturwissenschaften*, 23:823–828, 1935. 10.1007/BF01491914.
- [3] E. Schrödinger. Die gegenwärtige Situation in der Quantenmechanik. *Naturwissenschaften*, 23:844–849, 1935. 10.1007/BF01491987.
- [4] M. H. Anderson, J. R. Ensher, M. R. Matthews, C. E. Wieman, and E. A. Cornell. Observation of Bose-Einstein condensation in a dilute atomic vapor. *Science*, 269(5221):198–201, 1995.
- [5] L.P. Pitaevskiĭ and S. Stringari. *Bose-Einstein Condensation*. Clarendon Press, 2003.
- [6] D. M. Stamper-Kurn, M. R. Andrews, A. P. Chikkatur, S. Inouye, H.-J. Miesner, J. Stenger, and W. Ketterle. Optical confinement of a Bose-Einstein condensate. *Phys. Rev. Lett.*, 80:2027–2030, Mar 1998.
- [7] Cheng Chin, Rudolf Grimm, Paul Julienne, and Eite Tiesinga. Feshbach resonances in ultracold gases. *Rev. Mod. Phys.*, 82:1225–1286, Apr 2010.
- [8] Juha Javanainen. Oscillatory exchange of atoms between traps containing Bose condensates. *Phys. Rev. Lett.*, 57:3164–3166, Dec 1986.
- [9] Anthony J. Leggett. Bose-Einstein condensation in the alkali gases: Some fundamental concepts. *Rev. Mod. Phys.*, 73:307–356, Apr 2001.
- [10] H.J. Lipkin, N. Meshkov, and A.J. Glick. Validity of many-body approximation methods for a solvable model: (i). exact solutions and perturbation theory. *Nuclear Physics*, 62(2):188 – 198, 1965.
- [11] N. Meshkov, A.J. Glick, and H.J. Lipkin. Validity of many-body approximation methods for a solvable model: (ii). linearization procedures. *Nuclear Physics*, 62(2):199 – 210, 1965.
- [12] A.J. Glick, H.J. Lipkin, and N. Meshkov. Validity of many-body approximation methods for a solvable model: (iii). diagram summations. *Nuclear Physics*, 62(2):211 – 224, 1965.

- [13] S. Raghavan, A. Smerzi, S. Fantoni, and S. R. Shenoy. Coherent oscillations between two weakly coupled Bose-Einstein condensates: Josephson effects, -oscillations, and macroscopic quantum self-trapping. *Phys. Rev. A*, 59:620–633, Jan 1999.
- [14] A. Smerzi, S. Fantoni, S. Giovanazzi, and S. R. Shenoy. Quantum coherent atomic tunneling between two trapped Bose-Einstein condensates. *Phys. Rev. Lett.*, 79:4950–4953, Dec 1997.
- [15] D. Gordon and C. M. Savage. Creating macroscopic quantum superpositions with Bose-Einstein condensates. *Phys. Rev. A*, 59:4623–4629, Jun 1999.
- [16] J. I. Cirac, M. Lewenstein, K. Mølmer, and P. Zoller. Quantum superposition states of Bose-Einstein condensates. *Phys. Rev. A*, 57:1208–1218, Feb 1998.
- [17] M. J. Steel and M. J. Collett. Quantum state of two trapped Bose-Einstein condensates with a Josephson coupling. *Phys. Rev. A*, 57:2920–2930, Apr 1998.
- [18] L.C. Biedenharn and H. Van Dam. *Quantum theory of angular momentum: a collection of reprints and original papers*. Perspectives in physics. Academic Press, 1965.
- [19] J.J. Sakurai and S.F. Tuan. *Modern Quantum Mechanics*. Addison-Wesley Publishing Company, 1994.
- [20] F. T. Arecchi, Eric Courtens, Robert Gilmore, and Harry Thomas. Atomic coherent states in quantum optics. *Phys. Rev. A*, 6:2211–2237, Dec 1972.
- [21] Anton Chigurh. private communication.
- [22] L. Allen and J.H. Eberly. *Optical Resonance and Two-Level Atoms*. Dover Books on Physics. Dover, 1987.
- [23] Masahiro Kitagawa and Masahito Ueda. Squeezed spin states. *Phys. Rev. A*, 47:5138–5143, Jun 1993.
- [24] Max F. Riedel, Pascal Böhi, Yun Li, Theodor W. Hänsch, Alice Sinatra, and Philipp Treutlein. Atom-chip-based generation of entanglement for quantum metrology. *Nature*, 464(7292):1170–1173, April 2010.
- [25] C. Gross, T. Zibold, E. Nicklas, J. Estève, and M. K. Oberthaler. Non-linear atom interferometer surpasses classical precision limit. *Nature*, 464(7292):1165–1169, April 2010.
- [26] Bernd Eiermann. *Kohärente nichtlineare Materiewellendynamik - Helle atomare Solitonen*. PhD thesis, University of Konstanz, 2004.
- [27] Andreas Weller. *Dynamics and Interaction of Dark Solitons in Bose-Einstein Condensates*. PhD thesis, University of Heidelberg, 2009.

- 
- [28] Christian Gross. *Spin squeezing and non-linear atom interferometry with Bose-Einstein condensates*. PhD thesis, University of Heidelberg, 2010.
- [29] H.J. Metcalf and P. Van Der Straten. *Laser Cooling and Trapping*. Graduate Texts in Contemporary Physics. Springer, 1999.
- [30] Wolfgang Petrich, Michael H. Anderson, Jason R. Ensher, and Eric A. Cornell. Stable, tightly confining magnetic trap for evaporative cooling of neutral atoms. *Phys. Rev. Lett.*, 74:3352–3355, Apr 1995.
- [31] Jens Appmeier. Bose-Einstein condensates in a double well potential: A route to quantum interferometry. Master’s thesis, University of Heidelberg, 2007.
- [32] E. Nicklas, H. Strobel, T. Zibold, C. Gross, B. A. Malomed, P. G. Kevrekidis, and M. K. Oberthaler. Rabi flopping induces spatial demixing dynamics. *Phys. Rev. Lett.*, 107:193001, Nov 2011.
- [33] J. Keeler. *Understanding NMR Spectroscopy*. John Wiley & Sons, 2011.
- [34] Satoshi Tojo, Yoshihisa Taguchi, Yuta Masuyama, Taro Hayashi, Hiroki Saito, and Takuya Hirano. Controlling phase separation of binary Bose-Einstein condensates via mixed-spin-channel feshbach resonance. *Phys. Rev. A*, 82:033609, Sep 2010.
- [35] Thorsten Köhler, Krzysztof Góral, and Paul S. Julienne. Production of cold molecules via magnetically tunable feshbach resonances. *Rev. Mod. Phys.*, 78:1311–1361, Dec 2006.
- [36] Artur Widera, Olaf Mandel, Markus Greiner, Susanne Kreim, Theodor W. Hänsch, and Immanuel Bloch. Entanglement interferometry for precision measurement of atomic scattering properties. *Phys. Rev. Lett.*, 92:160406, Apr 2004.
- [37] M. Erhard, H. Schmaljohann, J. Kronjäger, K. Bongs, and K. Sengstock. Measurement of a mixed-spin-channel feshbach resonance in  $^{87}\text{Rb}$ . *Phys. Rev. A*, 69:032705, Mar 2004.
- [38] Kaspar Sakmann, Alexej I. Streltsov, Ofir E. Alon, and Lorenz S. Cederbaum. Exact quantum dynamics of a bosonic Josephson junction. *Phys. Rev. Lett.*, 103:220601, Nov 2009.
- [39] Kaspar Sakmann. Exact quantum dynamics of a bosonic Josephson junction. In *Many-Body Schrödinger Dynamics of Bose-Einstein Condensates*, Springer Theses, pages 65–80. Springer Berlin Heidelberg, 2011.
- [40] G. Reinaudi, T. Lahaye, Z. Wang, and D. Guéry-Odelin. Strong saturation absorption imaging of dense clouds of ultracold atoms. *Opt. Lett.*, 32(21):3143–3145, Nov 2007.
- [41] M. R. Andrews, M.-O. Mewes, N. J. van Druten, D. S. Durfee, D. M. Kurn, and W. Ketterle. Direct, nondestructive observation of a Bose condensate. *Science*, 273(5271):84–87, 1996.

- [42] Tatjana Gericke, Peter Wurtz, Daniel Reitz, Tim Langen, and Herwig Ott. High-resolution scanning electron microscopy of an ultracold quantum gas. *Nat Phys*, 4(12):949–953, December 2008.
- [43] Timo Ottenstein. A new objective for high resolution imaging of Bose-Einstein condensates. Master’s thesis, University of Heidelberg, 2006.
- [44] Yun Li, Y. Castin, and A. Sinatra. Optimum spin squeezing in Bose-Einstein condensates with particle losses. *Phys. Rev. Lett.*, 100:210401, May 2008.
- [45] A. Micheli, D. Jaksch, J. I. Cirac, and P. Zoller. Many-particle entanglement in two-component Bose-Einstein condensates. *Phys. Rev. A*, 67:013607, Jan 2003.
- [46] C. J. Dedman, R. G. Dall, L. J. Byron, and A. G. Truscott. Active cancellation of stray magnetic fields in a Bose-Einstein condensation experiment. *Review of Scientific Instruments*, 78(2):024703, 2007.
- [47] Norman F. Ramsey. A molecular beam resonance method with separated oscillating fields. *Phys. Rev.*, 78:695–699, Jun 1950.
- [48] B.D. Josephson. Possible new effects in superconductive tunnelling. *Physics Letters*, 1(7):251 – 253, 1962.
- [49] J. M. Rowell, P. W. Anderson, and D. E. Thomas. Image of the phonon spectrum in the tunneling characteristic between superconductors. *Phys. Rev. Lett.*, 10:334–336, Apr 1963.
- [50] A. Barone and G. Paternò. *Physics and applications of the Josephson effect*. UMI books on demand. Wiley, 1982.
- [51] S. V. Pereverzev, A. Loshak, S. Backhaus, J. C. Davis, and R. E. Packard. Quantum oscillations between two weakly coupled reservoirs of superfluid  $^3\text{He}$ . *Nature*, 388(6641):449–451, July 1997.
- [52] Kalyani Sukhatme, Yury Mukharsky, Talso Chui, and David Pearson. Observation of the ideal Josephson effect in superfluid  $^4\text{He}$ . *Nature*, 411(6835):280–283, May 2001.
- [53] Tilman Zibold, Eike Nicklas, Christian Gross, and Markus K. Oberthaler. Classical bifurcation at the transition from rabi to Josephson dynamics. *Phys. Rev. Lett.*, 105:204101, Nov 2010.
- [54] F. S. Cataliotti, S. Burger, C. Fort, P. Maddaloni, F. Minardi, A. Trombettoni, A. Smerzi, and M. Inguscio. Josephson junction arrays with Bose-Einstein condensates. *Science*, 293(5531):843–846, 2001.
- [55] Michael Albiez, Rudolf Gati, Jonas Fölling, Stefan Hunsmann, Matteo Cristiani, and Markus K. Oberthaler. Direct observation of tunneling and non-linear self-trapping in a single bosonic Josephson junction. *Phys. Rev. Lett.*, 95:010402, Jun 2005.

- 
- [56] S. Levy, E. Lahoud, I. Shomroni, and J. Steinhauer. The a.c. and d.c. Josephson effects in a Bose-Einstein condensate. *Nature*, 449(7162):579–583, October 2007.
- [57] Yvan Castin and Jean Dalibard. Relative phase of two Bose-Einstein condensates. *Phys. Rev. A*, 55:4330–4337, Jun 1997.
- [58] Maya Chuchem, Katrina Smith-Mannschott, Moritz Hiller, Tsampikos Kottos, Amichay Vardi, and Doron Cohen. Quantum dynamics in the bosonic Josephson junction. *Phys. Rev. A*, 82:053617, Nov 2010.
- [59] Q. Xie and W. Hai. Quantum entanglement and classical bifurcations in a coupled two-component Bose-Einstein condensate. *The European Physical Journal D - Atomic, Molecular, Optical and Plasma Physics*, 39:277–282, 2006. 10.1140/epjd/e2006-00103-6.
- [60] Julien Vidal, Guillaume Palacios, and Claude Aslangul. Entanglement dynamics in the lipkin-meshkov-glick model. *Phys. Rev. A*, 70:062304, Dec 2004.
- [61] B. Juliá-Díaz, J. Martorell, and A. Polls. Bose-Einstein condensates on slightly asymmetric double-well potentials. *Phys. Rev. A*, 81:063625, Jun 2010.
- [62] B. Juliá-Díaz, D. Dagnino, M. Lewenstein, J. Martorell, and A. Polls. Macroscopic self-trapping in Bose-Einstein condensates: Analysis of a dynamical quantum phase transition. *Phys. Rev. A*, 81:023615, Feb 2010.
- [63] B. Yurke and D. Stoler. Generating quantum mechanical superpositions of macroscopically distinguishable states via amplitude dispersion. *Phys. Rev. Lett.*, 57:13–16, Jul 1986.
- [64] D.F. Walls and G.J. Milburn. *Quantum Optics*. Springer, 2008.
- [65] D. J. Wineland, J. J. Bollinger, W. M. Itano, F. L. Moore, and D. J. Heinzen. Spin squeezing and reduced quantum noise in spectroscopy. *Phys. Rev. A*, 46:R6797–R6800, Dec 1992.
- [66] Norman F. Ramsey. Experiments with separated oscillatory fields and hydrogen masers. *Science*, 248(4963):1612–1619, 1990.
- [67] W. M. Itano, J. C. Bergquist, J. J. Bollinger, J. M. Gilligan, D. J. Heinzen, F. L. Moore, M. G. Raizen, and D. J. Wineland. Quantum projection noise: Population fluctuations in two-level systems. *Phys. Rev. A*, 47:3554–3570, May 1993.
- [68] W. M. Itano, J. C. Bergquist, J. J. Bollinger, J. M. Gilligan, D. J. Heinzen, F. L. Moore, M. G. Raizen, and D. J. Wineland. Erratum: Quantum projection noise: Population fluctuations in two-level systems [phys. rev. a 47 , 3554 (1993)]. *Phys. Rev. A*, 51:1717–1717, Feb 1995.
- [69] A. Sorensen, L.-M. Duan, J. I. Cirac, and P. Zoller. Many-particle entanglement with Bose-Einstein condensates. *Nature*, 409(6816):63–66, January 2001.

- [70] Géza Tóth, Christian Knapp, Otfried Gühne, and Hans J. Briegel. Optimal spin squeezing inequalities detect bound entanglement in spin models. *Phys. Rev. Lett.*, 99:250405, Dec 2007.
- [71] Géza Tóth, Christian Knapp, Otfried Gühne, and Hans J. Briegel. Spin squeezing and entanglement. *Phys. Rev. A*, 79:042334, Apr 2009.
- [72] C.W. Helstrom. Minimum mean-squared error of estimates in quantum statistics. *Physics Letters A*, 25(2):101 – 102, 1967.
- [73] Samuel L. Braunstein and Carlton M. Caves. Statistical distance and the geometry of quantum states. *Phys. Rev. Lett.*, 72:3439–3443, May 1994.
- [74] John W. Pratt. F. y. edgeworth and r. a. fisher on the efficiency of maximum likelihood estimation. *The Annals of Statistics*, 4(3):pp. 501–514, 1976.
- [75] Philipp Hyllus, Otfried Gühne, and Augusto Smerzi. Not all pure entangled states are useful for sub-shot-noise interferometry. *Phys. Rev. A*, 82:012337, Jul 2010.
- [76] Harald Cramér. *Mathematical methods of statistics*. Princeton University Press, Princeton, 1999.
- [77] Roland Krischek, Christian Schwemmer, Witlef Wieczorek, Harald Weinfurter, Philipp Hyllus, Luca Pezzé, and Augusto Smerzi. Useful multiparticle entanglement and sub-shot-noise sensitivity in experimental phase estimation. *Phys. Rev. Lett.*, 107:080504, Aug 2011.
- [78] Luca Pezzé and Augusto Smerzi. Entanglement, nonlinear dynamics, and the heisenberg limit. *Phys. Rev. Lett.*, 102:100401, Mar 2009.
- [79] Kenneth Maussang, G. Edward Marti, Tobias Schneider, Philipp Treutlein, Yun Li, Alice Sinatra, Romain Long, Jérôme Estève, and Jakob Reichel. Enhanced and reduced atom number fluctuations in a BEC splitter. *Phys. Rev. Lett.*, 105:080403, Aug 2010.
- [80] E. Wigner. On the quantum correction for thermodynamic equilibrium. *Phys. Rev.*, 40:749–759, Jun 1932.
- [81] Marlan O. Scully. How to make quantum mechanics look like a hidden-variable theory and vice versa. *Phys. Rev. D*, 28:2477–2484, Nov 1983.
- [82] Leon Cohen and Marlan Scully. Joint Wigner distribution for spin-1/2 particles. *Foundations of Physics*, 16:295–310, 1986. 10.1007/BF01882690.
- [83] G. S. Agarwal. Relation between atomic coherent-state representation, state multipoles, and generalized phase-space distributions. *Phys. Rev. A*, 24:2889–2896, Dec 1981.
- [84] Jonathan P. Dowling, G. S. Agarwal, and Wolfgang P. Schleich. Wigner distribution of a general angular-momentum state: Applications to a collection of two-level atoms. *Phys. Rev. A*, 49:4101–4109, May 1994.

- 
- [85] U. Fano. Geometrical characterization of nuclear states and the theory of angular correlations. *Phys. Rev.*, 90:577–579, May 1953.
- [86] Klaus Schulten and Roy G. Gordon. Exact recursive evaluation of 3j- and 6j-coefficients for quantum-mechanical coupling of angular momenta. *Journal of Mathematical Physics*, 16(10):1961–1970, 1975.
- [87] Roman Schmied and Philipp Treutlein. Tomographic reconstruction of the Wigner function on the Bloch sphere. *New Journal of Physics*, 13(6):065019, 2011.
- [88] D. T. Smithey, M. Beck, M. G. Raymer, and A. Faridani. Measurement of the Wigner distribution and the density matrix of a light mode using optical homodyne tomography: Application to squeezed states and the vacuum. *Phys. Rev. Lett.*, 70:1244–1247, Mar 1993.
- [89] G. Breitenbach, S. Schiller, and J. Mlynek. Measurement of the quantum states of squeezed light. *Nature*, 387(6632):471–475, May 1997.
- [90] W. H. Oldendorf. Isolated flying spot detection of radiodensity discontinuities displaying the internal structural pattern of a complex object. *Bio-Medical Electronics, IRE Transactions on*, 8(1):68–72, Jan. 1961.
- [91] K. Banaszek, G. M. D’Ariano, M. G. A. Paris, and M. F. Sacchi. Maximum-likelihood estimation of the density matrix. *Phys. Rev. A*, 61:010304, Dec 1999.
- [92] G. Mauro D’Ariano, Martina De Laurentis, Matteo G. A. Paris, Alberto Porzio, and Salvatore Solimeno. Quantum tomography as a tool for the characterization of optical devices. *Journal of Optics B: Quantum and Semiclassical Optics*, 4(3):S127, 2002.
- [93] T. J. Dunn, I. A. Walmsley, and S. Mukamel. Experimental determination of the quantum-mechanical state of a molecular vibrational mode using fluorescence tomography. *Phys. Rev. Lett.*, 74:884–887, Feb 1995.
- [94] D. Leibfried, D. M. Meekhof, B. E. King, C. Monroe, W. M. Itano, and D. J. Wineland. Experimental determination of the motional quantum state of a trapped atom. *Phys. Rev. Lett.*, 77:4281–4285, Nov 1996.
- [95] Ch. Kurtsiefer, T. Pfau, and J. Mlynek. Measurement of the Wigner function of an ensemble of helium atoms. *Nature*, 386(6621):150–153, March 1997.
- [96] A. I. Lvovsky. Iterative maximum-likelihood reconstruction in quantum homodyne tomography. *Journal of Optics B: Quantum and Semiclassical Optics*, 6(6):S556, 2004.
- [97] Jaroslav Řeháček, Zdeněk Hradil, E. Knill, and A. I. Lvovsky. Diluted maximum-likelihood algorithm for quantum tomography. *Phys. Rev. A*, 75:042108, Apr 2007.

- [98] E. L. Hahn. Spin echoes. *Phys. Rev.*, 80:580–594, Nov 1950.
- [99] H. Y. Carr and E. M. Purcell. Effects of diffusion on free precession in nuclear magnetic resonance experiments. *Phys. Rev.*, 94:630–638, May 1954.
- [100] N. A. Kurnit, I. D. Abella, and S. R. Hartmann. Observation of a photon echo. *Phys. Rev. Lett.*, 13:567–568, Nov 1964.
- [101] Steven Tomsovic and Denis Ullmo. Chaos-assisted tunneling. *Phys. Rev. E*, 50:145–162, Jul 1994.
- [102] Tharanga Jinasundera, Christoph Weiss, and Martin Holthaus. Many-particle tunnelling in a driven bosonic Josephson junction. *Chemical Physics*, 322(12):118 – 126, 2006.
- [103] Shohini Ghose, Rene Stock, Poul Jessen, Roshan Lal, and Andrew Silberfarb. Chaos, entanglement, and decoherence in the quantum kicked top. *Phys. Rev. A*, 78:042318, Oct 2008.
- [104] Vittorio Giovannetti, Seth Lloyd, and Lorenzo Maccone. Quantum-enhanced measurements: Beating the standard quantum limit. *Science*, 306(5700):1330–1336, 2004.

# Danksagung / Acknowledgments

- Vielen Dank meinem Betreuer Markus Oberthaler, der mich zuerst als Diplomand und später als Doktorand in seine Arbeitsgruppe aufgenommen hat. Die Verantwortung, die er mir übertrug, gepaart mit dem großen Vertrauen das er mir entgegen gebracht hat, habe ich sehr geschätzt. Sein großes Interesse an den experimentellen Fortschritten sowie sein gutes Zureden und seine optimistische Art auch in schwierigeren Phasen meiner Arbeit waren für mich immer ein großer Ansporn. Nicht zuletzt seiner Person ist das äußerst gute Klima in der Arbeitsgruppe zu verdanken.
- Sehr herzlich möchte ich mich bei Helmut Strobel bedanken, dessen Arbeitseinstellung und Begeisterung für die Physik an sich, mir stets imponiert haben. Die viele Zeit, die wir in den letzten Jahren zusammen verbrachten, wird mir immer in guter Erinnerung bleiben. Dazu zählt auch das äußerst interessante Singwochenende, obwohl mir mit meinem unterdurchschnittlichen Bariton eine Gesangskarriere verwehrt bleiben wird. Dass mir Helmut so manches Mal unfreiwillig den Schlaf geraubt hat, werde ich ihm gerne verzeihen, da er dann immer einen guten Tipp für die Physik auf Lager hatte.
- Ein großer Dank geht an Wolfgang Müssel, der als Doktorand maßgeblich zu den Experimenten beigetragen hat. Seine uneingeschränkte Unterstützung hat mich immer motiviert weiterzumachen, auch wenn es manchmal aussichtslos erschien. Seine breitgefächerten Interessen sorgten außerdem immer für großartige Unterhaltung im Labor oder beim Kaffee. Ich hoffe, spätestens seit der Zeit im Wallis gehört auch Skifahren dazu.
- Eike Nicklas danke ich für seine faire Art und die vielen lustigen gemeinsamen Stunden in und besonders außerhalb des Labors. Sein Einsatz wird mir, nicht nur was Weihnachtsfeiern, Rodeln, Après-Ski oder Döner Kebap betrifft, besonders in Erinnerung bleiben.
- Christian Groß möchte ich für die schöne gemeinsame Zeit am BEC-Experiment danken. Unsere Diskussionen über die Physik, die beiderseits sehr engagiert geführt wurden, haben mich oft überzeugt und dazu beigetragen, einen Schritt im Experiment vorwärts zu kommen.
- I want to thank Jerome Estève who was a very inspiring instructor and he taught me a lot about cold atoms and electronics in the beginning of my time in the group. His nice character and his spot on explanations were always much-admired.

- Tobias Schuster möchte ich für die netten 'spontanen' Grillabende und sein offenes Ohr für Alles danken. Sein Rat, das Orchester zu wechseln, hat sich nicht nur in Bezug auf die schöne gemeinsame Zeit als sehr wichtig herausgestellt.
- Jiří Tomkovič danke ich für die vielen intensiven Diskussionen, insbesondere über politische Themen, die ich stets sehr genossen habe. Er hat mir dabei mehr als einmal die Augen geöffnet, auch wenn es mir schwerfiel, das immer zuzugeben.
- Bei David Hume möchte ich mich für seine ausgesprochen nette Art bedanken. Seine Fähigkeit sich, nicht nur sprachlich, in die Gruppe zu integrieren habe ich besonders bewundert, - auch seine große Geduld, die neutralen Atome zu bändigen!
- Many thanks to Bruno Juliá-Díaz for his ongoing interest in the experimental progress, the discussions about Josephson physics and his patience concerning my email replies.
- Bei Jürgen Schölles bedanke ich mich für die ausdauernde Unterstützung bei elektronischen Problemen und besonders für die neue Sichtweise, die ich durch seine Yoga Anleitung erhalten habe.
- Prof. Thomas Gasenzer danke ich für seine spontane Bereitschaft die Arbeit als Gutachter zu betreuen.
- Ich danke Andreas Weller, Jens Appmeier, Jens-Philipp Ronzheimer, Hendrik-Marten Meyer, Rostislav Doganov, Ion Stroescu, Naida Dzigal, Daniel Linne-mann, Markus Berberich, Elisabeth Brühl, Simon Murmann und Moritz Höfer, die während meiner Zeit am BEC-Experiment oder 'spin-offs' mitgearbeitet haben, und so einen großen Anteil an dem Erfolg der Experimente haben.
- Dankeschön auch an die Team Assistants Dagmar Hufnagel und Christiane Jäger die immer ein offenes Ohr nicht nur für die bürokratischen Hürden des Alltags hatten. Die Geduld mit der sie auf so manches Timesheet gewartet haben, erlaubte mir oft, mich ganz auf die interessante Physik zu konzentrieren.
- Many thanks to Fabrice Gerbier, Emmanuel Mimoun, Luigi de Sarlo and David Jacob for the very nice time in Paris.
- Vielen Dank gilt der Heidelberger Graduate School for Fundamental Physics, die es mir erlaubte, eine sehr schöne und lehrreiche Zeit in Paris verbringen zu können ohne großen bürokratischen Aufwand.
- Vielen Dank auch an die über die Jahre wechselnden Teams von NaLi, Atta und AEGIS. Ich habe es immer sehr geschätzt mit Euch zusammen zu arbeiten und Euch um so manchen Funktionsgenerator zu erleichtern.
- Viel Dank gilt auch der Landesgraduiertenförderung Baden-Württemberg, die mich finanziell unterstützt hat. Diese Unterstützung sorgte dafür, dass ich

mich voll auf die Physik konzentrieren konnte und dennoch in den Genuss so mancher polorofer Annehmlichkeit kam.

- Der größte Dank gilt meiner Familie und meiner Freundin, die mich während der nicht immer einfachen Zeit sehr unterstützt haben.